NAVAL POSTGRADUATE SCHOOL
Monterey, California

DISSERTATION

MULTIMODE SIMULATIONS OF
FREE ELECTRON LASERS

by

Joseph Blau

March 2002

Dissertation Supervisor: William B. Colson

Approved for public release; distribution is unlimited

Report Documentation Page

Report Date 29 Mar 2002	**Report Type** N/A	**Dates Covered (from... to)** -

Title and Subtitle Multimode Simulations of Free Electron Lasers	**Contract Number**
	Grant Number
	Program Element Number
Author(s) Blau, Joseph	**Project Number**
	Task Number
	Work Unit Number
Performing Organization Name(s) and Address(es) Naval Postgraduate School Monterey, California	**Performing Organization Report Number**
Sponsoring/Monitoring Agency Name(s) and Address(es)	**Sponsor/Monitor's Acronym(s)**
	Sponsor/Monitor's Report Number(s)
Distribution/Availability Statement Approved for public release, distribution unlimited	
Supplementary Notes The original document contains color images.	
Abstract	
Subject Terms	
Report Classification unclassified	**Classification of this page** unclassified
Classification of Abstract unclassified	**Limitation of Abstract** UU
Number of Pages 118	

REPORT DOCUMENTATION PAGE			*Form Approved OMB No. 0704-0188*
Public reporting burden for this collection of information is estimated to average 1 hour per response, including the time for reviewing instruction, searching existing data sources, gathering and maintaining the data needed, and completing and reviewing the collection of information. Send comments regarding this burden estimate or any other aspect of this collection of information, including suggestions for reducing this burden, to Washington headquarters Services, Directorate for Information Operations and Reports, 1215 Jefferson Davis Highway, Suite 1204, Arlington, VA 22202-4302, and to the Office of Management and Budget, Paperwork Reduction Project (0704-0188) Washington DC 20503.			
1. AGENCY USE ONLY ***(Leave blank)***	**2. REPORT DATE** March 2002	**3. REPORT TYPE AND DATES COVERED** Dissertation	
4. TITLE AND SUBTITLE: Multimode Simulations of Free Electron Lasers			**5. FUNDING NUMBERS**
6. AUTHOR(S) Blau, Joseph A.			
7. PERFORMING ORGANIZATION NAME(S) AND ADDRESS(ES) Naval Postgraduate School Monterey, CA 93943-5000			**8. PERFORMING ORGANIZATION REPORT NUMBER**
9. SPONSORING / MONITORING AGENCY NAME(S) AND ADDRESS(ES) N/A			**10. SPONSORING / MONITORING AGENCY REPORT NUMBER**
11. SUPPLEMENTARY NOTES The views expressed in this thesis are those of the author and do not reflect the official policy or position of the Department of Defense or the U.S. Government.			
12a. DISTRIBUTION / AVAILABILITY STATEMENT Approved for public release; distribution is unlimited			**12b. DISTRIBUTION CODE**

13. ABSTRACT ***(maximum 200 words)***

The results of theoretical research on Free Electron Lasers (FELs) are presented. Basic FEL physics is reviewed, using a previously developed classical theory. Numerical simulations based on this theory are described, and numerous examples show how they have been used to increase understanding of existing FELs and to help plan new experiments. Single-mode simulations that follow the evolution of a single-frequency plane wave provide insight into important physical effects in FELs. Results show how these simulations are used to evaluate new FEL designs such as inverse-tapered and step-tapered undulators. Longitudinal multimode simulations model plane waves using finite-length electron and optical pulses. These simulations are used to study coherence evolution in various FEL designs, and to explain effects such as limit-cycle behavior. Transverse multimode simulations that allow for the finite transverse dimensions of the optical wavefronts include the effects of optical mode distortion. These simulations are currently being used to design short Rayleigh length optical cavities that are less sensitive to mirror damage. Four-dimensional simulations are also described, which follow the optical wavefront in x, y, z, and t, including the effects of multiple longitudinal and transverse modes. These simulations are computationally intensive, but may play an important role in the design of future high-power FELs.

14. SUBJECT TERMS Free Electron Lasers, Numerical Simulations, Directed Energy			**15. NUMBER OF PAGES** 118
			16. PRICE CODE
17. SECURITY CLASSIFICATION OF REPORT Unclassified	**18. SECURITY CLASSIFICATION OF THIS PAGE** Unclassified	**19. SECURITY CLASSIFICATION OF ABSTRACT** Unclassified	**20. LIMITATION OF ABSTRACT** UL

NSN 7540-01-280-5500

Standard Form 298 (Rev. 2-89)
Prescribed by ANSI Std. 239-18

THIS PAGE INTENTIONALLY LEFT BLANK

MULTIMODE SIMULATIONS OF FREE ELECTRON LASERS

Joseph A. Blau
B.S., U.C. Santa Barbara, 1987
M.S., U.C. San Diego, 1989

Submitted in partial fulfillment of the
requirements for the degree of

DOCTOR OF PHILOSOPHY IN PHYSICS

from the

NAVAL POSTGRADUATE SCHOOL
March 2002

Author: Joseph A. Blau

Approved by:

William B. Colson Professor of Physics Dissertation Supervisor	Robert Armstead Professor of Physics
Andres Larazza Professor of Physics	James Luscombe Professor of Physics
Ron Pieper Professor of Electrical Engineering	

Approved by: William B. Maier, Chair, Department of Physics

Approved by: Carson K. Eoyang, Associate Provost for Academic Affairs

THIS PAGE INTENTIONALLY LEFT BLANK

ABSTRACT

The results of theoretical research on Free Electron Lasers (FELs) are presented. Basic FEL physics is reviewed, using a previously developed classical theory. Numerical simulations based on this theory are described, and numerous examples show how they have been used to increase understanding of existing FELs and to help plan new experiments. Single-mode simulations that follow the evolution of a single-frequency plane wave provide insight into important physical effects in FELs. Results show how these simulations are used to evaluate new FEL designs such as inverse-tapered and step-tapered undulators. Longitudinal multimode simulations model plane waves using finite-length electron and optical pulses. These simulations are used to study coherence evolution in various FEL designs, and to explain effects such as limit-cycle behavior. Transverse multimode simulations that allow for the finite transverse dimensions of the optical wavefronts include the effects of optical mode distortion. These simulations are currently being used to design short Rayleigh length optical cavities that are less sensitive to mirror damage. Four-dimensional simulations are also described, which follow the optical wavefront in x, y, z, and t, including the effects of multiple longitudinal and transverse modes. These simulations are computationally intensive, but may play an important role in the design of future high-power FELs.

THIS PAGE INTENTIONALLY LEFT BLANK

TABLE OF CONTENTS

LIST OF SYMBOLS

Throughout this dissertation, cgs units are used, except for the dimensionless variables mentioned below, which are defined in the text.

$\vec{A}$	magnetic vector potential
$\vec{a}$	dimensionless optical field
$\vec{B}$	undulator magnetic field
$\overrightarrow{B_s}$	optical magnetic field
$\vec{\beta}$	dimensionless relativistic electron velocity
c	speed of light in vacuum
d	dimensionless value of desynchronism
D	dimensionless optical klystron dispersive strength
δ	dimensionless phase acceleration due to linear undulator taper
Δ	dimensionless phase acceleration due to undulator step-taper
e	electron charge
E	optical field amplitude
$\overrightarrow{E_s}$	electric field of optical wave
ε	electron beam emittance
F	dimensionless filling factor
$F(\tau)$	characteristic function of electron distribution
$f(\nu)$	electron phase velocity distribution
ϕ	phase of optical wave

G	optical field single-pass gain
γ	Lorentz factor
η	single-pass extraction efficiency
J	current density
j	dimensionless current density
k	optical wavenumber
k_0	undulator wavenumber
L	undulator length
l_e	optical pulse length
λ	optical wavelength
λ_0	undulator wavelength
m	electron mass
N	number of undulator periods
n	number of passes through the undulator
ν	dimensionless electron phase velocity
ν_s	dimensionless synchrotron frequency
P	dimensionless optical power
Q	resonator quality factor
q	electron phase velocity shift from resonance
r_e	electron beam radius
r_m	dimensionless mirror radius
r_c	dimensionless radius of curvature
ρ	electron density

S	resonator cavity length
σ_G	electron phase velocity spread due to Gaussian energy spread
σ_θ	electron phase velocity spread due to angular spread
σ_z	dimensionless electron pulse length
t	time
τ	dimensionless time
τ_w	dimensionless position of optical waist
W_0	characteristic optical mode radius
w_0	dimensionless optical waist radius
ω	optical angular frequency
ω_0	undulator angular frequency
ω_β	dimensionless betatron frequency
Z_0	Rayleigh length
z_0	dimensionless Rayleigh length
ζ	dimensionless electron phase

THIS PAGE INTENTIONALLY LEFT BLANK

EXECUTIVE SUMMARY

The free electron laser (FEL) is of interest to the Navy as a scientific tool and a shipboard weapon system to destroy sea-skimming missiles. The FEL uses a relativistic electron beam, which passes through a magnetic undulator inside an optical cavity. The electron beam must be high-energy to produce short optical wavelengths. The magnetic undulator, which consists of spatially alternating magnetic fields, causes the relativistic electrons to "wiggle" and thus radiate and amplify co-propagating light. The optical cavity stores some of the light, allowing it to develop a narrow spectrum through mode competition over many passes.

The key advantages of FELs over existing light sources are tunability, high power, and high efficiency. While the wavelengths of conventional lasers are constrained by the allowed energy transitions of electrons bound in atoms, the wavelength of an FEL can be tuned over a broad range, from microwaves to X-rays, since the electrons are "free" to make energy transitions over a continuum of states. An FEL can amplify large optical power without damage, since there is no heat-absorbing medium within the optical cavity. FELs can be highly efficient: up to 40% extraction efficiency from the electron beam has been demonstrated, and up to 10% wall-plug efficiency may be possible.

The first part of the dissertation explains the classical theory of FELs. The resonance condition relates the optical wavelength to the electron beam energy and properties of the magnetic undulator. The FEL pendulum equation describes the evolution of the electrons with respect to the optical and undulator fields. Phase-space plots are used to show how electrons bunch on the scale of an optical wavelength, enabling power exchange between the electrons and the optical field. The FEL wave equation describes the evolution of the optical field due to electron bunching. Examples show how the electron beam quality (energy spread and emittance) affect bunching and FEL gain. As strong optical fields develop, the electrons begin to undergo synchrotron oscillations in phase space, leading to saturation of the optical power. Tapering the magnetic field along the undulator length can extend the saturation limit.

The following chapters describe the results from a set of numerical FEL simulations based on this classical theory. All of the simulations use the pendulum equation to follow the electron evolution, and the wave equation to follow the optical field evolution. These simulations are described in order of increasing complexity. The simplest ones, single-mode simulations, model the interaction of a single-frequency plane wave with the relativistic electron beam as it travels through the undulator. These simulations provide insight into important physical effects in FELs, and are used to evaluate new FEL designs such as inverse-tapered and step-tapered undulators.

Longitudinal multimode simulations use finite-length electron and optical pulses to model plane waves of multiple frequencies inside the resonator. The slightly slower-moving electron pulse slips back relative to the optical pulse, reducing the overlap and the optical power gain. These simulations are used to study coherence evolution in various FEL designs, and to explain effects such as limit-cycle behavior.

Transverse multimode simulations allow for the finite transverse dimensions of the optical wavefronts. The parabolic wave equation is used to include the effects of optical diffraction. Diffraction generally reduces the overlap between the optical wavefront and the electron beam, but under special conditions the FEL mechanism can continuously distort the optical wave, improving the overlap and enhancing the gain. These simulations are useful in studying new optical cavity designs.

Four-dimensional simulations follow the evolution of the electrons and the optical wavefront in x, y, z, and t, modeling multiple longitudinal and transverse modes. In general, both longitudinal and transverse modes are present and interact with each other. These simulations include the effects of longitudinal pulse slippage and transverse mode distortion. However, they are computationally intensive, requiring large amounts of memory and computer time. Four-dimensional simulations may play an important role in the design of future high-power FELs, which require short Rayleigh-length optical cavities that are less sensitive to mirror damage.

ACKNOWLEDGMENTS

I thank my parents for instilling in me a love of learning and the confidence to pursue my dreams. I thank Prof. Bill Colson for sparking my interest in physics and mentoring me for so many years. I thank Prof. Peter Crooker for interesting discussions and useful suggestions. I thank my wife Kathie for her patience and support as I studied and worked long hours to complete this dissertation. I thank God for bringing people and circumstances into my life to enable me to achieve this goal. And I thank my friends at Mayflower Church for all their prayers and encouragement.

THIS PAGE INTENTIONALLY LEFT BLANK

I. INTRODUCTION

This dissertation presents the results of Free Electron Laser (FEL) research over the past 10 years at the Naval Postgraduate School (NPS). The author has been deeply involved in all of this work, making significant contributions as the co-author of 10 articles published in refereed journals, and as the lead author of 7 of those articles.

An FEL is a new type of laser, which uses a relativistic electron beam to create and amplify coherent radiation. In a conventional laser, the electrons in the lasing medium are bound in atoms, and a particular transition between fixed atomic energy levels determines the radiation wavelength. In an FEL, the electrons are "free" to make an energy transition over a continuum of states, producing radiation over a broad range of wavelengths from microwaves to X-rays, depending on the design parameters. Since there is no heat-absorbing medium inside the optical cavity, an FEL can process large amounts of optical power without damage. At NPS, we do theoretical research and numerical modeling of FELs, helping to design new FELs at many universities and laboratories around the world, and to improve understanding of existing experiments.

Chapter II of this dissertation reviews the basic physics of FELs using a previously developed theory [1], explaining the FEL interaction in terms of the classical pendulum equation and Maxwell's wave equation. The equations are expressed using dimensionless parameters, which give insight into the FEL mechanism, and facilitate numerical modeling. We have used this theory to develop simulations of FELs on desktop computers. These simulations have been benchmarked against theoretical formulas and by comparison to numerous experiments. They have also provided the basis for FEL simulations used by other researchers.

The chapters that follow present the various types of simulations we have developed: single-mode, longitudinal multimode, transverse multimode, and four-dimensional simulations. The basic structure of the simulations is described, including their assumptions and limitations, the input parameters, and the output they produce. Examples are shown of how we have used these simulations at NPS to model FEL experiments, to study important physical effects, and to extend the basic theory to new

FEL concepts. Current NPS research is highlighted, including our ongoing collaboration with the Thomas Jefferson National Accelerator Facility (TJNAF) to develop a high-power FEL for naval applications.

Chapter III describes our single-mode simulations, which model a single-frequency plane wave interacting with many electrons in the relativistic electron beam. We have used these simulations to study the effects of electron beam quality on FEL gain, and to understand basic physical effects in new FEL designs. This research helped to design the SELENE FEL, a ground-based laser proposed in the early 1990's for beaming power to satellites. In recent years we have used single-mode simulations to study new designs for the current and proposed FELs at TJNAF, resulting in several conference presentations and a published article.

Chapter IV describes our longitudinal multimode simulations, which model plane waves using finite-length electron and optical pulses. These simulations have helped to understand new effects such as limit-cycle behavior in short pulse FELs. We used these simulations in the early 1990's to model electron beam energy modulation in the SCA FEL at Stanford. Our longitudinal multimode simulations contributed to the design of a high-power FEL proposed at Boeing in the mid-1990's, predicting the development of a chaotic optical spectrum. More recently we have used these simulations to study mode competition and coherence evolution in the proposed X-ray FEL at SLAC. They continue to play an important role in our FEL design studies for TJNAF. The results of this work have been presented at several conferences and in three published articles.

Chapter V describes our transverse multimode simulations, which allow for optical wavefronts of finite transverse dimensions. We have used these simulations to study optical mode distortion in the SELENE and Boeing FELs, and they have contributed to the design of new optical cavities for the TJNAF FEL. These research results have been presented at several conferences and in two published articles.

Chapter VI describes our four-dimensional simulations, which model the electron beam and the optical wavefront in x, y, z, and t, including the effects of multiple longitudinal and transverse modes. These simulations are computationally intensive, requiring large amounts of memory and computer time. In the early and mid-1990's we developed versions of these simulations that could run on desktop workstations, but applied only to FELs with narrow electron beams. We used these simulations to study coherence evolution and optical mode distortion effects in the Boeing FEL, and to help design an infrared FEL at TJNAF. We presented results of this research at several conferences, and in three published articles. We are currently studying new numerical techniques to reduce the computational requirements for our four-dimensional simulations, which may be useful in the design of high-power FELs for ship defense.

AUTHOR CONTRIBUTIONS

The author has made significant contributions to all of the work described here:

- Planned and participated in FEL research projects;
- Developed numerical simulations of FELs, and interpreted their results;
- Used the simulations to help design new FELs, and to understand important physical effects in existing experiments;
- Extended the basic FEL theory and modified simulations to include new FEL concepts and designs;
- Lead author for 7 articles published in refereed journals;
- Co-author for 3 additional articles published in refereed journals;
- Co-author for 7 published conference contributions;
- Gave more than a dozen oral and poster presentations at FEL conferences;
- Taught classes on FEL theory and simulation techniques;
- Assisted with more that two dozen NPS student theses;
- Represented the NPS FEL group at two TJNAF FEL Upgrade Reviews, and presented the results of our research at those meetings;
- Helped to write an FEL research proposal for JTO, which was recently funded at NPS for $750,000 over the next 3 years.

THIS PAGE INTENTIONALLY LEFT BLANK

II. BASIC FEL THEORY

A Free Electron Laser (FEL) is a device used to create powerful, tunable, coherent radiation for scientific, medical, industrial and military applications. Figure 1 shows a schematic of an FEL oscillator, which was first described by John Madey in the early 1970's [2].

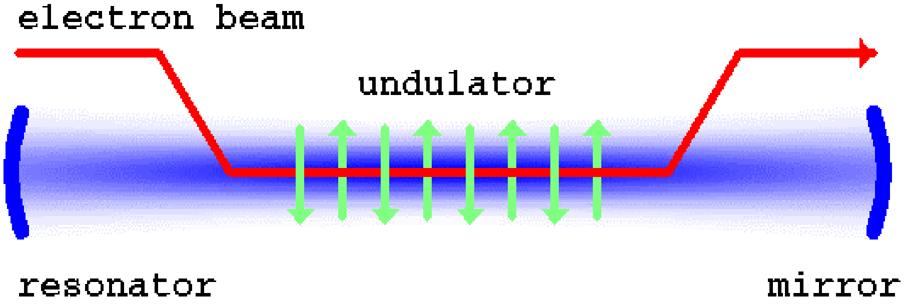

Figure 1. FEL Oscillator

The major components are a relativistic electron beam, a magnetic undulator, and a resonator cavity. A linear accelerator or a storage ring provides the relativistic electron beam, with typical energy of 100 MeV and peak current of 100 A. The undulator is either a series of alternating permanent magnets or a helically wound electromagnet, with typically 50 periods, each a few centimeters long. The undulator field strength is on the order of a few kilogauss. The resonator consists of an evacuated optical cavity typically about 10 meters long, terminated by mirrors on each end. One of the mirrors is partially transmitting to outcouple the light for applications. The electron beam, after passing once through the undulator, can either be directed to a beam dump, or recirculated back to the accelerator to enhance overall efficiency and reduce the energy of the dumped beam.

In an FEL amplifier, there are no mirrors. Radiation from an external source is amplified over a single pass. It is also possible to create and amplify light over a single pass, with no external source, in a process known as self-amplification of spontaneous emission (SASE).

The magnetic undulator gives the relativistic electrons a slight "wiggling" motion from side to side, yielding spontaneous radiation in a narrow cone in the forward direction. The radiation wavelength is determined by the electron beam energy, the undulator wavelength, and the magnetic field strength. The transverse motion of the electrons, when properly coupled to the transverse electric field of the radiation, produces stimulated emission, amplifying the light as it passes through the undulator.

FELs offer significant advantages over existing radiation sources. Unlike a conventional laser, the available wavelengths are not restricted by allowed transitions between energy levels of bound electrons. An FEL can be designed to operate at any wavelength from microwaves to X-rays, and a particular FEL can also be tunable over a broad band. A wavelength range of x10 for a single FEL has been demonstrated [3], and a range of x100 may be possible. Unlike a synchrotron light source, FEL radiation is highly coherent. Since there are no atoms or molecules inside the optical cavity, only relativistic free electrons, exhaust "heat" is removed at the speed of light, so it is possible to process megawatts of optical power inside the cavity. An FEL can be highly efficient; up to 40% energy extraction from the electron beam has been demonstrated [4]. FELs can also produce very short (picosecond) optical pulses, which are useful for many applications.

The first FEL was built at Stanford in the mid 1970's [5]. Since then, hundreds have been constructed around the world, with wavelengths ranging from 0.1 μm to several hundred μm [6]. The most powerful FEL is at Jefferson Labs in Virginia [7]; it has produced 2 kW of average power at 3 μm, and will soon be upgraded to 10 kW [8]. There are proposals to build X-ray FELs, with wavelengths from 1 to 10 Å, at DESY (Germany) and SLAC (Stanford); these would be the world's first X-ray lasers, with many novel applications [9].

A. RESONANCE CONDITION

The primary factor that determines the operating wavelength of an FEL is the electron beam energy γmc^2, where $\gamma = \left(1-\vec{\beta}^2\right)^{-1/2}$ is the Lorentz factor, $\vec{v} = \vec{\beta}c$ is the electron velocity, m is the electron rest mass, and c is the speed of light. In the reference frame of the electron, the undulator wavelength λ_0 is Lorentz contracted to $\lambda_0{}' = \lambda_0/\gamma$, and the electron will oscillate and emit light at that same wavelength, $\lambda' = \lambda_0'$. In the laboratory frame, the light is Doppler shifted to the wavelength $\lambda = \lambda'/2\gamma$, which gives

$$\lambda \approx \frac{\lambda_0}{2\gamma^2}. \tag{1}$$

This equation is approximate because it neglects the transverse motion of the electron (it assumes the undulator field is very small), but it shows the relationship between electron energy and optical wavelength. Thus, to achieve very short wavelengths, such as the proposed X-ray FEL at SLAC, requires a high-energy electron beam (>10 GeV, so that $\gamma > 20000$), whereas infrared radiation can be produced with a more modest accelerator ($\sim 50\,\mathrm{MeV}$, $\gamma \sim 100$). Visible and ultraviolet FELs require beam energies on the order of 500 MeV ($\gamma \sim 1000$).

A more precise relationship can be derived by considering a single electron traveling at speed $\beta_z c$ along the undulator (z) axis, with $\beta_z \approx 1$, and a co-propagating photon traveling at speed c. The undulator gives transverse motion to the electron, enabling energy exchange through the relativistic Lorentz equation,

$$\frac{d\gamma}{dt} = -\frac{e}{mc}\vec{\beta}\cdot\vec{E} \tag{2}$$

where $e = |e|$ is the electron charge magnitude and $\vec{E}$ is the electric field of the light wave. Since the light wave is transverse, $E_z = 0$ and only the transverse components of the velocity, $\beta_\perp = \beta_{x,y}$, contribute to energy exchange in (2). For optimum energy exchange, these components should oscillate at the same frequency as $\vec{E}$. This leads to the following resonance condition: one wavelength of light passes over an electron as the electron travels through one undulator period. In the corresponding time interval Δt, the electron travels a distance $\lambda_0 = c\beta_z\Delta t$ and the photon travels a distance $\lambda_0 + \lambda = c\Delta t$. Thus,

$$\lambda = \left(\frac{1-\beta_z}{\beta_z}\right)\lambda_0. \tag{3}$$

If we assume a highly relativistic electron beam $(\gamma \gg 1)$ and ignore the transverse motion of the electron $(\beta_\perp \ll 1)$, then $\beta_z \approx 1 - 1/2\gamma^2$, and the resonance condition (3) reduces to the previous result (1).

B. ELECTRON DYNAMICS

1. Betatron Motion

To understand the processes of spontaneous and stimulated emission in an FEL, it is necessary to study the motion of the electrons in the undulator. First, we will derive the electron trajectories in a linearly polarized undulator with no light present. The magnetic field for an ideal linear undulator can be written in rectangular coordinates [10]

$$\overrightarrow{B_L} = B\big(0,\, \sin(k_0 z)\cosh(k_0 y),\, \cos(k_0 z)\sinh(k_0 y)\big) \tag{4}$$

where $k_0 = 2\pi/\lambda_0$ is the undulator wavenumber, and λ_0 is the undulator period. Along the undulator (z) axis, the field is given by $B\sin(k_0 z)\,\hat{y}$ with an rms value $B_{\text{rms}} = B/\sqrt{2}$. Typically $k_0 y \ll 1$, since $\lambda_0 \sim 5$ cm and the beam radius $\overline{y} \sim 1$ mm. Off axis, the average field $\overline{B} = B_{\text{rms}}\left(1 + k_0^{\,2} y^2 + \cdots\right)$ increases with y, focusing the electrons back towards the axis. Since the field (4) is independent of x, there is no natural focusing in the x direction. In practice, the beam may be focused using parabolic pole faces or a quadrupole lens.

The electron motion is determined by the relativistic Lorentz force equations,

$$\frac{d\left(\gamma \vec{\beta}\right)}{dt} = -\frac{e}{mc}\left(\vec{E} + \vec{\beta} \times \vec{B}\right) \tag{5}$$

plus the energy equation (2). Using (4) for the undulator field and assuming no light present $\left(\vec{E} = 0\ , \dot{\gamma} = 0\right)$, we obtain

$$\begin{aligned}
\dot{\beta}_x &= -\frac{eB}{\gamma mc^2}\left[\cos\left(k_0 z\right)\dot{y}\sinh\left(k_0 y\right) - \dot{z}\sin\left(k_0 z\right)\cosh\left(k_0 y\right)\right] \\
\dot{\beta}_y &= +\frac{eB}{\gamma mc^2}\dot{x}\cos\left(k_0 z\right)\sinh\left(k_0 y\right) \\
\dot{\beta}_z &= -\frac{eB}{\gamma mc^2}\dot{x}\sin\left(k_0 z\right)\cosh\left(k_0 y\right)
\end{aligned} \tag{6}$$

The first equation is easily integrated:

$$\beta_x = -\sqrt{2}\,\frac{K}{\gamma}\cos\left(k_0 z\right)\cosh\left(k_0 y\right) \tag{7}$$

where $K = eB_{\mathrm{rms}}\lambda_0 / 2\pi mc^2$ is the "undulator parameter", a dimensionless quantity approximately equal to 1 for most FELs. We have assumed perfect injection in the x direction, so the integration constant in (7) is zero. Now substitute (7) into the last two equations in (6) to get

$$\begin{aligned}
\dot{\beta}_y &= -\frac{cK^2 k_0}{\gamma^2}\cos^2\left(k_0 z\right)\sinh\left(2k_0 y\right) \\
\dot{\beta}_z &= \frac{cK^2 k_0}{\gamma^2}\sin\left(2k_0 z\right)\cosh^2\left(k_0 y\right) .
\end{aligned} \tag{8}$$

Averaging over many undulator periods and assuming the electron is near the undulator axis $\left(k_0 y \ll 1\right)$ gives $\overline{\dot{\beta}_y} \approx -\left(cK^2 k_0^2 / \gamma^2\right) y$ and $\overline{\dot{\beta}_z} \approx 0$. Thus the averaged equation of motion for y is

$$\frac{d^2 y}{d\tau^2} = -\left(\frac{Kk_0 L}{\gamma}\right)^2 y \tag{9}$$

where we have used the dimensionless time $\tau = ct/L$. This corresponds to simple harmonic motion at the dimensionless betatron frequency, $\omega_\beta \equiv Kk_0 L/\gamma = 2\pi NK/\gamma$. For typical FEL parameters, $\omega_\beta \approx 2\pi$, so there is one betatron oscillation along the undulator.

The general solution to the harmonic oscillator equation (9) can be written

$$y(\tau) = y_0\cos\left(\omega_\beta \tau\right) + \frac{L\theta_y}{\omega_\beta}\sin\left(\omega_\beta \tau\right) \tag{10}$$

where y_0 and θ_y are the initial position and angle of an electron at the undulator entrance $(\tau = 0)$, with respect to the undulator axis. The initial angle is related to the initial *y*-velocity by $\theta_y = \overset{\circ}{y}(0)\big/L$ where $\overset{\circ}{(\ )}$ indicates a derivative with respect to dimensionless time τ. Equation (10) describes the electron betatron motion in a linearly polarized undulator with no light present.

For a helical undulator, the magnetic field can be written in cylindrical coordinates using Bessel functions [1]. Near the undulator axis, the average transverse field can be expanded for $k_0 r \ll 1$ to get $\overline{B}_\perp = B\left(1 + k_0^2 r^2/4 + \cdots\right)$, which increases off axis at half the rate of the linear field, so the betatron frequency is reduced by a factor of $\sqrt{2}$. Since the field is axially symmetric, there is equal betatron focusing in both the *x* and *y* directions.

2. FEL Pendulum Equation

Now we consider how a co-propagating optical wave affects the electron dynamics. For a helical undulator, assuming that betatron focusing keeps the electrons near the undulator axis, the field can be simplified in rectangular coordinates to

$$\overrightarrow{B_H} = B\left(\cos k_0 z, \sin k_0 z, 0\right). \tag{11}$$

Note that unlike the linear case, the field amplitude is constant along the *z*-axis, so $B_{\mathrm{rms}} = B$ in the definition of the undulator parameter *K*.

Now introduce a helically polarized, monochromatic plane wave with wavenumber *k* and frequency ω, traveling in the +*z* direction, with optical fields given by

$$\overrightarrow{E_s} = E\left(\cos\psi,\, -\sin\psi,\, 0\right) \;\;,\;\; \overrightarrow{B_s} = E\left(\sin\psi,\, \cos\psi,\, 0\right) \tag{12}$$

where $\psi = kz - \omega t + \phi$, *E* is the optical field amplitude in cgs unit, and ϕ is the optical phase. Integrating (5) using the undulator field (11) and the optical field (12), with the assumption $\gamma \gg 1$, gives the electron trajectories,

$$\overrightarrow{\beta_\perp} = -\frac{K}{\gamma}\left(\cos k_0 z,\, \sin k_0 z,\, 0\right) \;\;,\;\; \beta_z = 1 - \frac{1+K^2}{2\gamma^2}. \tag{13}$$

We again assume perfect injection of the electrons into the undulator, so the constants of integration are zero. Imperfections in the electron beam will be discussed later. Note that the amplitude of the transverse oscillations is small since $K/\gamma \ll 1$, but as we will see in the next section, it is these oscillations that cause spontaneous emission, and couple the electron motion to the optical wave to enable stimulated emission.

Using the expression (13) for β_z, the resonance condition (3) can now be written

$$\lambda = \frac{\lambda_0}{2\gamma^2}\left(1+K^2\right). \tag{14}$$

Substituting $\vec{\beta}_\perp$ from (13) into the energy equation (2) gives

$$\dot{\gamma} = \frac{d\gamma}{dt} = \frac{eKE}{\gamma mc}\cos\left(\zeta + \phi\right) \tag{15}$$

where $\zeta = (k+k_0)z - \omega t$ is the electron phase with respect to the combined optical and undulator fields. Equation (15) contains the physics of energy exchange: if the electron phases ζ are uniformly distributed, then half the electrons will gain energy $(\dot{\gamma} > 0)$ and half the electrons will lose energy $(\dot{\gamma} < 0)$. In order to have a net energy transfer, the electrons must be bunched on the scale of the optical wavelength.

The electron phase velocity is given by $d\zeta/dt = \left(k+k_0\right)\beta_z c - \omega$. Taking another time derivative, assuming $\gamma \gg 1$ and using (13) for β_z gives

$$\frac{d^2\zeta}{dt^2} = kc\left(\frac{1+K^2}{\gamma^2}\right)\left(\frac{\dot{\gamma}}{\gamma}\right). \tag{16}$$

Substituting $\dot{\gamma}$ from (15) and using the resonance condition (14),

$$\frac{d^2\zeta}{dt^2} = \frac{2eKEk_o}{\gamma^2 m}\cos\left(\zeta + \phi\right). \tag{17}$$

Assuming the electron energy γmc^2 doesn't change much over an undulator period, we can simplify this equation to obtain

$$\overset{\circ}{\nu} = \frac{d^2\zeta}{d\tau^2} = |a|\cos\left(\zeta + \phi\right) \tag{18}$$

where $\nu = \overset{\circ}{\zeta} = L\left[\left(k+k_0\right)\beta_z - k\right]$ is the dimensionless electron phase velocity, and $|a| = 4\pi NeKLE/\gamma^2 mc^2$ is the dimensionless optical field amplitude. The variable ν is also known as the "resonance parameter", since $\nu = 0$ for an electron that satisfies the resonance condition.

The result (18) also holds for a linear undulator if we replace *K* in the definition of $|a|$ by $K\left(J_0(\xi) - J_1(\xi)\right)$, where J_0 and J_1 are Bessel functions of the first kind, and $\xi = K^2/2\left(1+K^2\right)$. [1]

Equation (18) is known as the FEL pendulum equation. It describes the microscopic motion of each electron along the *z*-axis in a reference frame one optical wavelength long, traveling at the speed of a resonant electron. In that reference frame, the electron motion is analogous to a classical pendulum. [11]

To visualize this motion, it is useful to look at a phase space plot such as Figure 2 below, which shows the electron evolution in ζ and $\nu = \overset{\circ}{\zeta}$ for a typical low-gain FEL. This figure was produced by numerically solving the pendulum equation (18) in a single-mode simulation, as described in a later chapter. Twenty sample electrons are injected at resonance, each with initial phase velocity $\nu_0 = \nu(0) = 0$, and their initial phases ζ_i evenly distributed. A color scale is used to show their evolution from the beginning of the undulator ($\tau = 0$, yellow), to the end of the undulator ($\tau = 1$, red). The electrons are seen to follow pendulum phase space orbits. The separatrix, drawn in red for reference, is defined by $\nu_s^2 = 2|a|\left[1+\sin\left(\zeta_s + \phi\right)\right]$. The separatrix passes through the unstable fixed points at $(\zeta,\nu) = (-\pi/2, 0)$ and $(3\pi/2, 0)$, with peak-to-peak height $4|a|^{1/2}$. Inside the separatrix, the electrons follow closed paths around the stable fixed point at $(\zeta,\nu) = (\pi/2, 0)$, corresponding to a pendulum swinging back and forth; outside the separatrix are open paths, corresponding to a pendulum swinging "over the top". Notice at the end of the undulator the electrons are bunched near $\zeta = \pi/2$.

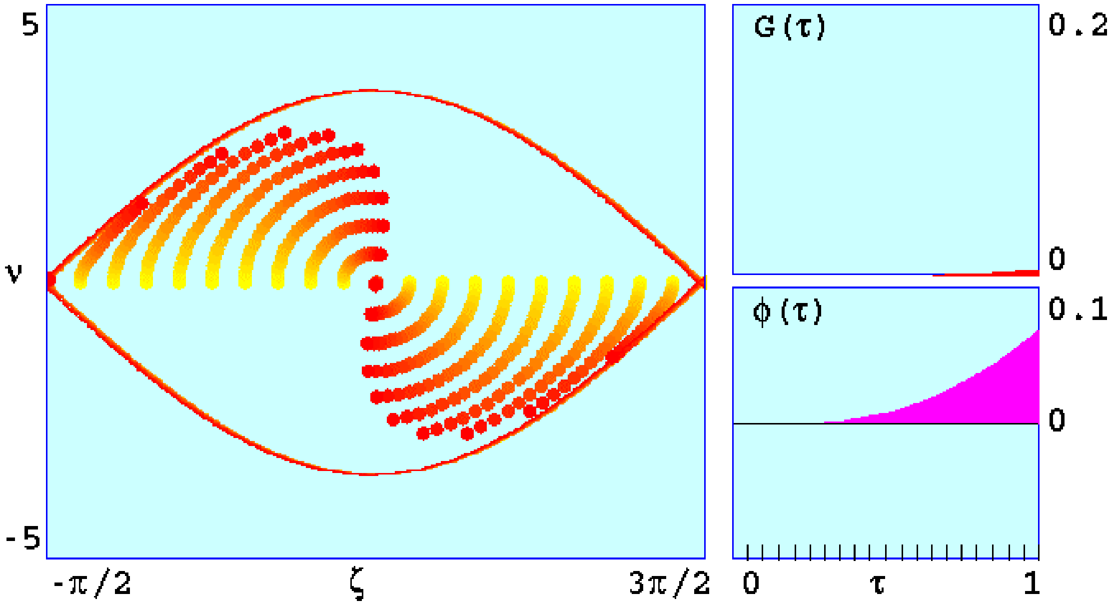

Figure 2. Electron evolution in (ζ, ν) phase space, optical field gain $G(\tau)$ and phase $\phi(\tau)$ for a single pass through a typical low-gain FEL, with electrons injected at resonance $(\nu_0 = 0)$. The electrons follow pendulum phase space orbits, and there is no net gain $(G \approx 0)$.

A change in phase velocity $\Delta\nu$ can be related to an energy change $\Delta\gamma$ using the definition of ν after (18), the definition of β_z (13), and the resonance condition (14), to obtain $\Delta\nu = 4\pi N \Delta\gamma / \gamma$. Thus the electrons gain energy when they move up on the phase space plot, and lose energy when they move down. In Figure 2, half of the electrons gain energy and half lose energy. The net result is very little energy transfer, as shown by the gain evolution plot $G(\tau)$ in the upper-right. The gain is defined by $G(\tau) = \left[P(\tau) - P_0\right]/P_0$, where $P(\tau)$ is the optical power at time τ, and $P_0 = P(0)$ is the initial optical power. The lower-right plot shows the optical phase evolution $\phi(\tau)$, which causes the separatrix to shift slightly.

Figure 3 shows another simulation with the electrons injected slightly off resonance at $\nu_0 \approx 2.6$. Some electrons now follow open orbits above the separatrix; those on the left side of the plot move ahead faster, while those on the right move slower.

The net effect is bunching near $\zeta = \pi$, where the electrons "fall" towards smaller values of ν, losing energy to the optical wave. Thus the final gain increases to about 13%, whereas in the previous case it was only about 0.5%. Also note that the optical phase shift has decreased.

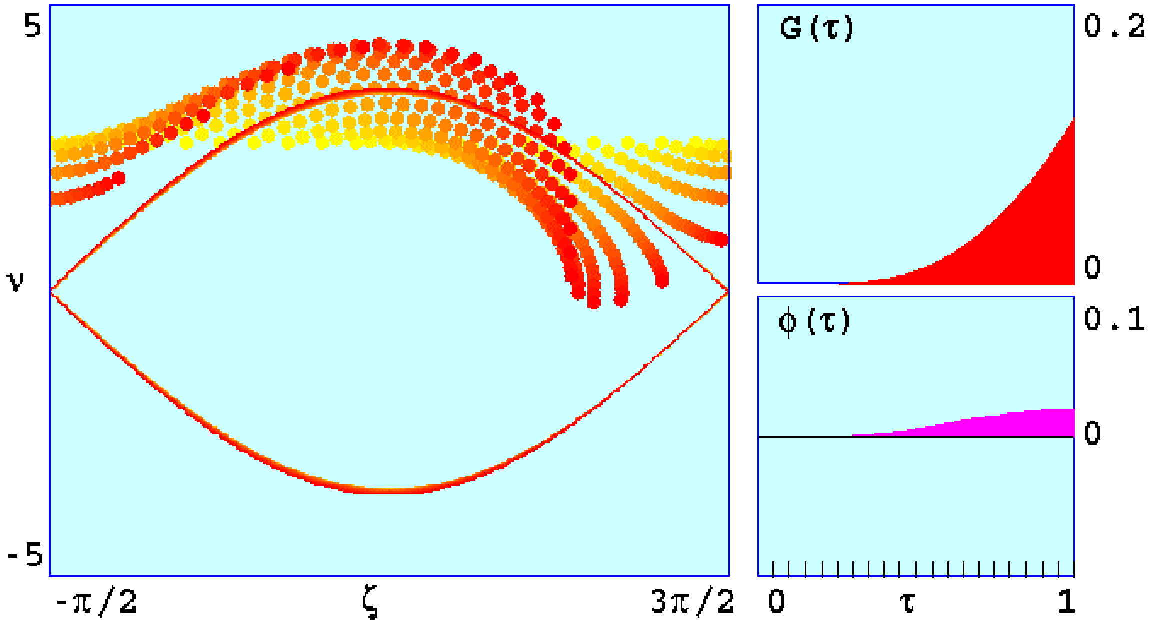

Figure 3. Electron evolution in (ζ,ν) phase space, optical field gain $G(\tau)$ and phase $\phi(\tau)$ for a single pass through a typical low-gain FEL, with electrons injected slightly off resonance $(\nu_0 = 2.6)$. The electrons still follow pendulum phase space paths, but now there is significant energy extraction and gain of about 13%.

If the electrons are started farther off resonance (larger ν_0), the phase space orbits flatten out and there is less gain. If the electrons start with a negative phase velocity $(\nu_0 < 0)$, they bunch near $\zeta = 0$ and absorb energy from the optical field. Figure 4 shows the gain in a single pass through the undulator, plotted versus initial electron phase velocity ν_0, generated by repeating a single-mode simulation while varying ν_0. The gain curve in Figure 4 is antisymmetric, and the peak gain is about 13% at $\nu_0 \approx 2.6$. The gain bandwidth is $\Delta\nu \approx 2\pi$. Extracting energy in excess of the gain bandwidth,

$\Delta\nu = 4\pi N \Delta\gamma/\gamma \approx 2\pi$, reduces the gain, so the maximum theoretical efficiency of an FEL (single pass energy extraction) is $\Delta\gamma/\gamma \approx 1/2N$.

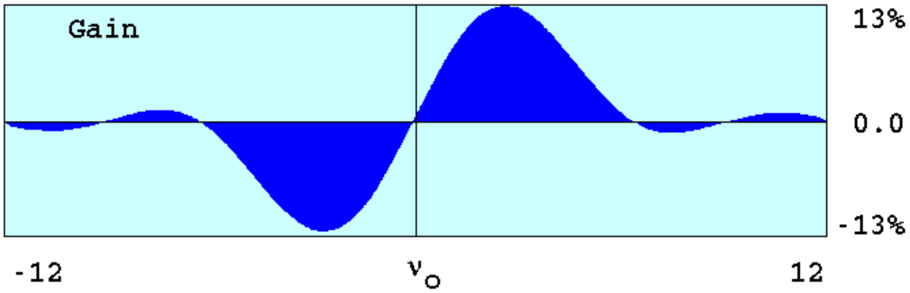

Figure 4. Single-pass gain versus initial electron phase velocity for a low-gain FEL with weak optical fields. The gain curve is anti-symmetric, with peak gain of about 13% at $\nu_0 \approx 2.6$.

Our derivation of the pendulum equation (18) assumed perfect injection of the electron beam into the undulator. If an electron is injected off-axis, at a displacement y_0 or an angle θ_y, it will undergo betatron motion described in (10). With the assumptions $\theta_y \ll \pi$ and $k_0 y_0 \ll 1$, it can be shown [12] that the corresponding phase velocity is reduced by

$$\Delta\nu_\beta = -\frac{2\pi N}{1+K^2}\left(K^2 k_0^2 y_0^2 + \gamma^2\theta_y^2\right). \tag{19}$$

Note that this shift is constant in time, so with an adjustment to the initial phase velocity, we can still use the pendulum equation to determine the electron's phase space evolution.

In a realistic beam, the electrons enter the undulator with a random distribution of positions and angles characterized by rms spreads $\overline{y_0}$ and $\overline{\theta_y}$. Each of those can be changed using focusing fields, but their product, known as the emittance $\varepsilon_y = \overline{y_0}\,\overline{\theta_y}$, is fixed [1]. Experimentalists try to "match" these quantities so that the beam is not too large and does not expand too much along the undulator. When the matching condition $K k_0 \overline{y_0} \approx \gamma\overline{\theta_y}$ is satisfied, the phase velocity spread $\overline{\Delta\nu_\beta} \approx 2\pi N K k \varepsilon_y/\gamma$ is minimized. Figure 4 shows that the natural gain bandwidth of an FEL is $\Delta\nu \approx 2\pi$, so for optimum gain the emittance should be limited to $\varepsilon_y^{\max} \approx \gamma\lambda/2\pi NK$, which corresponds to about 1 mm-mrad for typical FEL parameters. For a short wavelength FEL, or one with many undulator periods *N*, the required emittance can be significantly less.

C. OPTICAL FIELD EVOLUTION

1. Spontaneous Emission

The small transverse oscillations (13) of the relativistic electrons cause them to radiate light into a forward cone of angular width on the order of γ^{-1} [13]. If $K \lesssim 1$, the radiation cone stays in a detector on axis at infinity, but if $K \gtrsim 1$ the cone periodically deflects out of the detector, producing higher frequency harmonics [14]. This spontaneous emission is required for start-up of an FEL oscillator or SASE FEL. According to the FEL resonance condition (14), the fundamental frequency is $\omega = 2\gamma^2 k_0 c \big/ \left(1+K^2\right)$. The total radiated power at each frequency can be found from the relativistic Larmor formula, which reduces to a simple result that for each pass through a typical undulator $\left(K \approx 1\right)$, only a small fraction of the electrons in the beam, $\alpha K^2 \approx 10^{-2}$, contributes a photon to the fundamental mode, where α is the fine structure constant [1].

2. Stimulated Emission

Now we consider how the optical wave and electrons evolve as they interact in the undulator. First, we derive a simple formula for the gain in weak optical fields, $|a| \ll \pi$. We assume a perfect electron beam, with all the electrons at the same initial phase velocity ν_0 and their initial phases ζ_0 evenly distributed. If we assume low gain, $a \approx a_0$, then we can expand ζ and ν in powers of the initial field amplitude a_0:

$$\begin{aligned} \zeta &= \zeta^{(0)} + \zeta^{(1)} + \zeta^{(2)} + \cdots \\ \nu &= \nu^{(0)} + \nu^{(1)} + \nu^{(2)} + \cdots. \end{aligned} \tag{20}$$

To zeroth order in a_0 (no optical field), $\zeta^{(0)} = \zeta_0 + \nu_0\tau$ and $\nu^{(0)} = \nu_0$. To first order in a_0,

$$\zeta^{(1)} = -\frac{a_0}{\nu_0^2}\left[\cos(\zeta_0 + \nu_0\tau) - \cos\zeta_0 + \nu_0\tau\sin\zeta_0\right]$$
$$\nu^{(1)} = \frac{a_0}{\nu_0}\left[\sin(\zeta_0 + \nu_0\tau) - \sin\zeta_0\right]. \tag{21}$$

Since an electron's energy is proportional to its phase velocity ν, we must have $\langle v\rangle - \nu_0 \neq 0$ in order to have a net energy transfer, where $\langle\cdots\rangle$ indicates an average over all the electrons. But the electrons are evenly distributed in ζ_0, so (21) implies $\langle\nu^{(1)}\rangle = 0$, and thus to determine the gain the second-order term is required [1]

$$\nu^{(2)} = \frac{a_0^2}{\nu_0^3}\left[-\tfrac{1}{4}\left(\cos(2\zeta_0 + 2\nu_0\tau) - \cos 2\zeta_0\right) + \cos(\nu_0\tau) - 1 - \nu_0\tau\sin\zeta_0\cos(\zeta_0 + \nu_0\tau)\right]. \tag{22}$$

The first term inside the braces averages to zero over all the electrons, so we are left with

$$\langle\nu^{(2)}\rangle = \frac{a_0^2}{\nu_0^3}\left[\cos(\nu_0\tau) - 1 + \tfrac{1}{2}\nu_0\tau\sin(\nu_0\tau)\right]. \tag{23}$$

Recalling $\Delta\nu = 4\pi N\,\Delta\gamma/\gamma$, we can write the average energy change of an electron as

$$\overline{\Delta\gamma}\,mc^2 = \frac{\gamma mc^2\left(\langle\Delta\nu\rangle - \nu_0\right)}{4\pi N} = \frac{\gamma mc^2}{4\pi N}\langle\nu^{(2)}\rangle. \tag{24}$$

To obtain the total energy change of all the electrons in a volume element dV inside the laser beam, multiply (24) by the number of electrons in that volume, $\rho F dV$, where ρ is the electron beam density and F is the "filling factor", defined as the cross-section area of the electron beam divided by the cross-section area of the optical mode. From energy conservation, all of the energy lost by the electrons goes into the optical field. The radiation energy in dV is $2E^2\,dV/8\pi$. We define the gain of the optical field as the fractional increase in the optical field power or energy, giving

$$G = -\frac{(\rho F dV)\left(\gamma mc^2/4\pi N\right)\langle\nu^{(2)}\rangle}{2E^2\,dV/8\pi}. \tag{25}$$

Simplifying and using (23), we obtain

$$G = \frac{j}{\nu_0^3}\left[2 - 2\cos(\nu_0\tau) - \nu_0\tau\sin(\nu_0\tau)\right] \tag{26}$$

where $j = 8N\left(e\pi KL\right)^2 \rho F / \gamma^3 mc^2$ is the dimensionless current density. This result is valid for weak fields $\left(a_0 \ll \pi\right)$ and low gain $\left(j \lesssim \pi\right)$. Equation (26) describes the gain curve shown in Figure 4, which was obtained by numerical simulation.

3. Coherence Development

The electron phase velocity ν is a function of the optical wavenumber *k*, so that a change in ν implies a change in the frequency of the optical mode inside the resonator. Thus by varying ν and calculating the FEL response, we can obtain the gain or power spectrum.

The spontaneous emission spectrum $s(\nu)$ is symmetric in shape, centered at $\nu = 0$ with a width $\Delta\nu \approx 2\pi$. [1] In weak fields and low gain, each mode will have gain $G(\nu)$ given by (26), antisymmetric about $\nu = 0$ with a peak at $\nu = 2.6$. Each pass through the undulator, the optical power in each mode $P(\nu)$ will evolve according to

$$\Delta P(\nu) = s(\nu) + P(\nu)\left[G(\nu) - 1/Q\right] \tag{27}$$

where Q is the resonator quality factor; for $Q \gg 1$, the loss on each pass is given by $1/Q$. Over many passes, mode competition will cause the linewidth to narrow, as shown in Figure 5. The bottom graph shows the spontaneous emission spectrum $s\left(\nu\right)$. Above that is the theoretical gain spectrum $G\left(\nu\right)$ for a low-gain FEL (identical to Figure 4). Above that is the optical power spectrum evolution $P\left(\nu, n\right)$ $n = 100$ passes, showing that the initially broad spectrum narrows and shifts over to the peak of the gain curve, due to mode competition. At the top is the final power spectrum $P_f\left(\nu\right)$. Eventually, the optical linewidth is transform limited by the optical pulse length, which is determined by the electron pulse length.

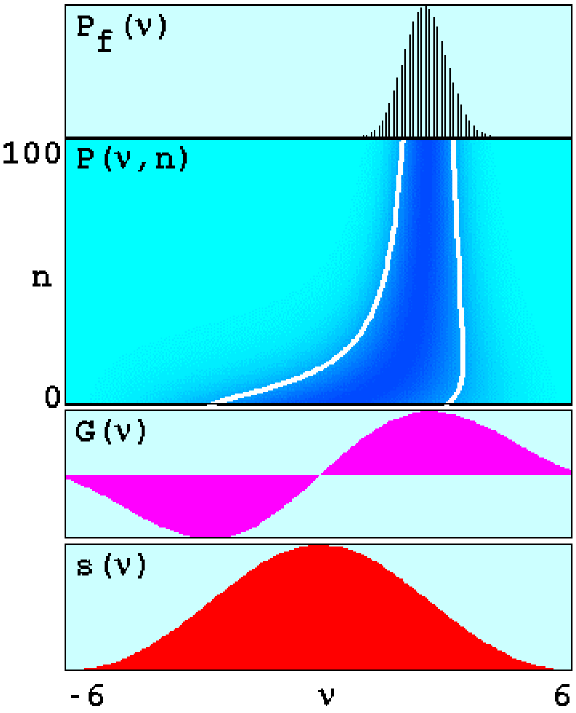

Figure 5. Spontaneous emission spectrum $s(\nu)$, gain spectrum $G(\nu)$, optical power spectrum evolution $P(\nu,n)$, and final power spectrum $P_f(\nu)$ for a typical low-gain FEL, showing coherence evolving through mode competition as the laser line narrows over $n=100$ passes.

4. FEL Wave Equation

A more general formula for the optical wave evolution can be derived by starting with Maxwell's wave equation in the Coulomb gauge,

$$\left(\nabla^2 - \frac{1}{c^2}\frac{\partial^2}{\partial t^2}\right)\vec{A} = -\frac{4\pi}{c}\vec{J_\perp} \tag{28}$$

where $\vec{A}$ is the optical wave vector potential and $\vec{J_\perp}$ is the transverse current density. For a helical undulator, the light emitted will be circularly polarized, and the wave vector corresponding to the field (11) can be written in rectangular coordinates as

$$\vec{A}(z,t) = \frac{E(z,t)}{k}\left(\sin\psi\,,\cos\psi\,,0\right) \tag{29}$$

where $\psi = kz - \omega t + \phi(z,t)$. We assume the field amplitude and phase vary slowly in time over an optical period $\left(dE/dt \ll \omega E,\ d\phi/dt \ll \omega\phi\right)$ and in space over an optical wavelength $\left(dE/dz \ll kE,\ d\phi/dz \ll k\phi\right)$. Then the left-hand side of the wave equation can be written

$$\left(\nabla^2 - \frac{1}{c^2}\frac{\partial^2}{\partial t^2}\right)\vec{A} \approx 2\left(\frac{\partial E}{\partial z} + \frac{1}{c}\frac{\partial E}{\partial t}\right)(\cos\psi, -\sin\psi, 0) \\ - 2E\left(\frac{\partial \phi}{\partial z} + \frac{1}{c}\frac{\partial \phi}{\partial t}\right)(\sin\psi, \cos\psi, 0)\ . \tag{30}$$

Define the unit vectors $\hat{\varepsilon}_1 = (\cos\psi, -\sin\psi, 0)$ and $\hat{\varepsilon}_2 = (\sin\psi, \cos\psi, 0)$, then project the wave equation onto each of these vectors to obtain

$$\frac{\partial E}{\partial z} + \frac{1}{c}\frac{\partial E}{\partial t} = -\frac{2\pi}{c}\left(\overrightarrow{J_\perp}\cdot\hat{\varepsilon}_1\right) \\ E\left(\frac{\partial \phi}{\partial z} + \frac{1}{c}\frac{\partial \phi}{\partial t}\right) = \frac{2\pi}{c}\left(\overrightarrow{J_\perp}\cdot\hat{\varepsilon}_2\right)\ . \tag{31}$$

Now write the total beam current as a sum of single-particle currents:

$$\overrightarrow{J_\perp}\left(\vec{x}\right) = -ec\sum_i \overrightarrow{\beta_\perp}\delta^3\left(\vec{x} - \vec{r_i}\right) \tag{32}$$

where $\vec{r_i}$ is the position of an electron with transverse velocity $\overrightarrow{\beta_\perp}$ given by (13). The projection of $\overrightarrow{J_\perp}$ onto $\hat{\varepsilon}_1$ and $\hat{\varepsilon}_2$ is

$$\overrightarrow{J_\perp}\cdot\hat{\varepsilon}_1 = \frac{ecK\rho}{\gamma}\left\langle\cos(\psi + k_0 z)\right\rangle \\ \overrightarrow{J_\perp}\cdot\hat{\varepsilon}_2 = \frac{ecK\rho}{\gamma}\left\langle\sin(\psi + k_0 z)\right\rangle \tag{33}$$

where we have assumed $N \gg 1$, and replaced the sum over all the electrons by an average $\left\langle\cdots\right\rangle$ over sample electrons, weighted by the current density ρ. Substituting (33) into (31) and using $\zeta + \phi = \psi + k_0 z$, the wave equation can be written in complex form as

$$\left(\frac{\partial}{\partial z} + \frac{1}{c}\frac{\partial}{\partial t}\right)Ee^{i\phi} = -\frac{2\pi eK\rho}{\gamma}\left\langle e^{-i\zeta}\right\rangle\ . \tag{34}$$

If we assume a long electron pulse, we can remove the *z*-dependence from this equation, and it simplifies to

$$\overset{\circ}{a} = \frac{da}{d\tau} = -j\left\langle e^{-i\zeta} \right\rangle \tag{35}$$

where $a = |a|e^{i\phi}$ is the dimensionless optical field and *j* is the dimensionless current density. This is known as the FEL wave equation. It has the same form for a linear undulator, if we replace *K* in the definitions of *a* and *j* by $K\left(J_0(\xi) - J_1(\xi)\right)$, as before.

The FEL wave equation (35) clearly demonstrates that the electron beam needs to be bunched so that $\left\langle e^{-i\zeta} \right\rangle \neq 0$ in order to achieve gain. If the electrons are bunched near $\zeta \approx \pi$, the field amplitude $|a|$ will increase; if the electrons are bunched near $\zeta \approx 0$, the amplitude will decrease. Bunching near $\zeta \approx \pm\pi/2$ will drive the optical phase ϕ, with little change in the amplitude. The wave equation also shows that the gain depends on the dimensionless current density *j*; for $j \lesssim \pi$ there is low gain, and for $j \gg \pi$ there is high gain.

5. Diffraction

For a low gain FEL, the fundamental optical mode inside the laser cavity is mainly determined by the cavity mirrors, and is typically Gaussian in shape. The beam waist radius is on the order of a few mm, and is usually located in the middle of the undulator. From there, the beam will spread out by diffraction, doubling in area over a distance Z_0 known as the Raleigh length, which is determined by the curvature of the mirrors. If Z_0 is too large, the mode waist becomes large, so there is reduced overlap with the narrow electron beam (radius ~ 1 mm), and less gain. If Z_0 is too small, the mode waist is small, but the beam rapidly expands near the ends of the undulator, again reducing overlap and gain. The value of Rayleigh length that theoretically optimizes overlap and gain is $Z_0 = L/\sqrt{12} \approx 0.3L$, where *L* is the undulator length [15].

To study the evolution of transverse optical modes, we use the parabolic wave equation [16]:

$$\left[-\frac{i}{4}\nabla_{\perp}^{2}+\frac{\partial}{\partial\tau}\right]a\left(x,y,z,\tau\right)=-\left\langle je^{-i\zeta}\right\rangle_{(x,y,z-\tau,\tau)} \tag{36}$$

where $\nabla_{\perp}^{2}=\partial_{x}^{2}+\partial_{y}^{2}$, and the x and y coordinates are normalized to the characteristic mode radius, $\sqrt{L\lambda/\pi}$. The operator $-i\nabla_{\perp}^{2}/4$ describes the beam diffraction. The electron evolution is determined by the pendulum equation (18), which still has the same form, but the field amplitude $|a|$ now has x and y dependence.

The current density j on the right-hand side of (36) drives both the real and imaginary parts of the optical field a on the left-hand side. Thus a narrow electron beam can distort the optical mode by changing the amplitude and/or the phase of the central portion of the wavefront. In an FEL oscillator with modest gain, $j\approx 10$, the steady-state resonator mode shape can be altered by the FEL interaction. In an FEL amplifier with very large gain, $j\gg 10^{3}$, a process known as "optical guiding" [17] can effectively contain the light in the vicinity of the electron beam, continuously opposing the natural diffraction.

D. WEAK OPTICAL FIELDS

1. FEL Integral Equation

In weak optical fields, $|a|\ll\pi$, we use the expansion (20) for ζ and ν, and the wave equation (35) becomes

$$\overset{\circ}{a}=ij\left\langle e^{-i(\zeta_{0}+\nu_{0}\tau)}\zeta^{(1)}\right\rangle \tag{37}$$

while the pendulum equation (18) becomes

$$\frac{d^{2}\zeta^{(1)}}{d\tau^{2}}=\frac{1}{2}\left[ae^{i(\zeta_{0}+\nu_{0}\tau)}+a^{*}e^{-i(\zeta_{0}+\nu_{0}\tau)}\right]. \tag{38}$$

Integrating the latter twice gives

$$\zeta^{(1)}(\tau)=\int_{0}^{\tau}d\tau'\int_{0}^{\tau'}\frac{d\tau''}{2}\left[a\left(\tau''\right)e^{i(\zeta_{0}+\nu_{0}\tau'')}+a^{*}\left(\tau''\right)e^{-i(\zeta_{0}+\nu_{0}\tau'')}\right]. \tag{39}$$

Substituting that result into (37) and assuming the electron phases are evenly distributed, we obtain

$$\mathring{a}(\tau) = \frac{ij}{2}\int_0^\tau d\tau'\int_0^{\tau'} d\tau''\left\langle e^{i\nu_0(\tau''-\tau)}\right\rangle_{\nu_0} a(\tau'') . \tag{40}$$

If the electrons have a distribution *f*(*q*) of initial phase velocities $\nu_i = \nu_0 + q$ about ν_0, the Fourier transform of this distribution is $F(\tau) = \int_{-\infty}^{+\infty} e^{-iq\tau} f(q)dq$. Using this "characteristic function" and the substitution $\tau' = \tau - \tau''$ we can rewrite (40) in the form

$$\mathring{a}(\tau) = -\frac{ij}{2}\int_0^\tau d\tau''\int_0^{\tau''} d\tau' F(\tau')e^{-i\nu_0\tau'}a(\tau-\tau') . \tag{41}$$

Switching the order of integration and evaluating the inner integral,

$$\mathring{a}(\tau) = -\frac{ij}{2}\int_0^\tau d\tau'\tau' F(\tau')e^{-i\nu_0\tau'}a(\tau-\tau') . \tag{42}$$

This is known as the FEL integral equation [18]. It is valid only for weak optical fields, but for both the high-gain and low-gain regimes.

2. High Gain

We've previously derived a formula for low gain $(j \lesssim \pi)$ in weak fields (26). In the high gain regime $(j \gg \pi)$, the optical field amplitude and phase evolve rapidly. For a perfect electron beam, $F(\tau) = 1$, (42) can be integrated to describe high gain at resonance $(\nu_0 = 0)$ as a function of time [1],

$$G(\tau) \approx \frac{1}{9}\exp\left(\sqrt{3}\left(j/2\right)^{1/3}\tau\right) . \tag{43}$$

The growth of the field is exponential and is maximum at resonance for large *j*.

3. Electron Beam Quality Effects

The FEL integral equation (42) is useful for studying the effects of electron beam quality (energy spread and emittance). Note that it contains no reference to individual electrons, so it can be used to determine the field evolution for a given distribution of initial electron phase velocities, without having to follow the motion of each electron via the pendulum equation. Looking at the integrand, we see that the term $a(\tau - \tau')$

contributes to the growth of the field $a(\tau)$. This self-feedback leads to exponential growth of the optical field. However, poor beam quality will cause the magnitude of the characteristic function $F(\tau)$ to decay rapidly, decreasing the growth rate. The characteristic function corresponds to the bunching of the electron beam as it passes through the undulator. As the magnitude of $F(\tau)$ decreases over time, so does the bunching of the electron beam that gives rise to growth of the optical field in an FEL. The characteristic function provides a visual means for observing how different types of electron distributions will affect bunching, gain, and optical phase evolution.

In the early 1990's, we studied the effects of various types of electron distributions on the FEL mechanism. Current beam diagnostics in experiments do not tell us the precise shape of these functions, so it is important to study a variety of cases in order to understand the full range of possible effects. The author was deeply involved in this research, analyzing the characteristic functions produced by various types of electron distributions, and their effect on FEL bunching and gain, and was the lead author of an article we published on this work. [12]

As an example, a Gaussian energy spread of rms width $\Delta\gamma$ leads to a Gaussian phase velocity distribution

$$f(q) = \frac{e^{-q^2/2\sigma_G^2}}{\sqrt{2\pi}\,\sigma_G} \tag{44}$$

where $\sigma_G = 4\pi N \Delta\gamma/\gamma$ is the rms spread in phase velocities about ν_0 with $q = \nu - \nu_0$. This in turn yields a Gaussian characteristic function.

Figure 6 shows that a narrow phase velocity spread, $f(q)$ in the upper-left, yields a broad characteristic function, $F(\tau)$ in the upper-right, so bunching is preserved and the optical field grows rapidly. In contrast, a broad phase velocity spread, $f(q)$ in the lower-left, produces a narrow characteristic function, $F(\tau)$ in the lower-right, so bunching is quickly destroyed and there is much less gain.

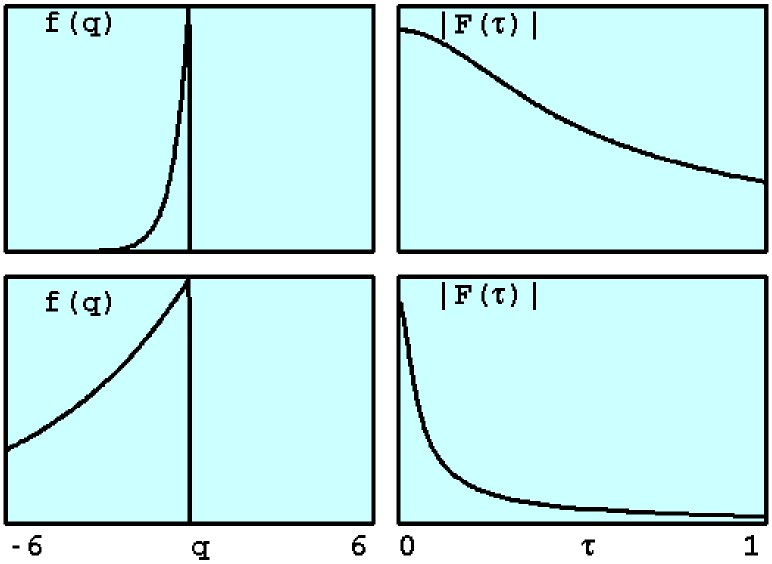

Figure 6. Phase velocity distribution f(q) and characteristic function F(τ) for good beam quality (top) and poor beam quality (bottom). With poor beam quality, F(τ) falls off faster, implying less bunching and reduced gain. (From [12].)

To study emittance effects, we use a distribution function $p\left(x, y, \theta_x, \theta_y\right)$ where (x, y) is the position of an electron when it enters the undulator and $\left(\theta_x, \theta_y\right)$ is the injection angle. Emittance effects would normally require a 3D simulation in order to include the changes in the FEL mechanism as the electrons drift off axis. However, it is possible to convert the distribution function to the corresponding phase velocity distribution, and then obtain the characteristic function. For example, an electron beam with a linear spread has a small angular spread in the *x* direction only. The resulting phase velocity distribution is given by

$$f(q) = \frac{e^{q/\sigma_\theta}}{\sqrt{-\pi\, q \sigma_\theta}} \tag{45}$$

for $q < 0$ and 0 otherwise, where $\sigma_\theta = 4\pi N \gamma^2 (\Delta\theta)^2 \big/ \left(1 + K^2\right)$ is the spread in phase velocities induced by the angular spread of rms width $\Delta\theta$. The amplitude and phase of the characteristic function for this and several other distributions is shown in Figures 7 and 8.

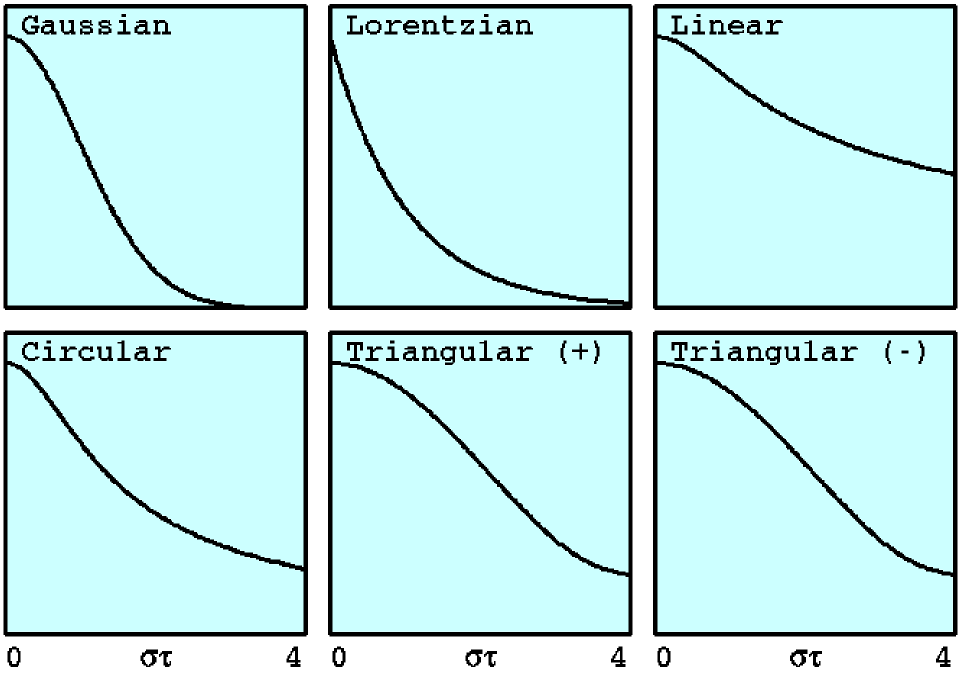

Figure 7. Amplitude of the characteristic function F(στ) for various electron distributions, as described in the text. (From [12].)

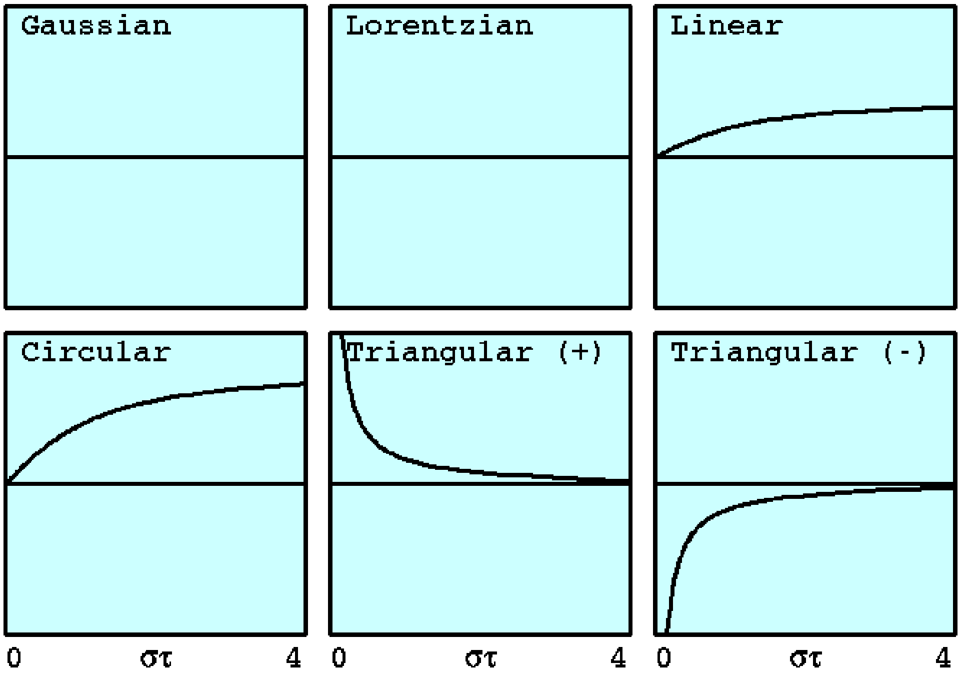

Figure 8. Phase of the characteristic function F(στ) for various electron distributions, as described in the text. (From [12].)

The circular distribution arises when there is an equal distribution in angles in the x and y directions. The triangular distributions occur when an emittance filter is used to reject all electrons outside a given radius, and outside a given angle; the negative slope occurs with betatron focusing, whereas the positive slope occurs if there is no focusing. Notice in Figures 7 and 8 that the various distribution functions produce remarkably different characteristic functions, and hence affect the FEL gain and phase evolution in different ways. This indicates that experimentalists should pay attention not only to the width, but also the shape of the electron beam distributions.

E. STRONG OPTICAL FIELDS

1. Saturation

The dimensionless optical field strength $|a|$ drives the electron bunching according to the FEL pendulum equation (18). Electron bunching causes the optical field to grow via the FEL wave equation (35). As the field grows, the peak-to-peak height of the separatrix $4|a|^{1/2}$ increases, trapping a large fraction of the electrons in the closed orbit region of phase space, as shown in Figure 9. This simulation uses a more realistic electron beam than before, with 1000 sample electrons injected with a Gaussian energy spread $\sigma_G = 1$ about the initial phase velocity $\nu_0 = 5$. The initial electrons are shown in yellow. The initial optical field strength is $a_0 = 20$. The pendulum and wave equations are still valid in strong fields, and the trapped electrons continue to follow the pendulum phase space paths. Halfway through the undulator, the electrons shown in light brown are clearly bunched near the optimum phase for gain, $\zeta = \pi$, so they give up energy to the optical wave, causing some electrons to lag behind others in the beam. When they reach the end of the undulator, the electrons (now shown in red) are bunched at the optimum phase for absorption, $\zeta = 0$. This “over-bunching” leads to reduced gain and the onset of saturation.

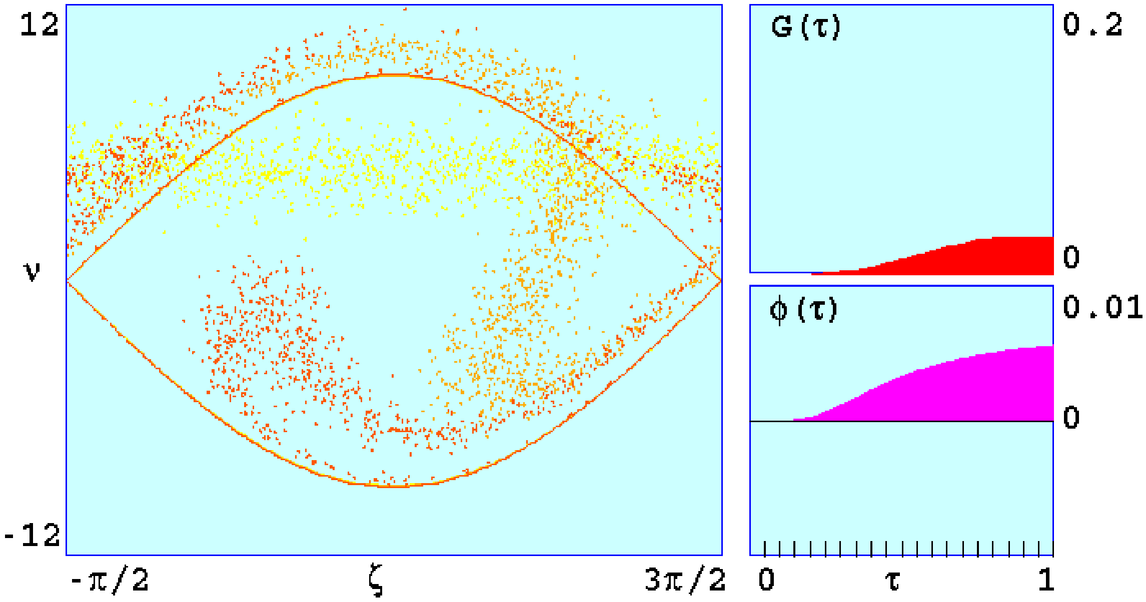

Figure 9. Electron evolution in (ζ,ν) phase space, optical field gain $G(\tau)$ and phase $\phi(\tau)$ for a single pass through a high power FEL $(a_0 = 20)$. The electrons "over-bunch" and the gain is reduced, indicating the onset of saturation.

At the onset of saturation, the mean phase velocity of the electron bunch is reduced on the order of the peak-to-peak height of the separatrix, $\Delta\nu = 4|a|^{1/2} \approx 2\pi$. This is related to the energy extracted from the bunch by $\Delta\nu = 4\pi N \Delta\gamma/\gamma \approx 2\pi$, which gives a maximum theoretical efficiency $\eta \equiv \Delta\gamma/\gamma \approx 1/2N$. So a typical FEL with $N = 100$ periods has an extraction efficiency of $\eta \approx 0.5\%$. For a high-gain FEL $(j \gg 1)$, the onset of saturation occurs at a larger field strength, $|a| \approx 2(j/2)^{2/3}$, and the theoretical efficiency is $\eta = (j/2)^{1/3}/8N$. [1]

2. Tapering

To enhance the extraction efficiency, it is possible to taper either the undulator period or field strength along the axis, thus maintaining resonance as the electrons lose energy to the optical field. This gives an artificial acceleration to the electron phase, equivalent to adding a constant torque to the pendulum equation, which now becomes

$$\frac{d^2\zeta}{d\tau^2} = \delta + |a|\cos(\zeta + \phi) \tag{46}$$

where the phase acceleration is $\delta \approx -2\pi N \Delta\lambda_0/\lambda_0$ if the undulator period is decreased, or $\delta \approx -\left[4\pi N K^2/\left(1+K^2\right)\right](\Delta K/K)$ if the undulator field strength is decreased [1].

If the taper rate is too large, $\delta > |a|$, there will be no electrons trapped in closed orbits near resonance, and there will not be significant gain. If the taper rate is too small, $\delta \lesssim 4|a|^{1/2}$, it will not overcome the natural deceleration of the electrons, and there is no advantage to tapering. Also, tapering is only useful in strong optical fields, $|a| \gtrsim \pi$, when saturation begins to reduce the gain. All of these criteria for tapering can be summarized in the following expression:

$$2\pi \lesssim 4|a|^{1/2} \lesssim \delta < |a| . \tag{47}$$

Tapering postpones saturation and enhances the natural efficiency of an FEL; however, it also reduces the weak-field gain, so the technique is more commonly used with FEL amplifiers rather than oscillators. Negative tapering has also been investigated, and has been shown to be useful in some cases [19].

3. Trapped-Particle Instability

In strong optical fields, many electrons are trapped in the closed-orbit region of phase space, as shown in Figure 9. The trapped electrons begin to oscillate inside the separatrix. A perturbation expansion of the pendulum equation near the stable fixed point $(\zeta,\nu) = (\pi/2, 0)$ gives an equation for these synchrotron oscillations [1],

$$\zeta(\tau) \approx \zeta_0 + \frac{\nu_0}{\nu_s}\sin(\nu_s \tau) \tag{48}$$

where (ζ_0, ν_0) is the initial position, and $\nu_s = |a|^{1/2}$ is the synchrotron frequency. This modulation of the electron beam causes sidebands to appear around the fundamental at $\nu_0 \pm \nu_s$, corresponding to a wavelength shift $\Delta\lambda/\lambda = \nu_s/2\pi N$, which is the ratio of the number of synchrotron oscillations to the number of undulator periods. An optical field strength of $|a| = 4\pi^2$ is required for one complete oscillation. High power FEL amplifiers can have many tens of synchrotron oscillations, causing significant sideband growth and fluctuations of the output power. In an FEL oscillator, repeated low gain with about one synchrotron oscillation each pass is sufficient to generate sidebands.

This "trapped-particle instability" can destroy FEL coherence, but also enhances the total output power, so it can be desirable in some applications where high power is more important than a narrow spectrum. Sidebands can be suppressed by decreasing the current or increasing the cavity losses, or by tapering the undulator, which decreases the fraction of trapped electrons. In the latter case, the synchrotron frequency is decreased to $\nu_s \approx \left(|a|^2 - \delta^2\right)^{1/4}$. [1]

F. SHORT PULSES

RF linacs are capable of producing very short electron pulses, on the order of picoseconds, which can create very short optical pulses in an FEL. The relativistic electrons travel slightly slower than the photons. The resonance condition implies that during one pass through the undulator, the electron pulse will lag behind the optical pulse by a slippage distance $N\lambda$. If the electron pulse length is on the order of or less than the slippage distance, then it will not overlap the optical pulse over the entire pass through the undulator, and gain will be reduced. The electrons at the leading edge of the pulse see the full optical field strength and bunch accordingly. As the bunched electrons slip back relative to the optical pulse, they amplify the trailing edge of the optical pulse. Thus the optical pulse centroid travels slower than the speed of light, a process called "pulse lethargy" [1].

1. Desynchronism

If the electron pulses are timed so the next pulse arrives at the beginning of the undulator at the same time as the rebounding optical pulse (exact synchronism), the optical pulse will gradually fall behind the electron pulse, and optical power will decay. To compensate, the optical pulse must arrive slightly ahead of the electron pulse. In practice, this is done by adjusting the cavity length S until the maximum output signal is obtained (“tuning” the cavity). The artificial advancement or “desynchronism” of the light pulse, relative to the slippage distance, is given by $d = -2\Delta S / N\lambda$.

For large values of desynchronism, $d \approx 0.1$, the optical pulse advances significantly ahead of the electron pulse each pass, and only the trailing edge of the optical pulse is amplified. This results in a broad, low-power optical pulse, with a narrow spectrum. The power is generally too low to trigger the trapped-particle instability. This regime could be desirable when stable, low-power operation is required. If *d* is too large, $d \gg 0.1$, the electron and optical pulses won’t overlap much, so that gain will be below threshold, and there will be no output power.

At moderate values of desynchronism, $d \approx 0.01$, the optical field strength becomes large enough to induce synchrotron oscillations, creating modulations of the optical pulse. The desynchronism causes these modulations to continuously drift from the trailing to the leading edge of the pulse. The optical power, spectrum, and pulse shape oscillate periodically over hundreds of passes; this is known as limit cycle behavior [20].

At smaller values of desynchronism, $d \approx 10^{-3}$, the total output power can be larger, but the optical pulse can become chaotic due to the trapped-particle instability. In this case the optical pulse is short and modulated by sharp spikes. [21]

THIS PAGE INTENTIONALLY LEFT BLANK

III. SINGLE-MODE SIMULATIONS

Prior to developing a large comprehensive simulation that covers all aspects of the FEL interaction, we have for many years used a set of smaller simulations that model various physical effects separately, enabling us to analyze the origins and consequences of those effects. These simulations are well understood, easy to modify, and can run on personal computers. They have been benchmarked against FEL theoretical formulas, and by comparison to numerous FEL experiments.

This chapter describes our single-mode simulations, which model the interaction of a single optical mode (a single-frequency plane wave) with the relativistic electron beam as it travels through the undulator. Although higher-order modes are present in any real experiment, we learn much about the basic FEL physics from these single-mode simulations.

A. PHASE SPACE EVOLUTION

Our simplest simulation, called *psall*, follows sample electrons as they evolve in phase space (ζ,ν) and exchange energy with the optical field over one pass through the undulator. The optical field can start with a given amplitude and phase, or it can be allowed to develop from spontaneous emission. The sample electrons are initially distributed uniformly in phase from $\zeta = 0$ to 2π, but may have a random spread in phase velocities determined by beam emittance and energy spread. The undulator can have a positive or negative taper. In each numerical time step, the pendulum equation (18) determines the microscopic motion of the electrons in phase space, while the wave equation (35) is used to self-consistently update the optical field amplitude and phase. The output of *psall*, as shown in Figure 9, displays the evolution of the electrons in phase space, and plots the optical field gain and phase versus time. This simulation is useful for understanding basic FEL physical processes, such as electron bunching, optical field growth and saturation, as discussed in the previous chapter.

B. GAIN SURFACES

We wrote another computer program called *gain* which runs the same single-mode simulation numerous times, varying the initial electron phase velocity ν_0, to produce a gain spectrum like that shown in Figure 4. In another program called *Gav*, the initial optical field strength a_0 is also varied to produce a gain surface as shown in Figure 10. The single-pass gain is plotted versus initial electron phase velocity ν_0 and optical field strength a_0, for a low-gain FEL $(j=1)$. The white lines on the surface represent contours of equal gain. Notice that as the optical field strength is increased beyond saturation $(a_0 \gtrsim \pi)$, the gain decreases. The gain spectrum becomes broader since the height of the separatrix increases with $\sqrt{a_0}$. The value of ν_0 that maximizes the gain also increases, which corresponds to a longer wavelength of laser operation; this effect has been observed in FEL experiments [22].

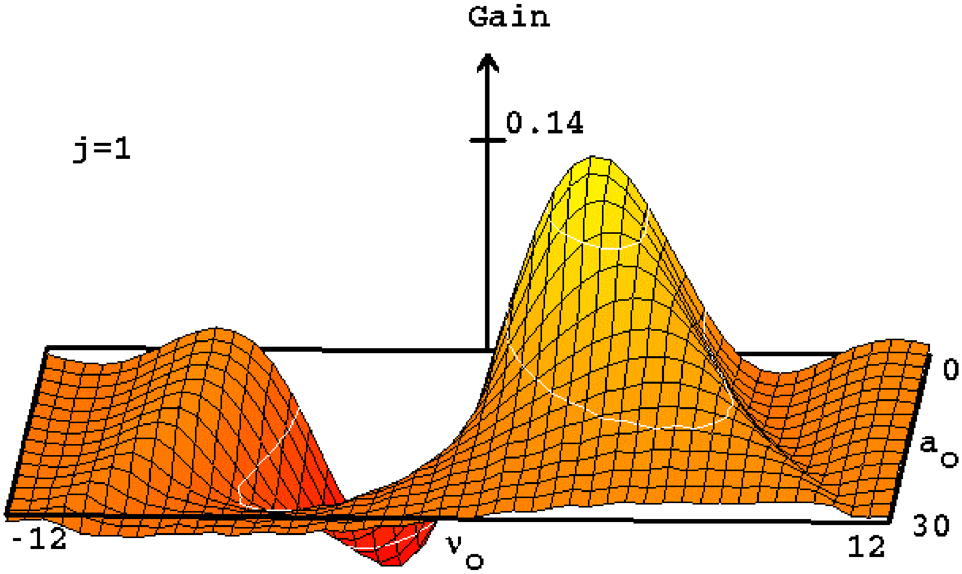

Figure 10. Single-pass gain versus initial electron phase velocity ν_0 and optical field strength a_0, for a low-gain FEL $(j=1)$. As a_0 increases, the gain spectrum becomes broader, the peak gain decreases and shifts to a larger value of ν_0.

For a high-gain FEL $(j \gg 1)$, the shape of the gain surface changes significantly. Figure 11 gives an example of a gain surface for an FEL with $j = 100$. On the vertical axis we plot the logarithm of the gain, $\ln(1+G)$, because the gain can now change over several orders of magnitude. Observe that in weak fields $(a_0 \lesssim \pi)$, the spectrum is now broader (compared to Figure 10) and more symmetric around resonance, $\nu_0 = 0$. As the field strength increases, the peak again moves away from resonance. Also notice the sharp dip in the surface near $\nu_0 \approx -10$ in weak fields; since the vertical axis is logarithmic, this corresponds to gain ≈ 0.

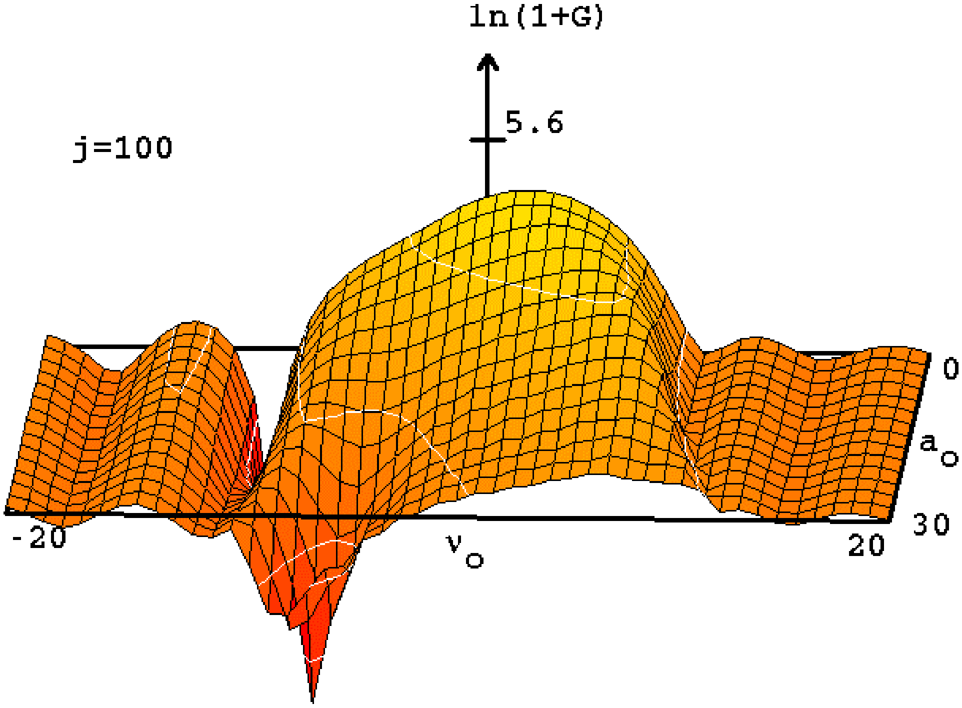

Figure 11. Single-pass gain, $\ln(1+G)$, versus initial phase velocity ν_0 and optical field strength a_0, for a high-gain FEL $(j = 100)$. In weak fields, the gain spectrum is broad and nearly symmetric about the peak gain at $\nu_0 \approx 0$. As a_0 increases, the peak gain decreases and moves away from resonance.

1. Gain Degradation Due to Electron Beam Quality

Instead of varying the initial optical field, we can vary other parameters such as the electron beam energy spread or an angular spread due to beam emittance. For example, Figure 12 shows gain surfaces for circular and linear spreads. Recall from our earlier discussion that a linear spread is an angular spread in the *x* direction only, whereas a circular spread in an angular spread in both the *x* and *y* directions. In Figures 12 (a) and (b) we see that as the angular spread σ_θ increases, the gain naturally falls off, but the spectrum details are different. Note the different scales on the σ_θ axes. It is clear that a linear angular spread is less susceptible to gain degradation than a circular spread.

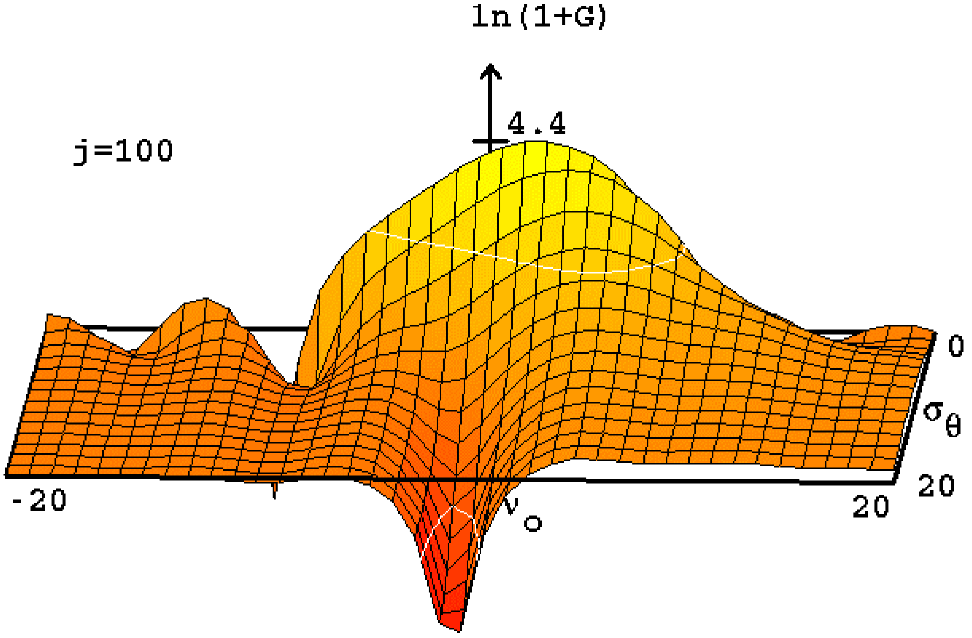

Figure 12(a). Single-pass gain, $\ln(1+G)$, versus initial phase velocity ν_0 and angular spread σ_θ, for a circular spread. As σ_θ increases, the gain falls off rapidly. (From [23].)

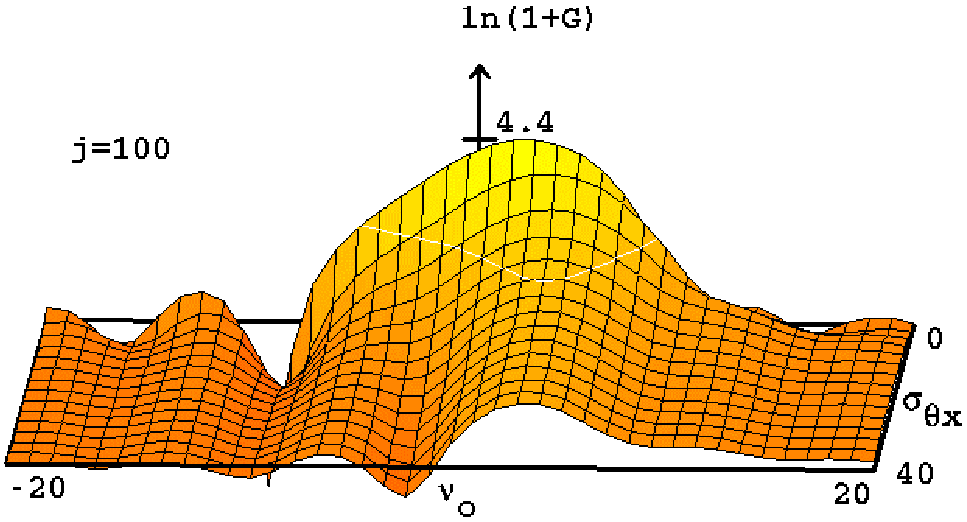

Figure 12(b). Single-pass gain $\ln(1+G)$ versus initial phase velocity ν_0 and angular spread $\sigma_{\theta x}$, for a linear spread. As $\sigma_{\theta x}$ increases, the gain falls off, but not as rapidly as it does for the circular spread. (From [23].)

2. FEL Klystron

Single-mode simulations are also useful for examining basic physical effects in new undulator designs. For example, an FEL klystron consists of two identical undulators separated by dispersive magnets equivalent to a drift section of length N_d undulator periods [24]. In the dispersion section between the undulators (at $\tau = 0.5$), each electron's phase evolves by $\Delta\zeta = \nu D$, where ν is the electron's phase velocity and $D = N_d / N$ is the dimensionless dispersive length. This enhances electron bunching and thus the gain in weak optical fields. However in strong optical fields, it precipitates overbunching and thus reduces efficiency. Figure 13 shows a gain surface for a typical FEL klystron. Compared to the standard FEL shown in Figure 10 for the same current density $(j = 1)$, the peak gain in weak fields is now about three times greater, the gain in strong fields is significantly reduced, and there is more structure in the gain spectrum, with multiple peaks of nearly equal gain.

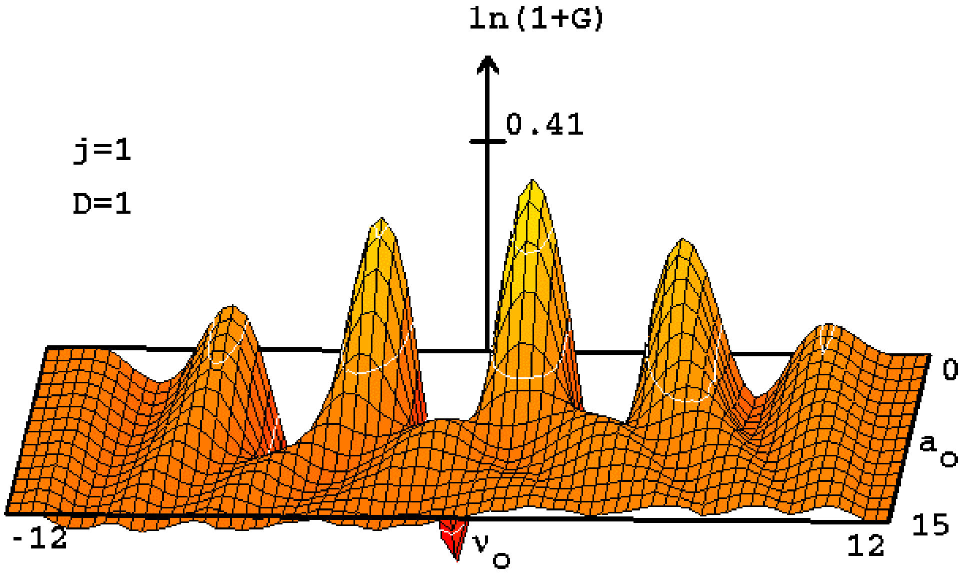

Figure 13. Single-pass gain, $\ln(1+G)$, versus initial phase velocity ν_0 and optical field strength a_0, for an FEL klystron $(D=1)$. Compared to the standard FEL in Figure 10, there is now more gain in weak fields, but less gain in strong fields, and the spectrum has more structure.

In the mid-1990's we studied the SELENE FEL, a ground-based laser designed for satellite power beaming [25,26]. This experiment used a three-stage klystron oscillator with dispersive magnets at $\tau = 1/3$, $\tau = 2/3$, and $\tau = 1$, followed by a single pass FEL amplifier referred to as the radiator. Our simulations showed the klystron oscillator strongly bunches the electrons so they begin spontaneous radiation early in the radiator and are amplified along the entire length, with final amplified power from the radiator about 500 times the level in the oscillator. The klystron configuration also limits the saturated power within the oscillator. This scheme could produce a powerful output beam without damaging the oscillator mirrors.

3. Positive and Negative Undulator Tapers

Last year we published a paper in which we used single-mode simulations to compare positive and negative undulator tapers [27]. As discussed in the above section on strong optical fields, the conventional method for enhancing FEL efficiency is to decrease the magnetic field strength along the undulator to maintain resonance and extract more energy from the electrons. A decreasing magnetic field strength, $\Delta K/K < 0$, adds a positive phase acceleration

$$\delta = -\left(\frac{4\pi NK^2}{1+K^2}\right)\left(\frac{\Delta K}{K}\right) > 0 \tag{49}$$

to the pendulum equation (46), so we refer to this as a positive taper. Figure 14 shows a typical electron phase space after one pass through an undulator with a positive taper, $\delta = 8\pi$, in strong optical fields, $a_0 = 40$. This field strength would normally be beyond saturation, but the gain plotted on the right shows that the field is still growing.

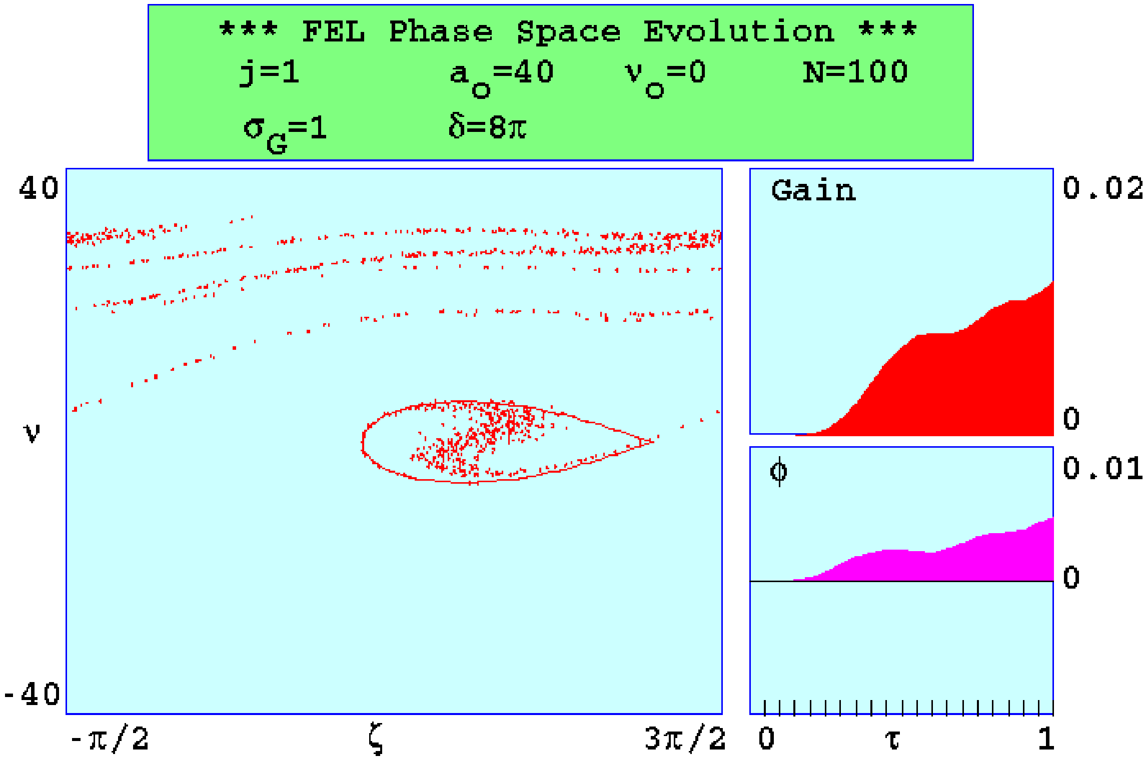

Figure 14. Electron phase space, optical field gain and phase evolution for an FEL with a positive undulator taper, $\delta = 8\pi$, in strong optical fields, $a_0 = 40$. About half of the electrons are trapped inside the separatrix, and there is still positive gain, even though the field strength is beyond the normal saturation level.

Notice in Figure 14 that the separatrix is shrunk and distorted. About half of the electrons are trapped in closed orbits inside the separatrix; the other half are in open orbits and do not interact much with the optical field. The smaller separatrix confines the trapped electrons near the optimum phase for gain, $\zeta = \pi$. The fluctuations in the gain are due to synchrotron oscillations of the trapped electron bunch inside the separatrix.

Figure 15 shows the phase space evolution for an undulator with a negative taper of $\delta = -8\pi$. This corresponds to an increasing magnetic field strength along the undulator, $\Delta K/K < 0$. The separatrix is now reversed from the previous case, and there are no trapped electrons inside it. However, the phase space paths of the electrons cause them to bunch near $\zeta = \pi$ about halfway down the undulator, as shown by the light brown dots, and they still produce gain.

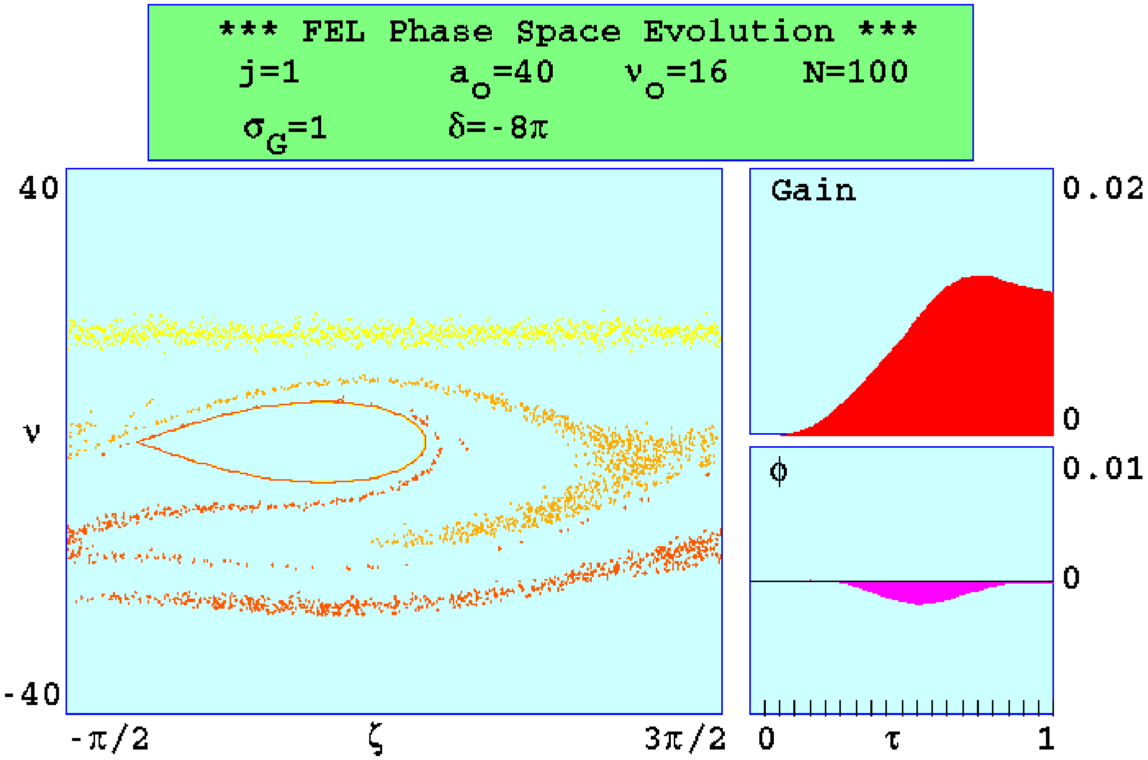

Figure 15. Electron phase space, optical field gain and phase evolution for an FEL with a negative undulator taper, $\delta = -8\pi$, in strong optical fields, $a_0 = 40$. No electrons are trapped inside the separatrix, but they still bunch and produce gain.

Figure 16 shows FEL gain surfaces for positive and negative tapers. The two surfaces are related by $G(\nu_0, \delta, a_0) \approx -G(-\nu_0, -\delta, a_0)$. In both cases, the weak-field gain is reduced but the strong-field gain is enhanced compared to the untapered case (Figure 10). The large tapers produce complicated gain spectra, with multiple peaks shifted away from resonance. For the positive taper, Figure 16(a) shows that the peak gain drifts to larger phase velocity ν_0, corresponding to a wavelength shift $\Delta\lambda/\lambda \approx 4\%$, as the FEL evolves from weak fields to strong fields. For the negative taper, Figure 16(b) shows that the peak gain remains at about the same ν_0 as a_0 increases, so there is no wavelength shift.

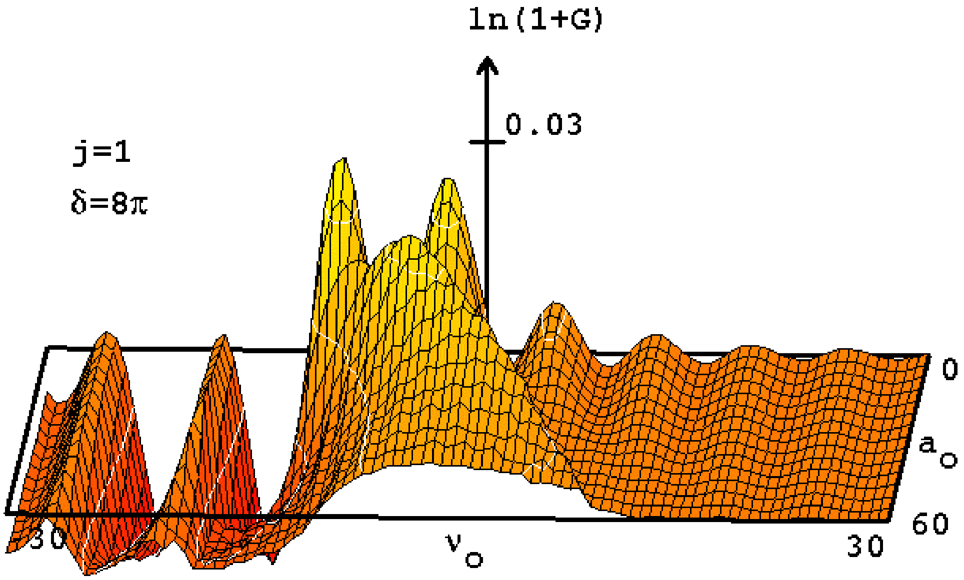

Figure 16(a). Single-pass gain $\ln(1+G)$ versus initial phase velocity ν_0 and optical field strength a_0, for an FEL with a positive undulator taper, $\delta = 8\pi$. Compared to an untapered FEL (Figure 10), there is less gain in weak fields, but more gain in strong fields. As a_0 increases, the peak gain shifts to a larger value of ν_0.

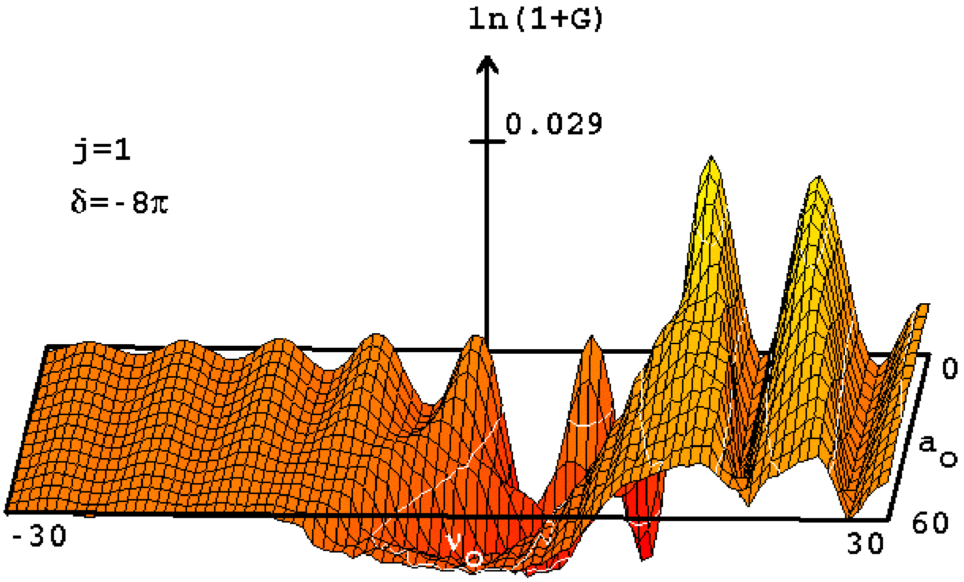

Figure 16(b). Single-pass gain $\ln(1+G)$ versus initial phase velocity ν_0 and optical field strength a_0, for an FEL with a negative undulator taper, $\delta = -8\pi$. Compared to an untapered FEL (Figure 10), there is less gain in weak fields, but more gain in strong fields. As a_0 increases, the peak gain stays near the same value of ν_0.

IV. LONGITUDINAL MULTIMODE SIMULATIONS

In an actual FEL experiment with a finite optical pulse length, there are multiple longitudinal modes inside the optical cavity. We have developed several numerical simulations that follow the evolution of longitudinal modes in an FEL. The optical field amplitude and phase are allowed to vary along the undulator (z) axis. The initial optical field can be specified or allowed to develop from spontaneous emission. The pendulum equation (18) and the wave equation (35) are used to self-consistently determine the evolution of the electrons and the optical field at each longitudinal position. We follow the behavior of the optical pulse in a co-propagating window moving at the speed of light. By taking a Fourier transform of the square of the optical pulse amplitude, we can obtain the optical power spectrum, and thus observe mode competition and coherence evolution.

A. LONG PULSES

Consider an electron pulse of length l_e entering the undulator with a co-propagating optical pulse. In a single pass through the undulator, the slower moving electron pulse slips back relative to the optical pulse by the slippage distance, $N\lambda$. If the electron pulse is much longer than the slippage distance, $\sigma_z = l_e/N\lambda \gg 1$, a long optical pulse will form. In that case, we make the optical pulse window a small, integral number of slippage distances long, and we assume periodic boundary conditions at each end of the window. Since the electron pulse is much longer than the optical pulse window, we take the current density $j(z)$ to be constant in that window.

1. Single Pass

For studying long pulse FEL amplifiers, we have a simulation called *wrapev1* that follows the electron and optical pulses over a single pass through the undulator. The output of *wrapev1* shows the evolution of the optical pulse, the optical power spectrum, the electron energy distribution, the optical power and gain versus dimensionless time τ.

a. SLAC X-ray FEL

In the X-ray FEL proposed at SLAC in 1993 [28], high-energy 7 GeV electrons would be used to produce radiation at a wavelength of 4 nm with a peak power of 28 GW. Since there are no low-power input sources at that wavelength, and no mirrors are available to create an optical cavity, the FEL must create light from spontaneous emission and amplify it to high power over a single pass through the undulator, in a process known as self-amplification of spontaneous emission (SASE) [29]. Figure 17 shows the output from a simulation of this FEL. The high peak current of 2500 A, the 60m long undulator with $N = 723$ periods, and other design parameters give dimensionless current density $j = 2400$, so this is a high-gain FEL. The electrons have a moderate energy spread $\sigma_G = 3.6$, and a small angular spread $\sigma_\theta = 1$. The 0.16 ps duration electron pulse corresponds to dimensionless pulse length $\sigma_z \approx 16$.

In the middle left of Figure 17 we show the evolution of the optical field amplitude $|a(z,\tau)|$ over a single pass from $\tau = 0$ to 1, as an intensity/contour plot inside a window two slippage distances long $(z = -1 \text{ to } 1)$, which moves with the pulse at the speed of light. The optical field amplitude is represented by the color scale at the top of the figure, with the largest amplitude, $|a| = 362$, shown as red and zero field shown as blue. Observe that the optical field grows from spontaneous emission to form a broad pulse with fluctuations due to shot noise, as shown in blue in the upper left. In the lower left is the evolution of the optical gain, $\ln(1+G(\tau))$. In the lower center the theoretical weak-field gain spectrum $\ln(1+G(\nu))$ for $j = 2400$ is shown in black for reference. In the center of the figure is an intensity/contour plot of the optical power spectrum $P(\nu,\tau)$, which shows coherence developing over a single pass. The final optical spectrum, shown in magenta in the upper-center, has a linewidth corresponding to $\Delta\lambda/\lambda \approx 0.07\%$. The triangular tick mark at the top points to the center of the initial power spectrum, and the rectangular tick mark points to the center of the final power spectrum. In the lower right is the total optical power $P(\tau)$ versus time, showing saturation near the end of the undulator. If higher power is required, the undulator could be tapered to delay the onset of saturation, at the cost of a broader linewidth. In the middle-right, another intensity/contour plot shows the evolution of the electron phase velocity distribution $f(\nu,\tau)$. As we discussed before, a change in an electron's phase velocity corresponds to a change in its energy, so the final broad phase velocity distribution, shown in red in the upper-right, indicates that significant energy has been extracted from the electrons.

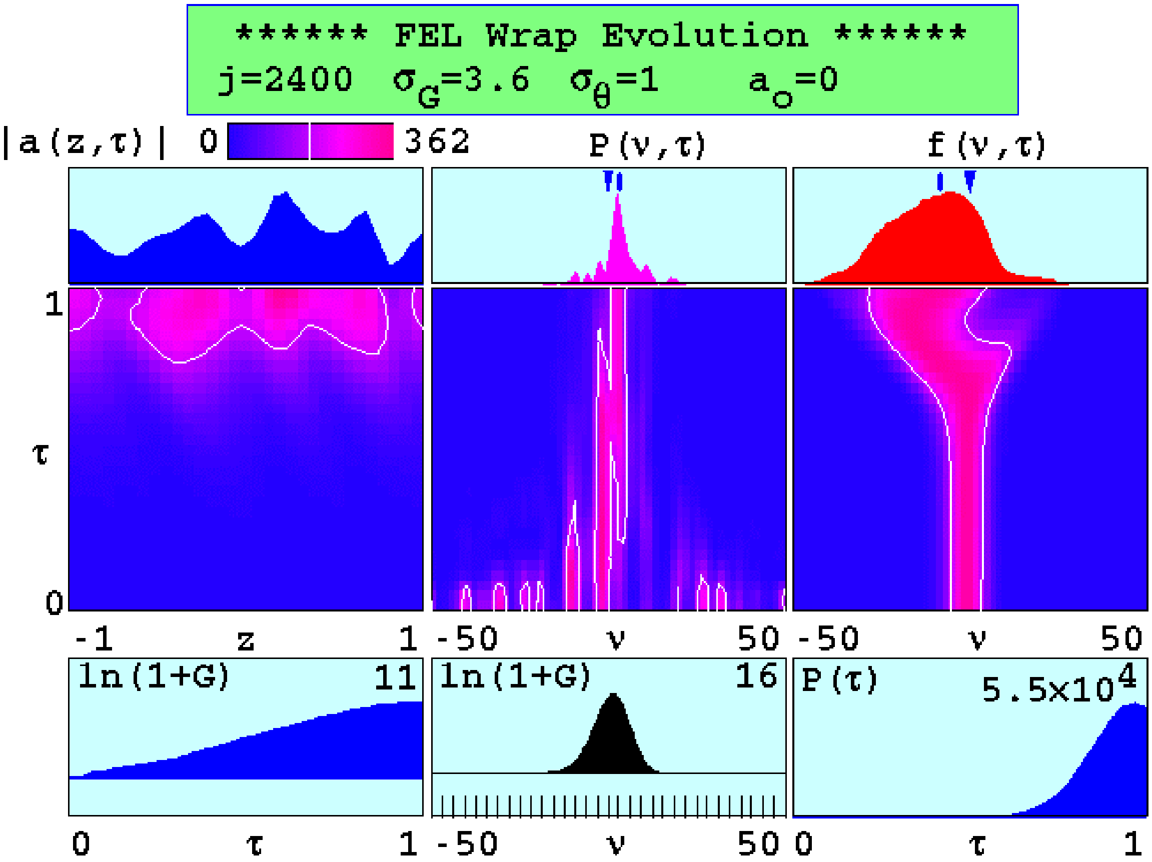

Figure 17. Longitudinal multimode simulation results for the SLAC X-ray FEL. The various plots are described in the text. The optical power spectrum, $P(\nu,\tau)$, shows coherence evolving as the laser line narrows over a single pass through the undulator. (From [30].)

2. Multiple Passes

For studying long pulse FEL oscillators, we have another simulation called *wrapevn* that follows the electron and optical pulses over many passes through the undulator, again using periodic boundary conditions at each end of the optical pulse window. Mirror transmission losses at the end of each pass are determined by the resonator quality factor *Q*. The output of the program shows the evolution of the optical pulse, the optical and electron spectra, and the optical power and gain plotted versus pass number *n*.

a. Boeing 1 kW FEL Oscillator

In the early 1990's, Boeing designed an FEL oscillator to produce 1 kW average power at a wavelength of 0.6 μm. It was planned to be a high-gain FEL, $j = 658$, with $N = 220$ undulator periods, and a fairly large initial electron energy spread, $\sigma_G = 11$. The proposed resonator quality factor $Q = 5$ corresponded to ~20% losses per pass. Figure 18 shows the results of a *wrapevn* simulation of this FEL. This figure is similar to the previous examples, but now the evolution is over $n = 400$ passes, instead of over a single pass. The bottom left corner shows the gain, $G(n)$, at the end of each pass through the undulator. The FEL starts at resonance $\nu_0 = 0$ with an initial optical field of $a_0 = 1$. As the electrons slip back past the optical field sites and execute synchrotron oscillations, they continually modulate the optical wave envelope. Numerous modes begin to grow, and the power $P(n)$ increases dramatically as sidebands appear in the power spectrum $P(\nu, n)$. The final power spectrum $P(\nu)$ shows several prominent sidebands up to $\delta\nu \approx 200$ away from the fundamental, corresponding to about a 7% frequency spread. The evolution of the optical field amplitude $|a(z,n)|$ is chaotic, due to nonlinear interactions between the modes.

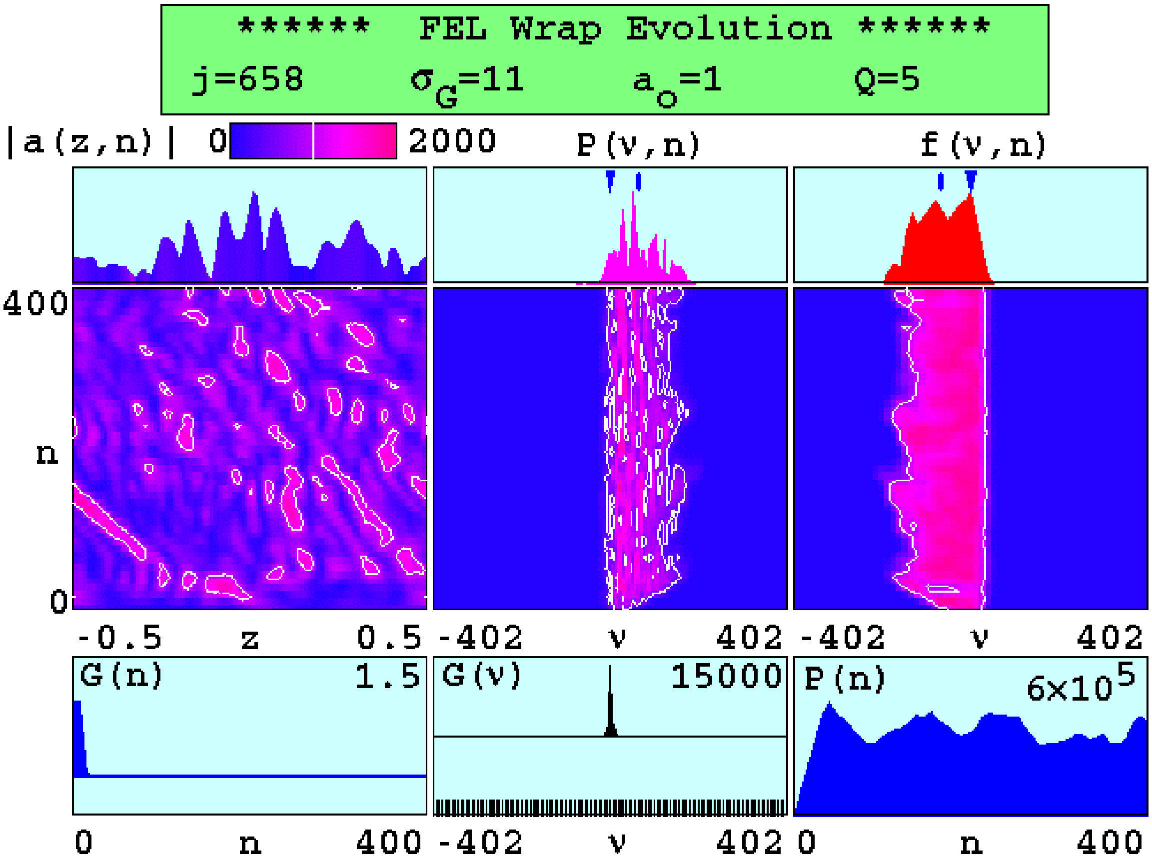

Figure 18. Longitudinal multimode simulation results for the Boeing 1 kW FEL oscillator. The optical field amplitude $|a(z,n)|$ shows the development of a chaotic field over $n = 400$ passes. (From [31].)

B. SHORT PULSES

If the electron pulse length σ_z is just a few slippage distances long or less than the slippage distance, then we must allow the current density to vary along the undulator axis. For numerical convenience, we choose a parabolic pulse shape given by $j(z) = \hat{j}\left(1 - 2z^2/\sigma_z^2\right)$ for $j(z) > 0$. The peak current density $\hat{j}$ and electron pulse length σ_z are specified. We follow the evolution of the optical pulse in a co-propagating window long enough to contain the entire pulse, so we do not use periodic boundary conditions for these simulations.

1. Single Pass

For studying short pulse FEL amplifiers, we have a simulation called *pulsev1* that follows the electron and optical pulses over a single pass through the undulator. The output of the program shows the evolution of the optical and electron pulses, the optical and electron spectra, as well as the optical power or gain versus dimensionless time τ .

a. Boeing APLE Amplifier

In the early 1990's, we studied pulse slippage effects in the Boeing Average Power Laser Experiment (APLE), an FEL that was designed to produce 100 kW of average power by amplifying a series of short, intense pulses in a single pass through a tapered undulator [32]. This author was directly involved in planning this research, developing and running the simulations, and interpreting their output, and was the lead author of a paper we published on the results of this work [33]. The 450 A peak current of each micropulse corresponds to $jF = 20000$, where *j* is the peak dimensionless current density, and the filling factor $F = 0.1$ is the cross-section area of the electron beam divided by the cross-section area of the optical mode. The electron beam has a Gaussian energy spread $\sigma_G = 6$ and an exponential angular spread $\sigma_\theta = 7$. The electron pulse length is twice the slippage distance, $\sigma_z = 2$. The initial optical pulse, produced by a separate FEL oscillator [34], has dimensionless amplitude $a_0 = 18$ and a pulse length of $\sigma_a = 6$ slippage distances. The 20% tapering rate gives a phase acceleration of $\delta = 200\pi$.

Figure 19 shows the output from a simulation of the Boeing APLE FEL. In the lower-left, the electron pulse $j(z)$ is shown in blue at the beginning of the undulator $(\tau = 0)$ and in red at the end of the undulator $(\tau = 1)$. Over a single pass through the undulator, the slower-moving electron pulse slips back relative to the optical pulse by the slippage distance $N\lambda$. The window width is 4 slippage distances. The optical pulse $|a(z,\tau)|$ starts out broad, but the final optical pulse in the upper left is about the same width as the electron pulse, since only the portion of the optical pulse that overlaps the electron pulse is amplified. The corresponding optical power spectrum

$P(\nu,\tau)$ becomes broader over time. The evolution of the electron phase velocity distribution $f(\nu,\tau)$ shows the taper starting at $\tau \approx 0.3$. Without the taper, the optical field would saturate at that point. The strong taper allows the field to continue to grow, as shown by the total power evolution $P(\tau)$. Tapering enhances the single-pass extraction efficiency to $\eta \approx 5\%$, to achieve the 100 kW goal averaged over many pulses. The final electron phase velocity distribution in the upper right shows that about half of the electrons are trapped near resonance $\nu = 0$.

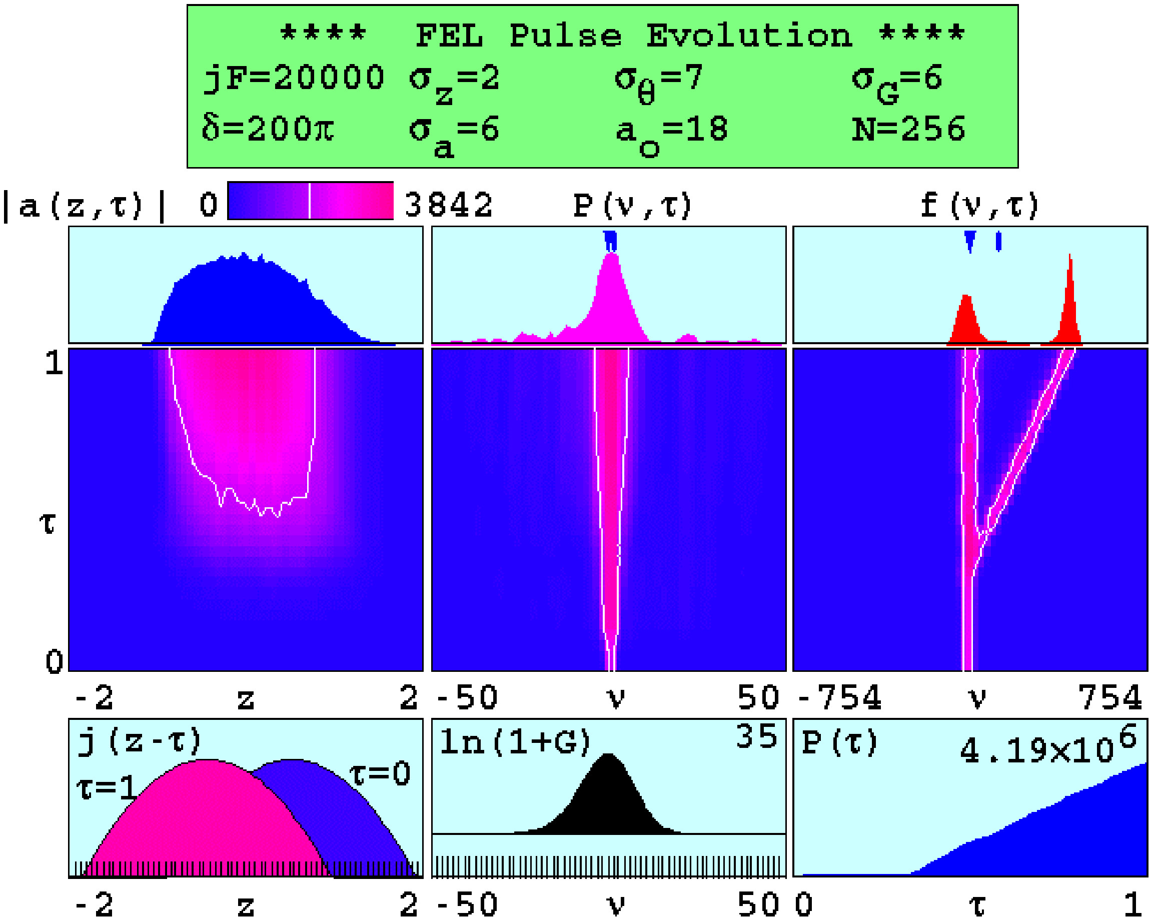

Figure 19. Longitudinal multimode simulation results for the Boeing APLE amplifier. The electron phase velocity distribution $f(\nu,\tau)$ and the optical power evolution $P(\tau)$ show the effect of the linear undulator taper, $\delta = 200\pi$, starting at $\tau \approx 0.3$. (From [33].)

2. Multiple Passes

For studying short-pulse FEL oscillators, we have a simulation called *pulsevn* that follows the electron and optical pulses over many passes through the undulator. The electron pulse length and the desynchronism determine the evolution of the optical pulse.

Figure 20 shows the output from a *pulsevn* simulation of an FEL with a short electron pulse, $\sigma_z = 1$, at exact synchronism, $d = 0$. The lethargy effect causes the optical pulse $|a(z,n)|$ to drift away from the electron pulse $j(z-\tau)$, and the optical power $P(n)$ decays over $n = 1000$ passes. The electron phase velocity distribution $f(\nu,n)$ is narrow, so very little energy is extracted from the electron beam.

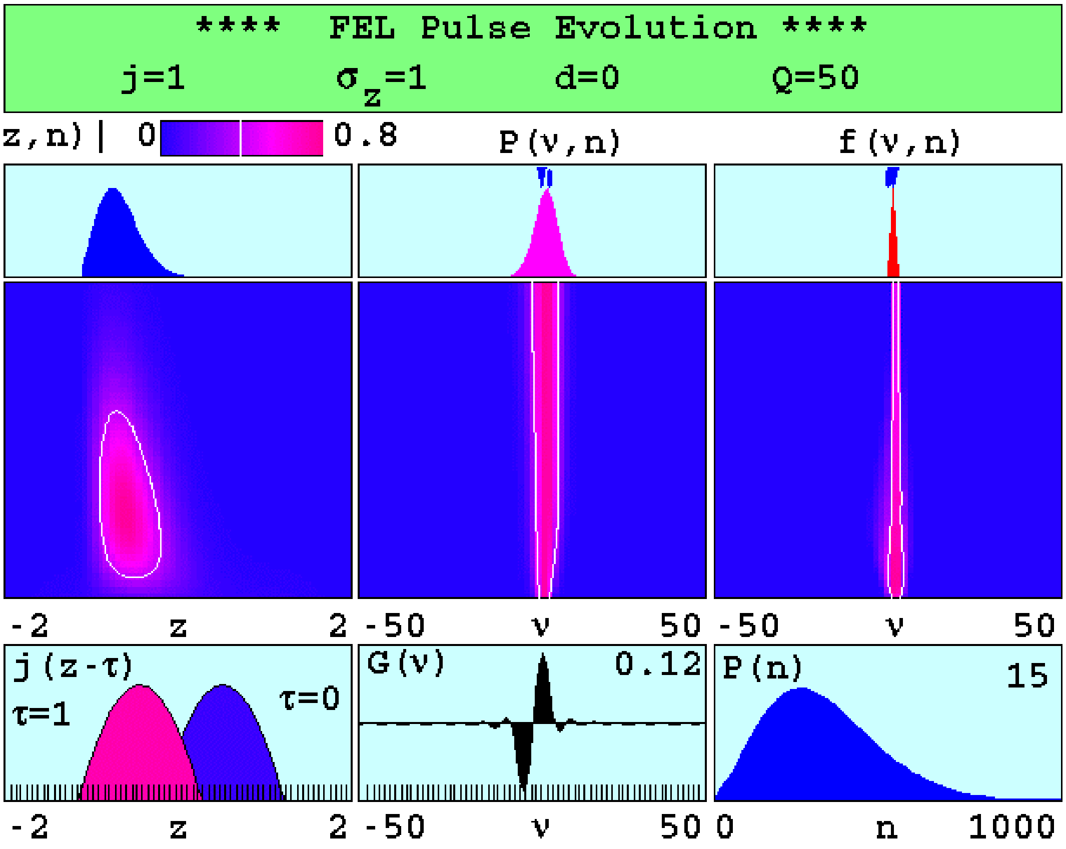

Figure 20. Longitudinal multimode simulation results for a short pulse FEL at exact synchronism $(d = 0)$ over $n = 1000$ passes. The optical pulse $|a(z,n)|$ drifts away from the electron pulse $j(z-\tau)$, and the optical power $P(n)$ decays.

Figure 21 shows a simulation with the same parameters, except now there is a small desynchronism $(d = 0.002)$, which means the cavity is slightly shortened to allow the optical pulse to "keep up" with the electron pulse. The optical power evolution $P(n)$ shows that the FEL now reaches steady-state saturation after about $n = 800$ passes. In steady-state, the gain each pass equals the loss each pass $(1/Q = 2\%)$. When the optical field saturates, the bunched electrons begin to execute synchrotron oscillations as they slip back over the optical field sites. This induces a slight modulation of the final optical pulse in the upper left, and the optical power spectrum $P(\nu, n)$ becomes broader.

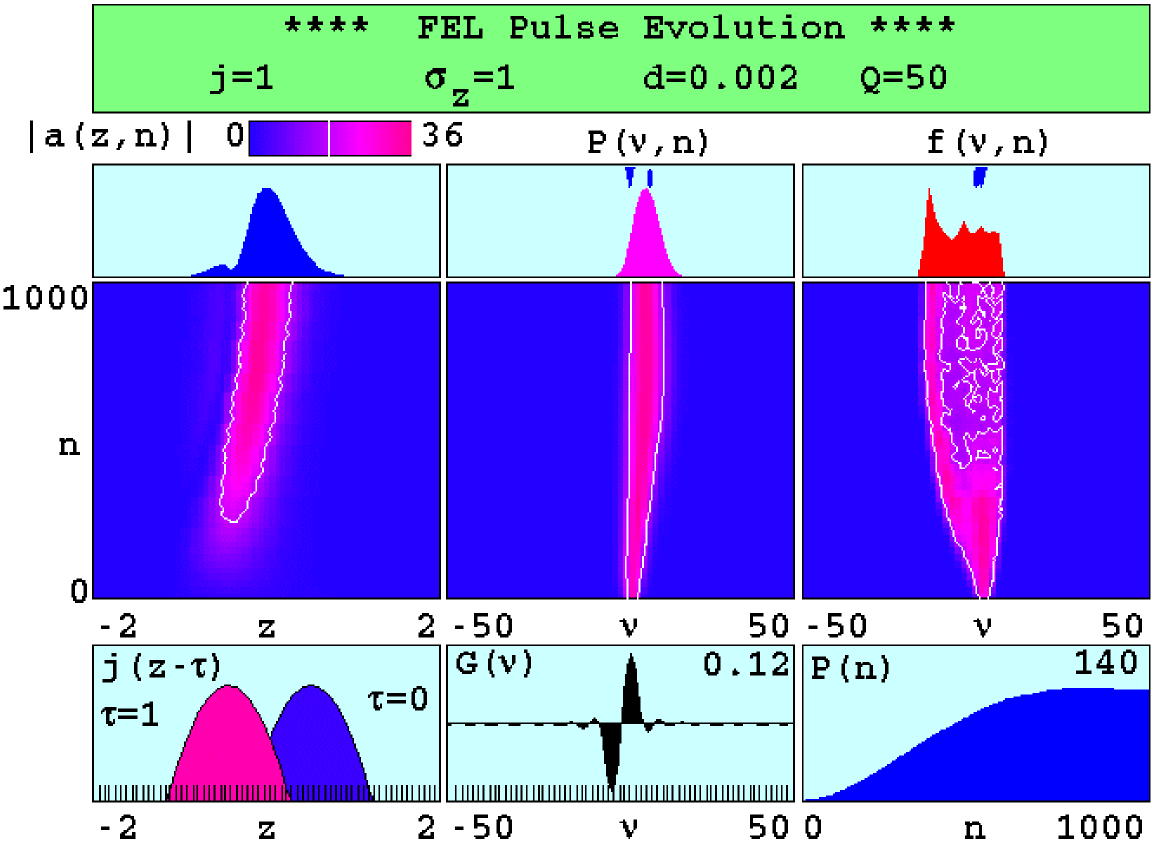

Figure 21. Longitudinal multimode simulation results for a short pulse FEL with small desynchronism $(d = 0.002)$, showing steady-state saturation of the optical power $P(n)$.

Figure 22 shows another simulation with large desynchronism $(d = 0.02)$. Now the optical pulse advances ahead of the electron pulse each pass, becoming very broad, as shown by the final optical pulse in the upper left. If the window was wide enough to contain the entire pulse, it would show that the pulse has a long exponential tail [1]. Less overlap between the electron and optical pulses yields less gain, and the steady-state power $P(n)$ is reduced. The steady-state optical power is reduced at large desynchronism, and for large enough *d*, the power is zero. This defines a range of desynchronism values where the FEL operates.

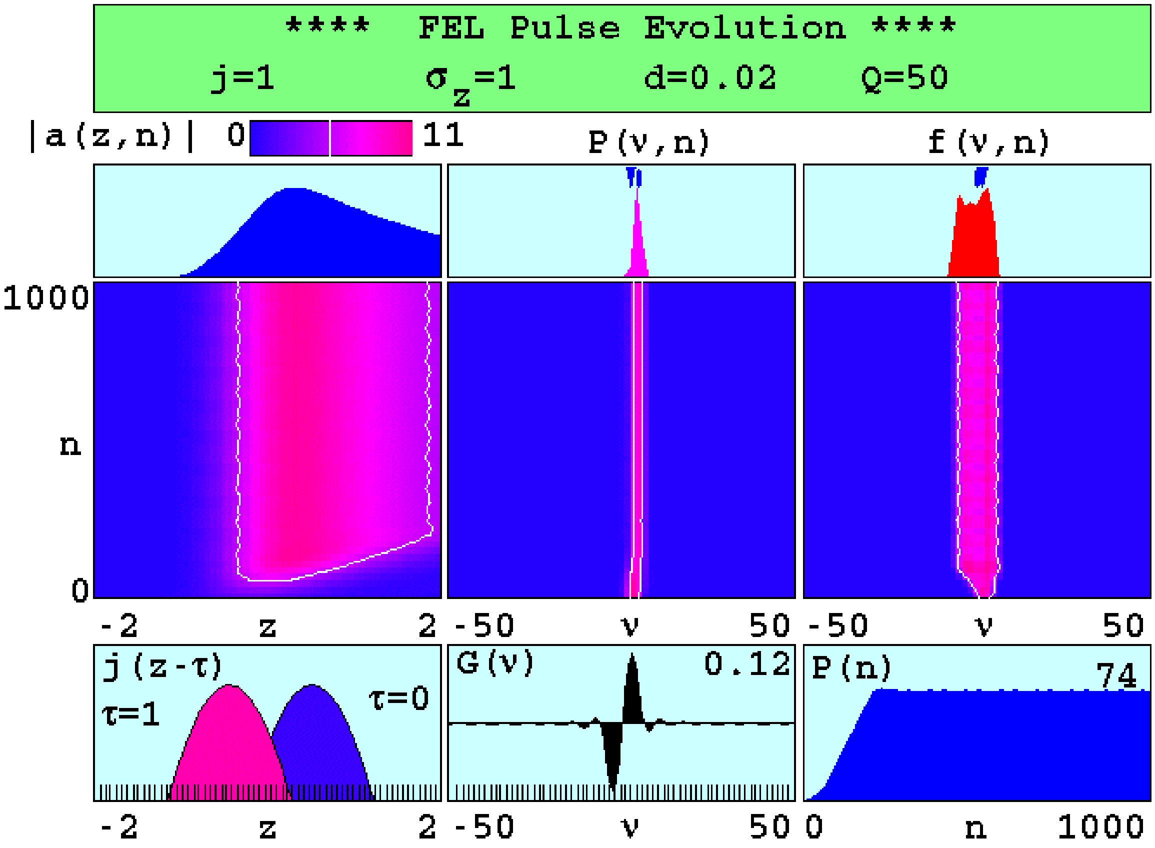

Figure 22. Longitudinal multimode simulation results for a short pulse FEL with large desynchronism, $(d = 0.02)$. The optical pulse $|a(z,n)|$ is now long, and the steady-state power $P(n)$ is reduced.

a. Limit Cycles: Stanford FIREFLY FEL

In strong optical fields, the trapped-particle instability can lead to modulations in the optical pulse. These can appear as sharp spikes that drift periodically across the pulse envelope at a rate depending on the desynchronism. This "limit-cycle" behavior has been observed in FEL experiments [35,36]. Figure 23 shows the output from a simulation of the Stanford FIREFLY [37], an FEL that was designed in 1994 to produce 1 kW average power at a wavelength of 7.6 µm. Limit cycles are clearly seen in the evolution of the optical field $|a(z,n)|$ and the total optical power $P(n)$. Sidebands appear in the optical power spectrum $P(\nu,n)$, and their separation roughly corresponds to the synchrotron frequency, $\nu_s = |a|^{1/2}$.

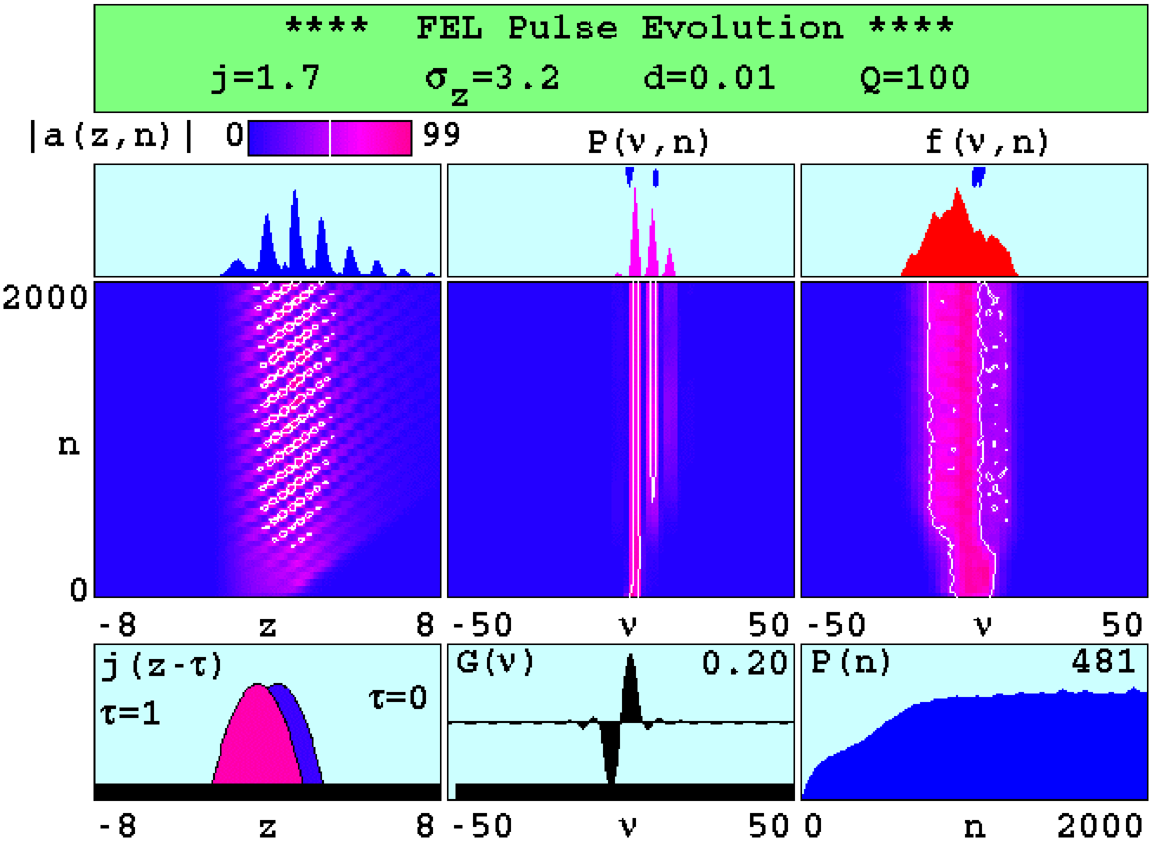

Figure 23. Longitudinal multimode simulation results for the Stanford FIREFLY experiment. The trapped-particle instability causes limit-cycle behavior in the optical pulse $|a(z,n)|$ and the formation of sidebands in the optical power spectrum $P(\nu,n)$. (From [37].)

b. Ultra-short Pulse FELs

In the mid-1990's we studied ultra-short pulse FEL oscillators, such as FELIX in the Netherlands [38], which uses picosecond electron pulses. This author played a key role in planning this research, developing and running the simulations, and interpreting their results, and was the lead author of a paper we published on the results of this work [39]. Figure 24 shows the results of a simulation of an ultra-short pulse FEL with $\sigma_z = 0.1$ and very small desynchronism $d = 0.0002$ over $n = 5000$ passes.

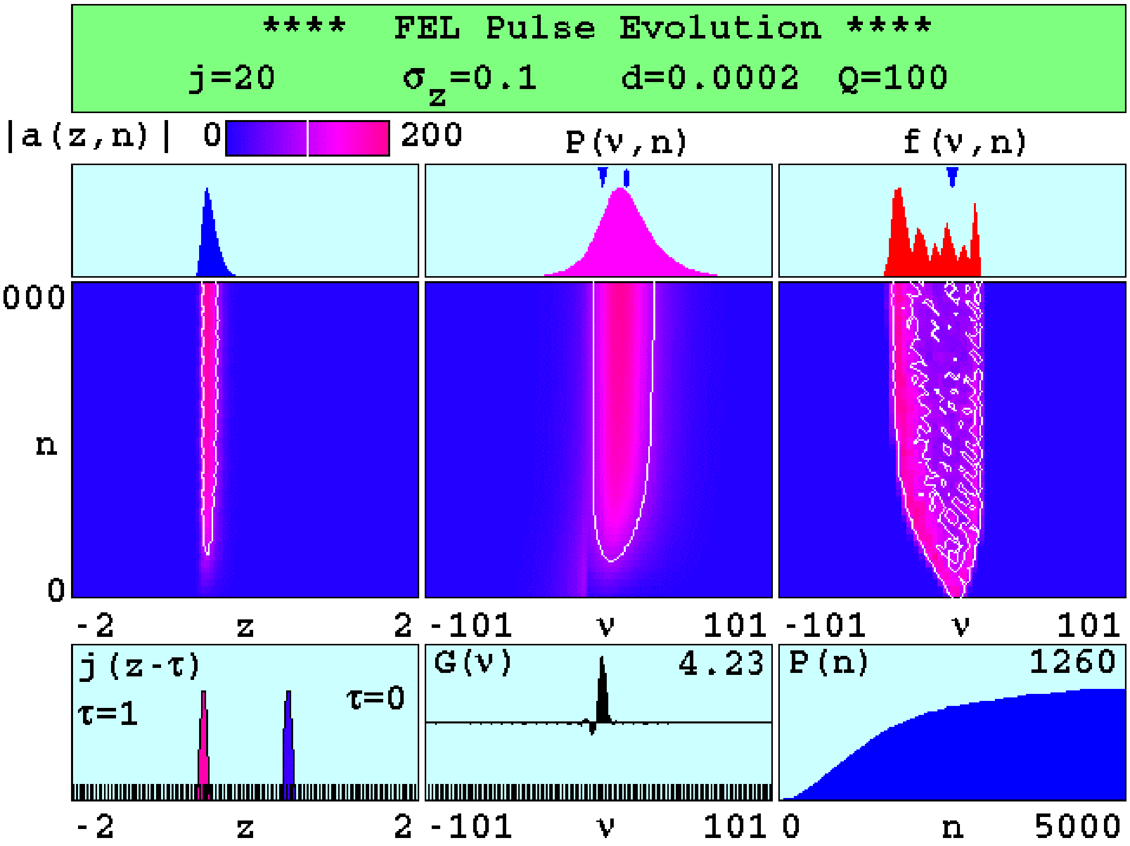

Figure 24. Longitudinal multimode simulation results for an ultra-short pulse FEL $(\sigma_z = 0.1)$, showing the formation of a narrow optical pulse $|a(z,n)|$ and a broad optical power spectrum $P(\nu,n)$. (From [39].)

In Figure 24, the final optical pulse $|a(z,n)|$ is about the same length as the electron pulse $j(z-\tau)$, and much shorter than the slippage distance. Since the optical pulse is so short, the electron pulse does not "see" much of the light until it is more than halfway down the undulator, leaving less time for bunching and gain. However, the large dimensionless current density $j = 20$ enables bunching and gain to develop quickly. The 1% loss each pass $(Q = 100)$ allows the optical field to grow to a large amplitude over $n = 5000$ passes.

c. Electron Beam Energy Modulation: Stanford SCA FEL

In 1990, the Stanford Superconducting Accelerator (SCA) FEL was used to study the effects of electron beam energy modulation [40], which is equivalent to oscillation of the electron phase velocity through the relationship $\Delta\nu = 4\pi N \Delta\gamma/\gamma$. Figure 25 shows the output from a simulation of the Stanford SCA FEL over $n = 2000$ passes, with a sinusoidal variation added to the electron phase velocity on each pass, $\nu(n) = \nu_0 + A_0 \sin(2\pi\, n/N_0)$. The amplitude of the phase velocity modulation is $A_0 = 2\pi$, and the period is $N_0 = 500$ passes. The energy modulations can be seen in the evolution of the electron phase velocity distribution $f(\nu,n)$, and the optical power spectrum $P(\nu,n)$. As strong optical fields develop, mode competition narrows the spectrum, making it more resistant to modulation. This prevents the peak optical power from following the sinusoidal modulations fully to the right, so we observe flattening of the $P(\nu,n)$ oscillations for $\nu > 0$. The total optical power $P(n)$ also oscillates at the same frequency; the dips in the peaks correspond to narrowing of the peaks in the optical pulse evolution, $|a(z,n)|$.

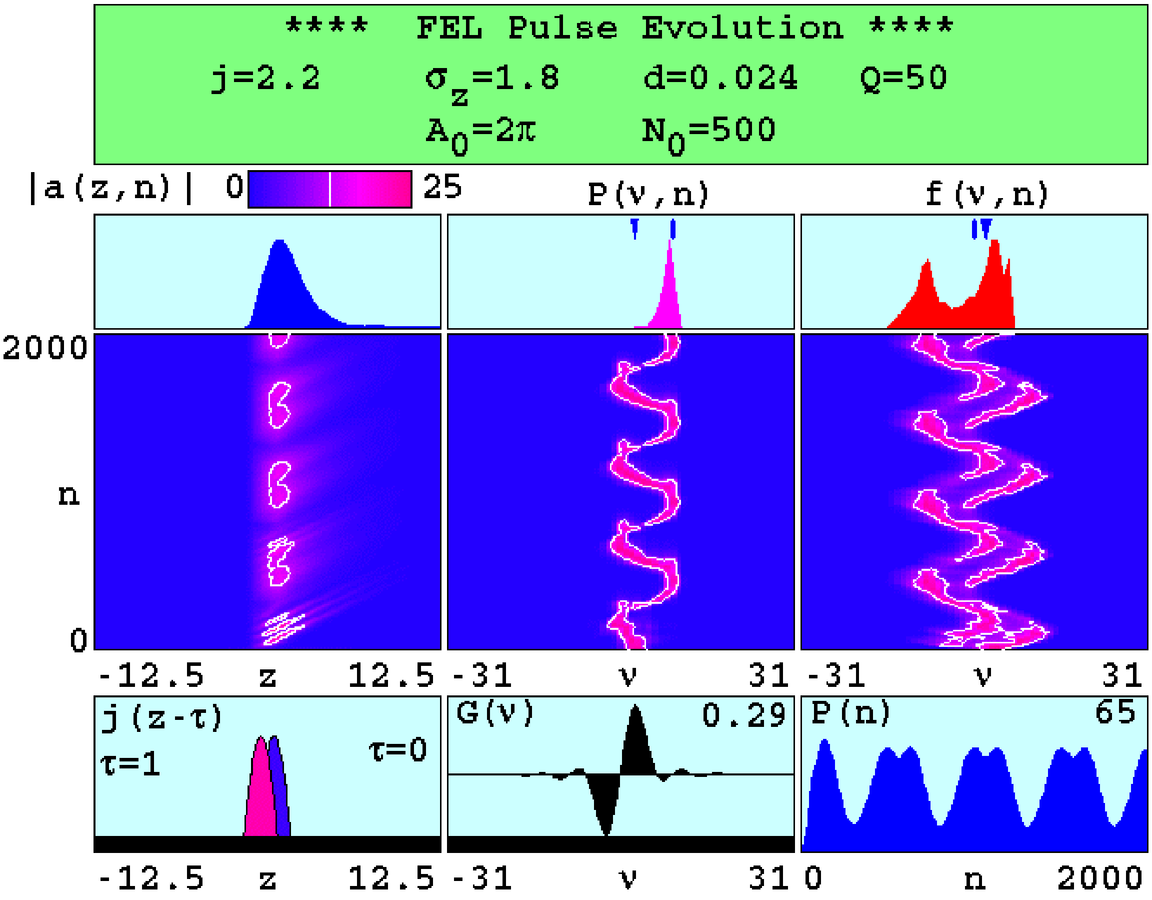

Figure 25. Longitudinal multimode simulation of the Stanford SCA FEL with modulated electron beam energy. Oscillations appear in the optical pulse $|a(z,n)|$, the power spectrum $P(\nu,n)$, the phase velocity distribution $f(\nu,n)$, and the optical power $P(n)$. (From [41].)

C. CURRENT NPS RESEARCH: TJNAF FEL

For the past several years, we have been involved in design studies for the Thomas Jefferson National Accelerator Facility (TJNAF) FEL in Virginia [7]. Their accelerator provides 0.5 ps duration electron pulses at 34.5 MeV energy with a peak current of 50 A, at a pulse repetition rate of 18.7 MHz. These values correspond to dimensionless current density $j=10$ and electron pulse length $\sigma_z=1$. Their undulator has $N=41$ periods of length $\lambda_0=2.7$ cm each, with undulator parameter $K=0.98$. The FEL produces up to 2 kW of average power at a wavelength of $\lambda=6$ μm inside a $Q=10$

resonator. It is currently being upgraded to 10 kW [8] by increasing the electron beam energy, the peak current, and the pulse repetition rate. A 100 kW FEL [42] is also in the design stage.

In the TJNAF FEL, after the electron beam exits the undulator, it is recirculated back to the accelerator for energy extraction. Recirculation enhances system efficiency, and reduces radiation shielding requirements for the beam dump, but it requires a small induced electron energy spread $\left(\lesssim 10\%\right)$ for beam transport. A high power FEL can induce a significant electron energy spread. Various undulator designs have been considered to optimize steady-state optical power while minimizing the exhaust energy spread of the electron beam.

1. Positive and Negative Undulator Tapers

Last year we published a paper on positive and negative undulator tapers [27], which were explored experimentally using the TJNAF FEL [43]. We simulated linear taper rates of $\Delta K/K = \pm 5\%$, $\pm 7.5\%$, and $\pm 10\%$, corresponding to phase accelerations of $\delta = \pm 4\pi$, $\pm 6\pi$, and $\pm 8\pi$ in the pendulum equation (46). For each value of the undulator taper rate, we varied the desynchronism from d = 0 to 0.4 to determine the optimum weak-field gain and steady-state power. For most of the range of d, a positive taper provides no advantage over the untapered case. However, for a small negative taper $\delta = -4\pi$, our simulations predict more steady-state power than the untapered case up to $d \simeq 0.18$. Negative taper also induces slightly less energy spread on the electron beam.

For some values of $d < 0.1$, we observe limit-cycle behavior. Figure 26 shows the results of a *pulsevn* simulation of the TJNAF FEL over $n = 2000$ passes, with a large positive taper $\delta = 8\pi$, and desynchronism $d = 0.026$. To include shot noise, the electron phases are given an initial random spread of amplitude $\delta\zeta = 0.0001$. In the evolution of the optical power spectrum $P(\nu, n)$, at about $n = 200$ passes, the FEL suddenly shifts to a different frequency. This corresponds to the onset of strong optical fields, where the peak in the gain curve shifts to a larger value of ν (refer to Figure 16(a)). After that, limit cycles appear as oscillations of the optical field $\left|a(z,n)\right|$, the optical spectrum

$P(\nu,n)$, and the electron phase velocity distribution $f(\nu,n)$. The total optical power $P(n)$ is modulated by about 50%, at the same frequency. This limit-cycle behavior is also seen with negative tapers.

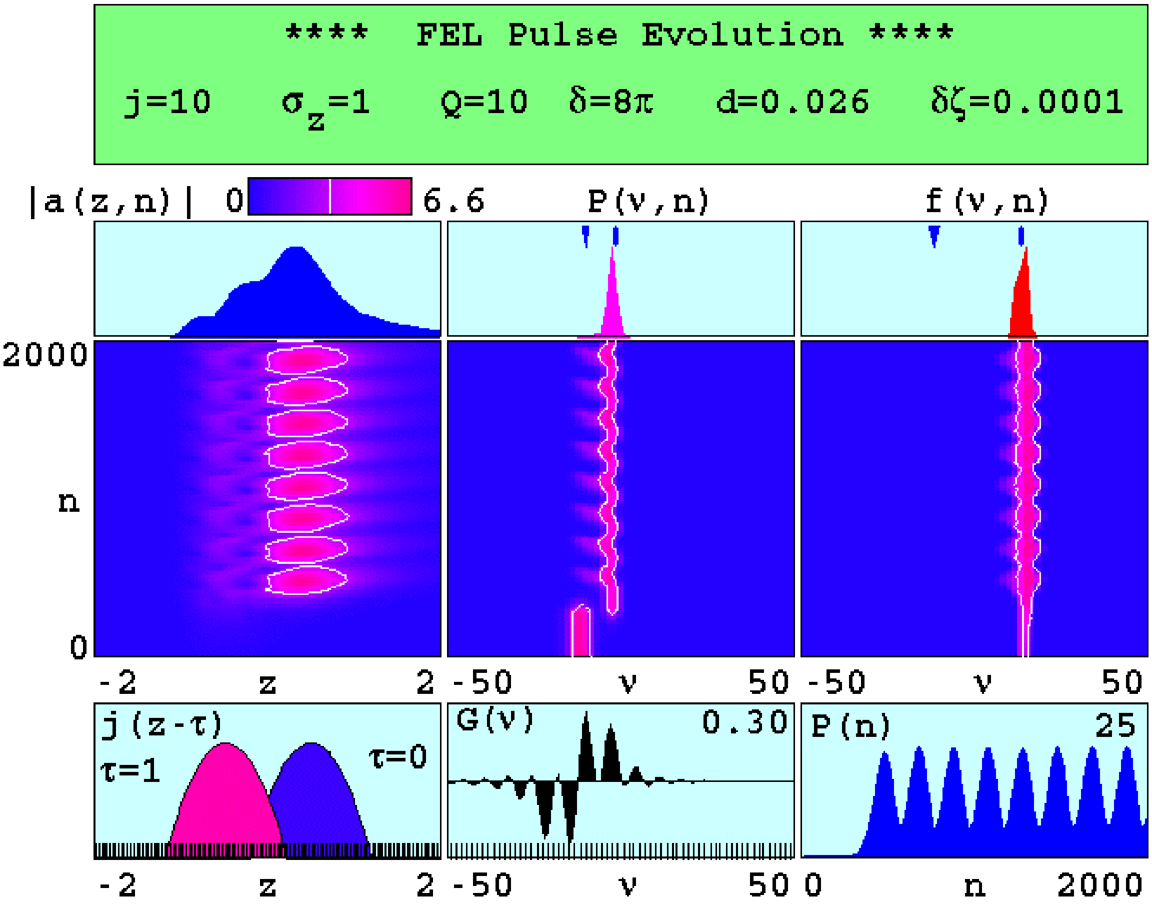

Figure 26. Longitudinal multimode simulation results for the TJNAF FEL with large positive taper, $\delta = 8\pi$. Limit-cycle behavior is observed in the evolution of the optical pulse $|a(z,n)|$ and the optical power spectrum $P(\nu,n)$. The total optical power $P(n)$ is modulated by ~50%. (From [27].)

2. Step-tapered Undulator

Last year we studied the use of a step-tapered undulator for the proposed 100 kW TJNAF FEL. This author played a key role in developing and running the simulations and interpreting the results, and was the lead author of a paper on this work, recently accepted for publication [44]. Unlike the linear tapered undulators discussed previously, the step-tapered undulator would have an abrupt change in the magnetic field halfway through the undulator. In an experiment, this would be done by having two separate undulator segments, each with a different gap between the magnets. The modification to the pendulum equation is similar to the linear taper (46):

$$\frac{d^2\zeta}{d\tau^2} = \theta\left(\tau - \frac{1}{2}\right)\Delta + a\cos(\zeta + \phi) \qquad (50)$$

where $\theta(z) = \begin{cases} 0 \text{ for } z < 0 \\ 1 \text{ for } z \geq 0 \end{cases}$ is the step function, and

$$\Delta = -\left(\frac{4\pi NK^2}{1+K^2}\right)\left(\frac{\Delta K}{K}\right) \qquad (51)$$

is the phase acceleration at $\tau = 1/2$ due to the step taper $\Delta K/K$.

Figure 27 shows the results of a series of longitudinal multimode simulations of the proposed 100 kW FEL for a negative step taper $\Delta = -\pi$, with the desynchronism varied from $d = 0$ to 0.3.

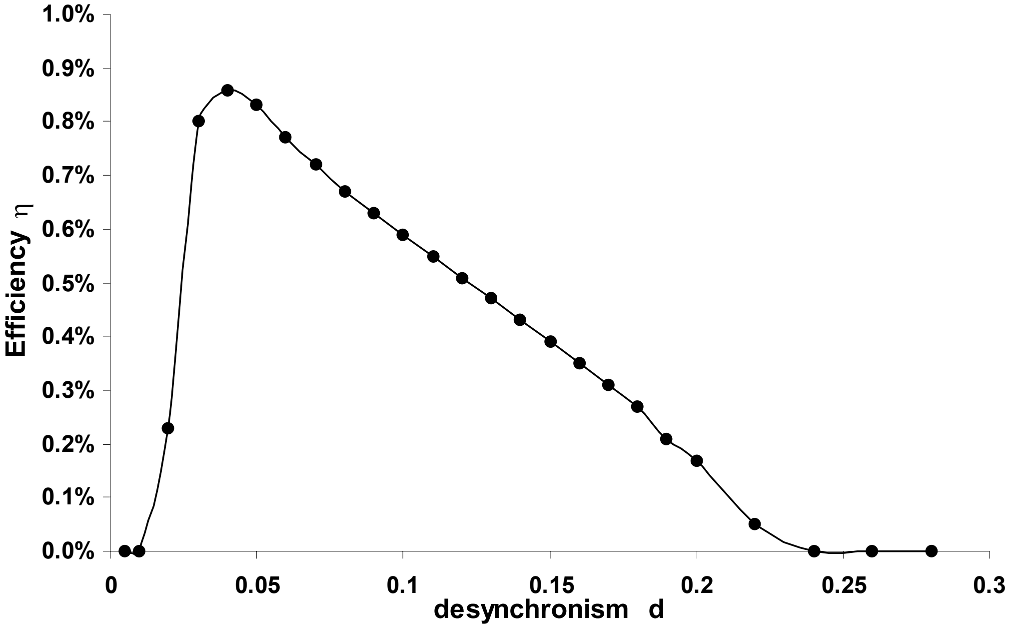

Figure 27. Extraction efficiency η versus desynchronism d for the TJNAF 100 kW FEL with negative step-tapered undulator, $\Delta = -\pi$. To produce 100 kW, an efficiency of $\eta > 0.7\%$ is required, which is achieved for $0.03 \lesssim \mathrm{d} \lesssim 0.07$.

In Figure 27, the extraction efficiency $\eta = \Delta\gamma/\gamma = \overline{\Delta\nu}/4\pi N$ is determined from the shift in the average electron phase velocity, $\overline{\Delta\nu}$. Note that η is just the single-pass extraction efficiency; the overall system "wall plug" efficiency is enhanced by recirculation of the electron beam. The steady-state output power is directly proportional to η . Figure 27 shows the general features of desynchronism (or "cavity detuning") curves that are commonly observed in our simulations as well as in FEL experiments [43]. At exact synchronism, $d = 0$, there is no output power, as discussed previously. At small desynchronism, $d \approx 0.01$, there is a sharp rise in the output power, peaking at $d \approx 0.05$ in this case. Limit-cycle behavior is often seen in this region, as shown in earlier figures. As d is further increased, the power slowly drops off, until eventually there is no output power, for $d \geq 0.24$ in this case. For stable operation, it may be desirable to operate the FEL at a value of d slightly beyond the peak of the desynchronism curve. Otherwise, small fluctuations in the cavity length could cause large fluctuations in the output power, unless active feedback is employed to keep the cavity length constant.

To achieve the goal of 100 kW average power, an efficiency of $\eta \geq 0.7\%$ is required for this FEL. Figure 27 shows that with a step-tapered undulator $\Delta = -\pi$, the 100 kW goal is reached for desynchronism values $0.03 \lesssim d \lesssim 0.07$. For no taper, the peak output power is slightly reduced, and the range of desynchronism values that produce the 100 kW goal is narrower, $0.03 \lesssim d \lesssim 0.06$. The induced electron energy spread is similar in both cases, $\Delta\gamma/\gamma \approx 4\%$, well below the requirement for recirculation. Other values of step-taper that we studied, $\Delta = \pi$, $\pm 2\pi$, did not reach the 100 kW goal.

Previously published results based on simulations and experimental results from CLIO and FELIX showed as much as a 75% efficiency enhancement with a negative step-tapered undulator [45-47]. In contrast, we found only a slight improvement in efficiency with a small negative taper for the parameters investigated. The results of our research show that step-taper cannot always be as effective as found earlier, and that an FEL must be far into strong-field saturation before tapering can extend the saturation limit.

3. FEL Klystron

Last year we published a paper in which we investigated the use of an FEL klystron configuration for the TJNAF 10 kW FEL [48]. This FEL will use an electromagnetic undulator, so by changing the magnetic field strength, the undulator parameter can be varied from $K = 1$ to 4. Thus according to the resonance condition (14), the FEL wavelength can be tuned from 2.3 μm to 20 μm. Since the undulator consists of two separate sections, it is possible to have a dispersive section in between. This would enhance the gain in weak fields, but reduce the saturation power and hence the efficiency. Our simulations showed that with no klystron $(D = 0)$ and undulator parameter $K = 1$ or 2, the TJNAF FEL could produce a maximum of 14.5 kW average power. With $K = 3$ or 4, the weak-field gain is below threshold, and there is no output power, due mainly to a smaller filling factor F at long wavelengths. Introducing a weak klystron, $D = 0.25$, reduces the average power to slightly above 10 kW for $K = 1$ or 2, but provides enough gain to enable operation with K = 3 at an output power of 7.5 kW. With a stronger klystron, $D \geq 0.5$, all four undulator parameters produce some output power, but less than the desired value of 10 kW.

V. TRANSVERSE MULTIMODE SIMULATIONS

The simulations described so far have all assumed plane waves, but in an actual FEL experiment, an optical wavefront with finite transverse dimensions will have multiple transverse modes. To study these transverse modes, we have developed several three-dimensional simulations that include diffraction and self-consistent evolution of the optical wavefront in x, y, and τ . These simulations do not assume axial symmetry; the electron beam is allowed to have separate emittance in the x and y directions. Transverse distances are normalized to the characteristic optical mode radius $W_0 = \sqrt{L\lambda/\pi}$. The parabolic wave equation (36) is used to follow the evolution of the optical field.

A. SINGLE PASS

For simulating FEL amplifiers, we have a three-dimensional simulation called *3d1* that follows multiple transverse optical modes over a single pass through the undulator. The output of *3d1* shows the evolution of the optical wavefront and the driving current, the electron phase velocity distribution, the optical power and gain, and the optical phase versus dimensionless time τ.

1. Optical Guiding

As mentioned earlier, the FEL interaction can distort the optical mode. If the current density is very large, $j \gg 10^3$, a phenomenon known as "optical guiding" can contain the light in the vicinity of the electron beam. Enhanced overlap between the electron beam and the optical mode increases the FEL gain. There are two processes that contribute to optical guiding. A narrow, high-current electron beam can continuously amplify the central portion of the wavefront, effectively narrowing the optical mode area in a process known as "gain guiding". A high-current beam can also continuously drive the optical phase, opposing the phase shift due to natural diffraction and focusing the light back towards the electron beam in a process known as "phase guiding". In the following example, both types of optical guiding are observed.

a. Boeing APLE Amplifier

Figure 28 shows the results from a simulation of the Boeing APLE amplifier, discussed earlier. The box in the upper right shows the dimensionless parameters for this experiment. The current density is $j = 2\times10^5$, with an electron beam radius of $\sigma_e = 0.09$. The electrons have a Gaussian energy spread of width $\sigma_G = 6$ and an exponential angular spread of width $\sigma_\theta = 7$. The initial electron phase velocity $\nu_0 = 15$ is determined from FEL gain surfaces for these parameters. The initial optical field amplitude is $a_0 = 18$. The position of the optical waist is at the beginning of the undulator, $\tau_w = 0$, in an FEL amplifier with no resonator mirrors. The dimensionless Rayleigh length, $z_0 = w_0^2 = 0.8$, is determined by the optical mode radius, w_0. The undulator has $N = 256$ periods, with a 20% positive taper rate corresponding to a phase acceleration of $\delta = 200\pi$. The color scale shown in the parameter window is used for the intensity plots of the optical field amplitude and the electron beam current density, with dark blue corresponding to an amplitude or density of zero, and light blue corresponding to the maximum amplitude or density. The white contour line on the intensity plots corresponds to half of the maximum value, as indicated on the color scale.

The intensity/contour plot in the upper-left of Figure 28 shows a slice through the optical wavefront, $\left|a\left(x,\tau\right)\right|$ at $y = 0$, as it evolves in time, and next to it is the final wavefront $\left|a\left(x,y\right)\right|$. The narrow, high-current electron beam causes optical guiding, which yields a much smaller final spot size than would be predicted from natural diffraction. The slow evolution of the optical phase in the center of the wavefront, $\phi\left(0,\tau\right)$ in the center-right, indicates that the predominant process in this case is gain guiding. In the center-left is shown the evolution of the driving current $\sigma\left(x,\tau\right) = j\left\langle\cos\left(\zeta+\phi\right)\right\rangle$ at $y = 0$, where j is the dimensionless current density at the site $\left(x,y\right)$ and $\left\langle\cdots\right\rangle$ indicates an average over all the electron phases at that site.

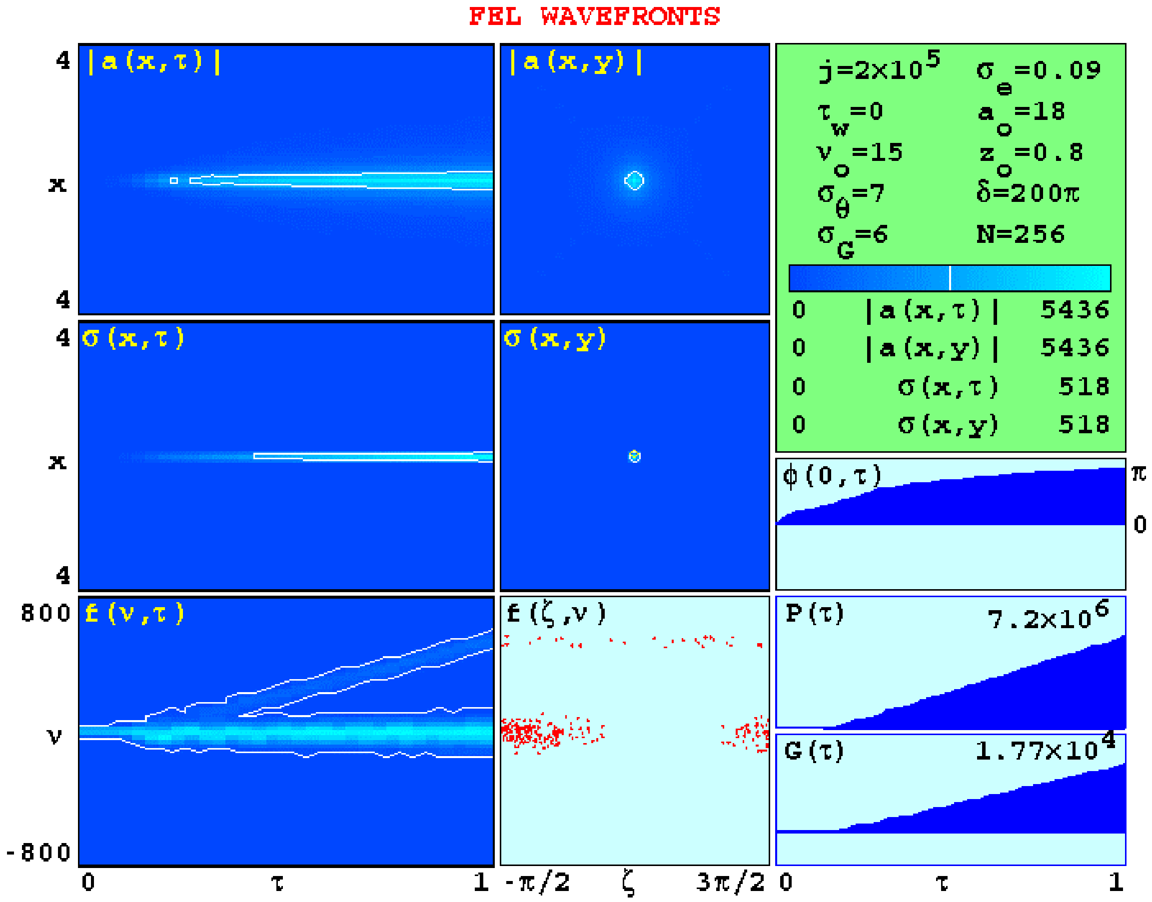

Figure 28. Three-dimensional simulation results for the Boeing APLE amplifier. The various plots are described in the text. The evolution of the optical wavefront $|a(x,\tau)|$ shows optical guiding. (From [33].)

The final electron beam profile $\sigma(x,y)$ in the center of Figure 28 and the final wavefront $|a(x,y)|$ above it are used to estimate the filling factor, $F = r_e^2/W_0^2 \approx 0.1$, where r_e is the electron beam radius and W_0 is the mean optical mode radius. In the lower-left is the evolution of the electron spectrum $f(\nu,\tau)$, showing the 20% taper starting at the saturation time $\tau_{\text{sat}} \approx 0.2$. The final phase-space plot $f(\zeta,\nu)$ in the lower-center shows that about 70% of the electrons remained trapped in closed orbits. The graphs in the lower-right show that the optical power $P(\tau)$ and gain $G(\tau)$ continue to grow linearly after τ_{sat}, so the taper is effectively increasing the efficiency. This simulation predicts an efficiency of $\eta = 8\%$, which is too optimistic since pulse slippage effects are neglected.

B. MULTIPLE PASSES

For simulating transverse optical modes in FEL oscillators, we have another three-dimensional simulation called *3dn* that runs for many passes, including the effects of mirror transmission and edge losses. The shape and size of the cavity mirrors is determined by the Rayleigh length, the optical mode waist, and the mirror edge losses. The mirror transmission can be varied, as well as the output coupling mechanism. The output of *3dn* shows the evolution of the optical wavefront over many passes, the final optical mode shape, the electron phase velocity distribution, the optical power and gain versus pass number *n*.

1. Optical Mode Distortion

In a typical FEL oscillator, the steady-state optical mode has a transverse Gaussian profile, determined mainly by the resonator geometry (the size, shape and location of the mirrors, and the outcoupling mechanism). However, a moderate electron beam current, $j \approx 100$ to 1000, can distort the optical mode, affecting the average filling factor and hence the weak-field gain and steady-state power.

a. SELENE FEL Klystron Oscillator

The SELENE experiment, mentioned previously, is a two-stage FEL proposed in 1993 for satellite power-beaming applications [49], based on the Novosibirsk racetrack microtron [50]. The three-stage FEL klystron oscillator consists of three identical undulators separated by two dispersive magnets located at dimensionless times $\tau = 1/3$ and $\tau = 2/3$. The klystron design was intended to enhance electron bunching and reduce the saturated optical power inside the cavity. The purpose of the oscillator is only to bunch the electrons before they are injected into an external radiator [25]. The radiator creates high average power over a single pass by self-amplification of spontaneous emission from the bunched electron beam.

Figure 29 shows the output from a *3dn* simulation of the SELENE oscillator. The dimensionless parameters for this experiment are shown in the upper-right. All longitudinal distances are normalized to the undulator length *L*, and transverse distances are normalized to the characteristic optical mode radius $W_0 = \sqrt{L\lambda/\pi}$. The microtron provides an electron beam with current density $j = 2500$ and radius $\sigma_e = 0.14$. The electron beam can be given an offset from the undulator axis, but in this case there is no offset, so $x_0 = 0$. At each pass, the electrons are injected with an initial Gaussian spread in phase velocity of width $\sigma_G = 3$, centered on $\nu_0 = 1$. The simulation is started with a weak optical field, $a_0 = 1$, but the optical power quickly saturates after $n = 10$ passes. The Rayleigh length $z_0 = 0.4$ and the position of the optical waist $\tau_w = 0.5$ are chosen to maximize the overlap between the electron beam and the optical mode. The klystron dispersive strength is given by $D = 0.66$. The three undulator sections have a total of $N = 120$ periods. The mirror radius is $r_m = 1.9$, and radius of curvature $r_c = 1.2$. Cavity losses are given by $Q = 10$ corresponding to approximately 10% mirror transmission and edge losses around the mirrors of 10% per pass.

In the upper left of Figure 29, we show a slice through the optical wavefront, $|a(x,n)|$ at $y = 0$, as it evolves over $n = 10$ passes, and next to it the final optical wavefront $|a(x,y)|$. Below that is a slice through the optical wavefront, $|a(x,\tau)|$ at $y = 0$, as it evolves over the final pass, with the mirrors shown at each end, and tick marks beneath indicating the beginning of the undulator $(\tau = 0)$ and the end of the undulator $(\tau = 1)$. The mirror separation is artificially shortened to twice the undulator length for numerical convenience.

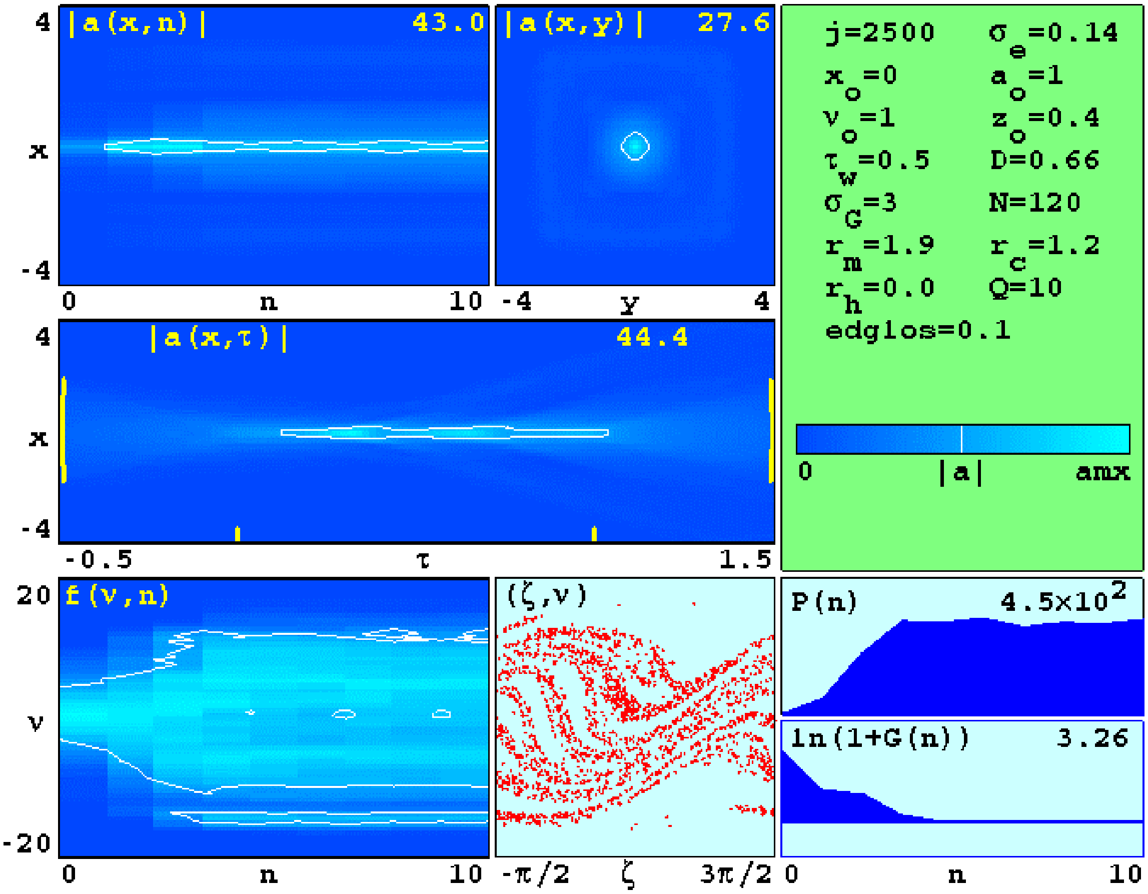

Figure 29. Three-dimensional simulation results for the SELENE FEL oscillator, showing mode distortion in the evolution of the optical wavefront $|a(x,n)|$. (From [51].)

Figure 29 shows optical mode distortion, and the effect of the klystron magnets is clearly seen in the final mode shape, $|a(x,\tau)|$. In the lower-left is the evolution of the electron spectrum $f(\nu,\tau)$. The final electron phase-space plot in the lower-center shows evidence of bunching. The achromatic bending magnet used to extract the electrons from the oscillator [52] would add more dispersion and further improve the bunching. In the lower right is the evolution of the optical power $P(n)$ and the gain $G(n)$, showing that the oscillator quickly saturates. It may be necessary to operate the resonator at a low $Q \lesssim 10$ to prevent the power from growing excessively and damaging the mirrors.

b. *TJNAF 10 kW FEL*

Figure 30 shows a three-dimensional simulation of the TJNAF 10 kW FEL oscillator over $n = 500$ passes. The dimensionless parameters for this experiment are shown in the upper-right. Their accelerator provides an electron beam with a current density of $j = 165$ and a radius of $\sigma_e = 0.12$. At each pass, the electrons are injected with an initial Gaussian spread in phase velocity of width $\sigma_G = 0.5$, centered on $\nu_0 = 9$. The Rayleigh length is $z_0 = 0.4$ with the optical waist located in the center of the undulator, $\tau_w = 0.5$. The undulator has $N = 24$ periods. The dimensionless mirror radius is $r_m = 3.2$, and the dimensionless radius of curvature is $r_c = 1.2$. Cavity losses are given by $Q = 6$ corresponding to approximately 15% mirror transmission and edge losses around the mirrors of 0.1% per pass. The simulation was started with a weak optical field, $a_0 = 0.1$, and allowed to develop until steady-state power was obtained in a stable resonator mode.

In weak fields, $a \lesssim \pi$, the narrow electron beam distorts the resonator mode, as seen in the upper-left plot $\left|a\left(x,n\right)\right|$ in Figure 30. Mode distortion reduces the filling factor, enhancing the gain in this example by about a factor of 4 compared to a simple theoretical estimate. As the optical power grows and reaches saturation, the figure shows that gain and mode distortion are reduced. Notice that at about $n = 200$ passes, the optical mode narrows and the power grows rapidly again, finally developing a more symmetric Gaussian mode with steady power. The plot of $\left|a\left(x,\tau\right)\right|$ in the center shows the steady-state optical mode.

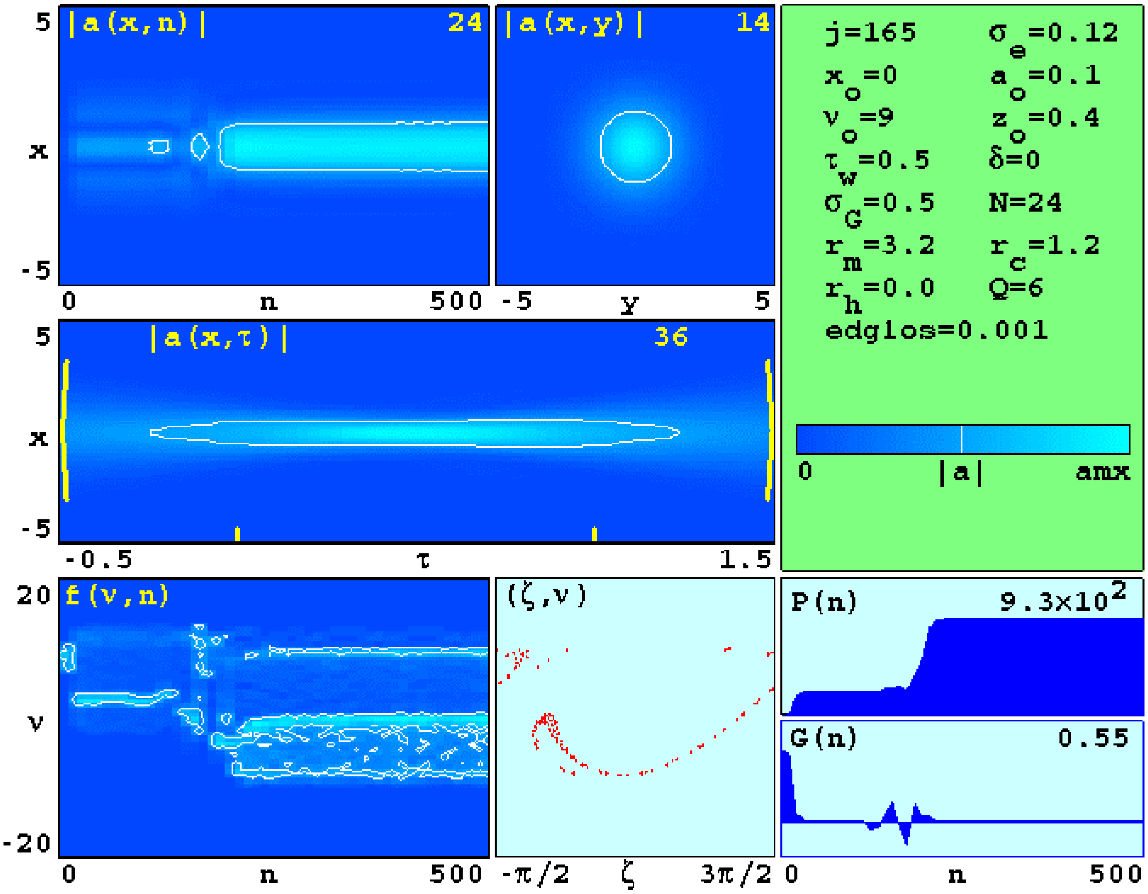

Figure 30. Three-dimensional simulation results for the TJNAF 10 kW FEL, showing optical mode distortion in weak fields, and the development of a Gaussian mode at saturation. (From [48].)

2. Current NPS Research: Short Rayleigh Length FELs

In the previous two examples, a Rayleigh length of $z_0 = 0.4$ was chosen to maximize the overlap between the electron beam and the optical mode. In a high average power FEL, it may be desirable to operate at a shorter Rayleigh length. This would result in a smaller mode waist, but a larger spot size at the mirrors, reducing the power density on the mirrors. Traditional FEL theory implies that a shorter Rayleigh length would reduce the average filling factor, and hence the gain and steady-state power, but mode distortion can counteract this effect. We have used our three-dimensional simulations to study short Rayleigh length operation for the proposed 10 kW and 100 kW upgrades for the TJNAF FEL at Jefferson Labs.

a. TJNAF 10 kW FEL

Figure 31 shows the result of a series of *3dn* simulations of the TJNAF 10 kW FEL. The weak-field gain and steady-state power are plotted versus the normalized Rayleigh length z_0. The design value of $z_0 = 0.4$ is indicated by the triangular tick mark at the bottom of the graph. The weak-field gain remains almost constant as the Rayleigh length is reduced from $z_0 = 0.6$ to 0.1. The gain is well above threshold $(1/Q \approx 15\%)$ for the entire range of z_0 values that we studied, indicating that it may be possible to operate at an even shorter Rayleigh length. As the Rayleigh length is reduced from the design value of $z_0 = 0.4$ to 0.1, the steady-state power increases by 50%. Also as the Rayleigh length is reduced, the optimum electron phase velocity ν_0, indicated at each point, increases.

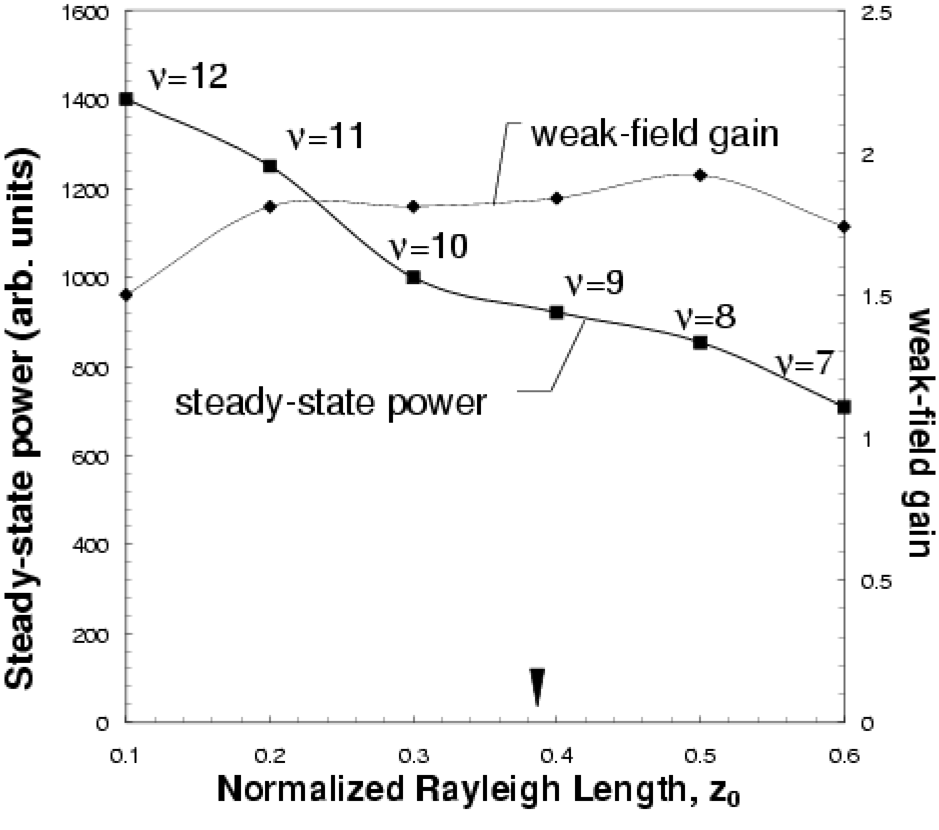

Figure 31. Three-dimensional simulation results for the TJNAF 10 kW FEL, showing weak-field gain and steady-state power versus Rayleigh length. As the Rayleigh length is reduced, the weak-field gain stays fairly constant, and the steady-state power increases. (From [48].)

b. TJNAF 100 kW FEL

The design for the proposed 100 kW FEL assumes a resonator quality factor $Q = 4.2$ corresponding to approximately 21% mirror transmission, and edge losses around the mirrors of 1% per pass. Even with such large losses, the intra-cavity power may be too much for the mirrors to tolerate. Last year we reported the results of simulations using a short Rayleigh length resonator to reduce the power the density on the mirrors [53].

Figure 32 shows the shape of the optical mode and the power density on the mirrors for Rayleigh length $z_0 = 0.1$ to 0.5. The horizontal axis corresponds to the longitudinal axis of the resonator, normalized to the undulator length *L*. The resonator length is $11L$ with the mirrors located at $\tau = -5$ and +6, and the undulator is located between $\tau = 0$ and 1. The vertical axis is the optical mode radius in millimeters.

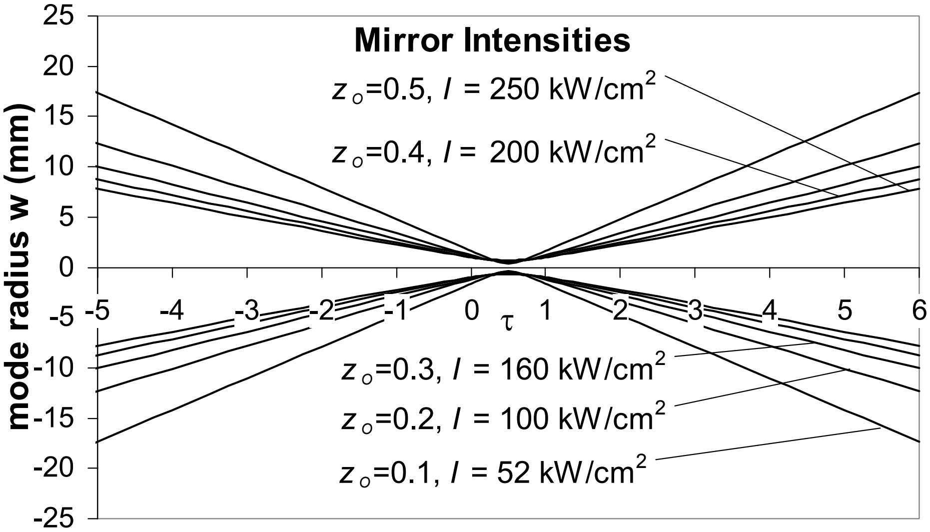

Figure 32. Optical mode radius versus dimensionless longitudinal position τ for an optical cavity with mirrors located at $\tau = -5$ and +6, for various Rayleigh lengths. As the Rayleigh length is reduced, the mode radius at the mirror increases, and the intensity decreases.

Figure 32 shows that a Rayleigh length of $z_0 = 0.3$ gives a spot size at the mirrors of 1 cm, corresponding to a power density of 160 $\mathrm{kW/cm^2}$. Reducing the Rayleigh length from $z_0 = 0.3$ to 0.1 increases the mirror spot size to approximately 1.7 cm and decreases the power density on the mirrors by a factor of 3.

A short Rayleigh length FEL requires a short undulator, to avoid beam scraping at the ends of the undulator. Also, since the mode waist is small in this case, a narrow electron beam is desirable. Figure 33 shows the results of a three-dimensional simulation of the proposed 100 kW FEL, with a short Rayleigh length given by $z_0 = 0.1$, and a narrow electron beam radius given by $\sigma_{x,y} = 0.1$ in the *x* and *y* directions. In this case we have used a newer simulation called *3dbetan* that includes the betatron motion of the electrons. The betatron oscillation frequency is $\omega_\beta = 1$ over the undulator length, with the electron beam focused in the middle of the undulator at $\tau_\beta = 0.5$. The beam's angular spread $\sigma_{\theta x,y} = 0.01$ is determined by the matching requirement $\sigma_{\theta x,y} = \omega_\beta^2 \sigma_{x,y}^2$. The large initial electron phase velocity $\nu_0 = 16$ optimizes the extraction efficiency for the short Rayleigh length FEL. The dimensionless mirror radius $r_m = 7.2$ is chosen to allow 1% edge losses per pass $(e = 0.01)$, and the dimensionless radius of curvature $r_c = 1.5$ determines the Rayleigh length.

In the upper-left of Figure 33, a slice through the optical wavefront $|a(x,n)|$ is shown as it evolves over $n = 200$ passes. After about 50 passes, the optical field begins to oscillate between two different modes with a period of about 10 passes. The optical power $P(n)$ and gain $G(n)$ in the lower right appear to oscillate at about the same frequency, as well as the electron phase velocity distribution $f(\nu, n)$ in the lower-left. The final wavefront $|a(x,y)|$ in the upper-center is donut shaped; if we ran the simulation for a few more passes, we would observe a different mode shape. The center plot, $|a(x,\tau)|$, presents a section through the optical wavefront during the final pass. The superimposed red dots show the sample electrons as they pass through the undulator from

$\tau = 0$ to 1. The white contour line shows where the field amplitude drops to 5% of its maximum value, as indicated on the color scale to the right. The complicated pattern of the contour line confirms the presence of multiple transverse modes. The optical wave amplitude profile, shown in yellow at the mirrors on each end, indicates that power is distributed across the mirrors.

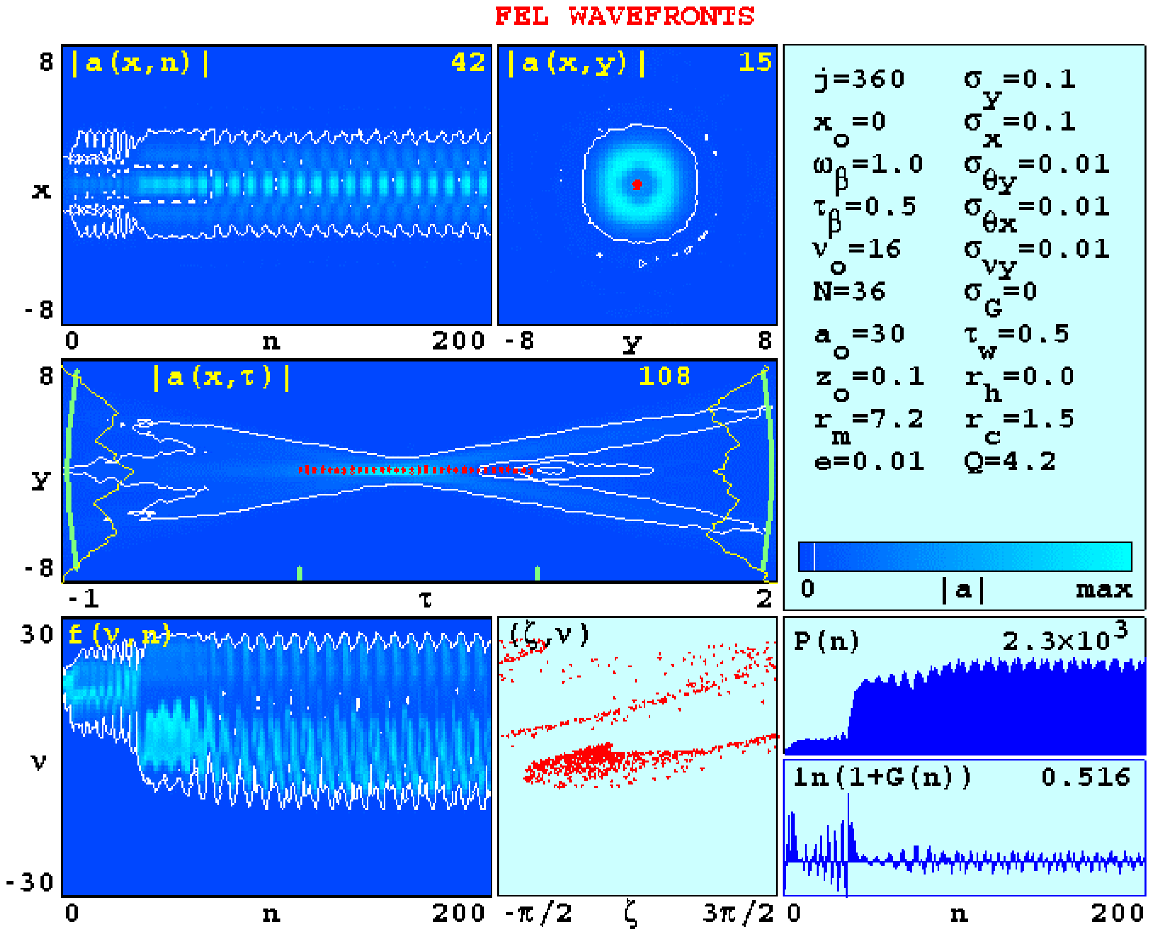

Figure 33. Three-dimensional simulation results for the proposed 100 kW TJNAF FEL with a short Rayleigh length, $z_0 = 0.1$, and a narrow electron beam, $\sigma_{x,y} = 0.1$, showing optical mode distortion and limit-cycle behavior.

With a larger electron beam radius, multimodes are suppressed. Figure 34 shows the results of another *3dbetan* simulation of the same FEL, with a longer Rayleigh length given by $z_0 = 0.5$ and a larger electron beam radius given by $\sigma_{x,y} = 0.5$. The dimensionless current density has been reduced to $j = 14.4$ in order to keep the total current $j\sigma_x\sigma_y$ constant. The electron beam's angular spread $\sigma_{\theta x,y} = 0.25$ has been increased to satisfy the matching condition $\sigma_{\theta x,y} = \omega_\beta^2\sigma_{x,y}^2$. With the longer Rayleigh length, the optimum initial electron phase velocity is now $\nu_0 = 6$. The dimensionless mirror radius that corresponds to 1% edge losses is now $r_m = 3.4$, and the dimensionless radius of curvature is $r_c = 1.7$.

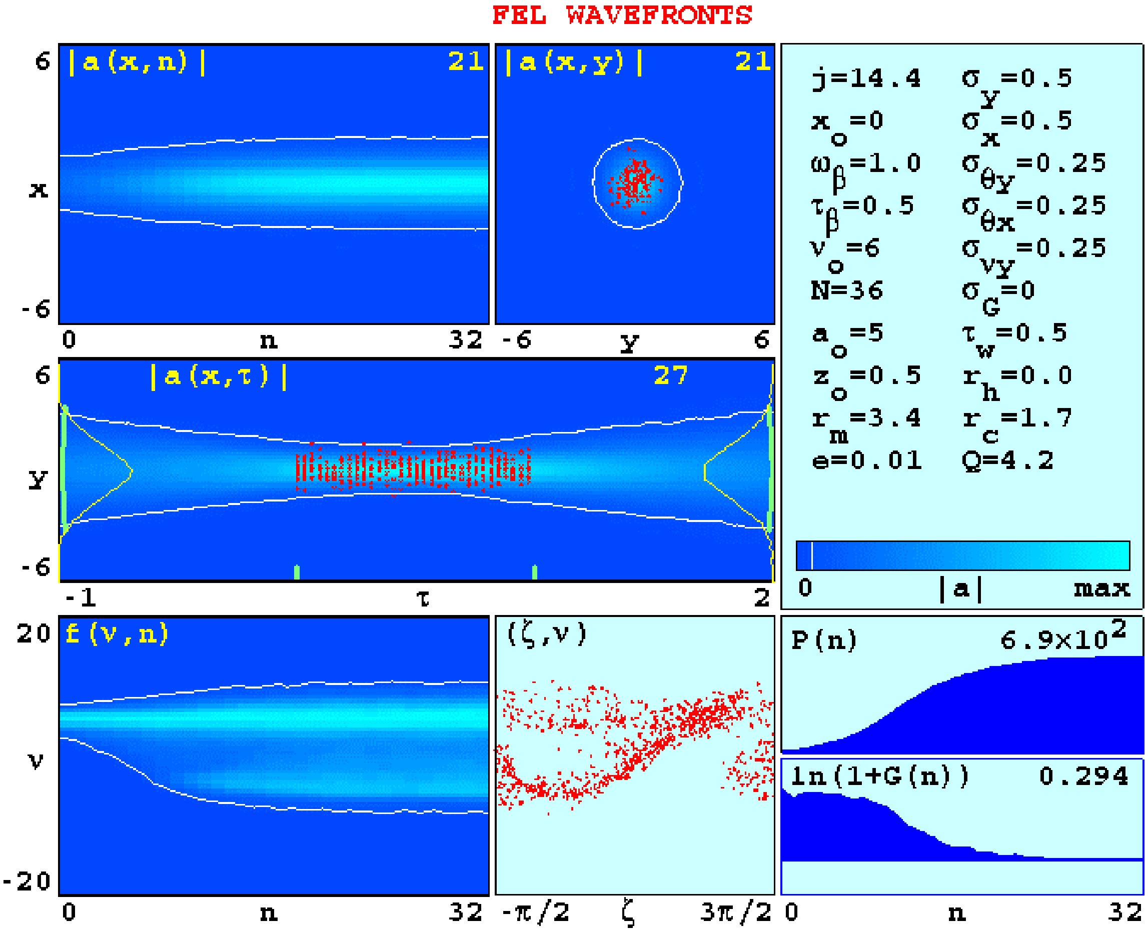

Figure 34. Three-dimensional simulation results for the proposed 100 kW TJNAF FEL with a long Rayleigh length, $z_0 = 0.5$, and a broad electron beam, $\sigma_{x,y} = 0.5$, showing the development of a stable Gaussian mode.

In Figure 34, the optical field evolution plots $\left|a(x,n)\right|$ and $\left|a(x,\tau)\right|$ show that a stable Gaussian mode develops over $n = 32$ passes. Notice that the mirror spot size is much smaller than in Figure 33, and the power is concentrated near the center of the mirror, so mirror damage is more likely in this case. The betatron motion of the electrons is now clearly seen in the red dots on the center-left plot. Some of the sample electrons make excursions far outside the center of the optical mode, where they won't be effectively bunched. As a result, there is less gain, and the extraction efficiency is reduced to $\eta \approx 0.8\%$.

Figure 35 shows a plot of the single-pass extraction efficiency η versus the electron beam radius $\sigma_{x,y}$, for the TJNAF 100 kW FEL parameters with a short Rayleigh length $z_0 = 0.1$. It indicates that a narrow electron beam is beneficial for efficiency, since the electrons are contained well inside the optical mode.

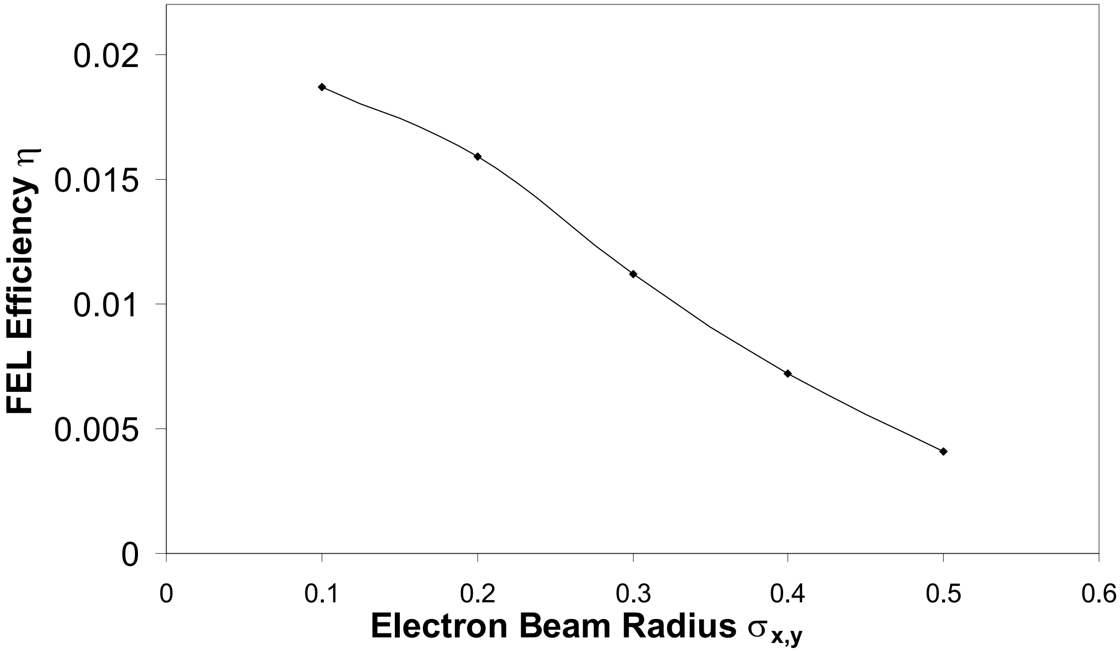

Figure 35. Three-dimensional simulation results for the proposed TJNAF 100 kW FEL with a short Rayleigh length, $z_0 = 0.1$. The efficiency η is plotted versus the electron beam radius $\sigma_{x,y}$. The extraction efficiency increases as the electron beam radius is reduced.

THIS PAGE INTENTIONALLY LEFT BLANK

VI. FOUR-DIMENSIONAL SIMULATIONS

The simulations described in the last two chapters follow the evolution of FEL optical modes in either the longitudinal or transverse directions. They do not require too much computer processing power or memory, and they enable us to isolate and study important physical effects such as pulse slippage, coherence evolution, the trapped-particle instability, diffraction, mode distortion, and wavefront guiding, as discussed in the previous chapters. In many FELs, either longitudinal or transverse mode effects dominate, depending on parameters such as the current density, the electron beam radius, and the pulse length. But in general, both longitudinal and transverse modes are present and interact with each other. Longitudinal pulse slippage effects tend to decrease the gain, while transverse mode distortion effects tends to increase the gain. It is sometimes necessary to study both types of effects simultaneously. For that reason, we have developed four-dimensional simulations that model the electron pulse and the optical wavefront in the x, y, and z directions, as they evolve in time. Unlike the three-dimensional simulations described in the last chapter, we don't have to select the resonance parameter ν in advance; the four-dimensional simulation determines the correct value of ν self-consistently through mode competition.

Four-dimensional simulations may be useful for studying optical modes in a megawatt class FEL with a short Rayleigh length. However, they require large amounts of memory and computer time. We are considering porting them to a supercomputer, or perhaps building a special-purpose computer to solve this problem. We are also studying new techniques for reducing the computational and memory requirements.

A. SHORT PULSES

For modeling short-pulse FELs with narrow electron beams, we have developed a multi-pass, four-dimensional simulation called *4dpnf*. When the electron beam remains well inside the optical mode, $r_e \ll W_0$, the filling factor $F \approx r_e^2 / W_0^2$ is small, and all electrons interact with the same small region of the optical field, so the microscopic bunching is uniform across the electron beam. The distributions of electron phases ζ

and phase velocities ν are therefore uniform across the beam. The values of ζ and ν for each electron are independent of the transverse positions *x* and *y*, but still depend on the longitudinal position *z* and the time τ. Instead of requiring large four-dimensional arrays for the electron microscopic variables ζ and ν, only two-dimensional arrays are needed. This reduces the major memory requirements of the simulation. Sample electrons are initially distributed uniformly in phase from 0 to 2π, but may have a random spread in phase velocities determined by beam emittance and energy spread.

In *4dpnf*, a complex-valued three-dimensional array, $a(x,y,z)$, is used to model the optical beam. The initial optical field shape is parabolic in the longitudinal direction with a length comparable to the electron pulse plus the slippage distance. In the transverse direction, the initial optical field amplitude has a Gaussian shape, while the optical phase is curved in the *x-y* plane so that natural diffraction focuses the beam at position τ_w along the undulator, with dimensionless Rayleigh length $z_0 = w_0^2$ and mode waist w_0.

A three-dimensional array is used in *4dpnf* to represent the electron beam current density $j(x,y,z)$, which is assumed to have a parabolic profile in the *x* and *y* directions. Once the initial electron and optical beams are established, the electrons evolve in phase space according to the pendulum equation

$$\frac{d^2\zeta(z-\tau,\tau)}{d\tau^2} = \left|a(0,0,z,\tau)\right| \cos\left[\zeta(z-\tau,\tau)+\phi(0,0,z,\tau)\right], \tag{52}$$

while the optical field evolves according to the parabolic wave equation

$$\left[-\frac{i}{4}\nabla_\perp^2+\frac{\partial}{\partial\tau}\right]a(x,y,z,\tau) = -j(x,y,z-\tau)\left\langle e^{-i\zeta(z-\tau,\tau)}\right\rangle, \tag{53}$$

where $\nabla_\perp^2 = \partial_x^2+\partial_y^2$ with *x* and *y* again normalized to the characteristic optical mode radius $\sqrt{L\lambda/\pi}$, and $\langle\cdots\rangle$ indicates an average over all electrons at each optical field site. The electron pendulum equation is evaluated using a fourth-order Runge-Kutta method, while the parabolic wave equation is integrated using fast Fourier transforms and diffraction operators [16].

1. CEBAF IR FEL

In the early 1990's, we used *4dpnf* to study a proposed 15 μm IR FEL at the Continuous Electron Beam Accelerator Facility (CEBAF, now known as the Thomas Jefferson National Accelerator Facility or TJNAF) [54]. This author was deeply involved in planning this research, developing and running the simulations, and interpreting their output, and was the lead author of a paper we published on the results of this work [55].

The electron beam for the CEBAF IR experiment had an energy of 45 MeV, with a peak current of 72 A, beam radius of 0.34 mm and pulse length of 0.54 mm. The undulator had $N = 25$ periods of length $\lambda_0 = 6\,\text{cm}$ each, with magnetic field strength $B = 4.4$ kG, corresponding to undulator parameter $K = 1.76$. These parameters give a peak dimensionless current density of $j = 138$, dimensionless beam radius of $\sigma_e = 0.125$ and pulse length of $\sigma_z = 1.4$. A dimensionless Rayleigh length of $z_0 = 0.3$ was chosen to maximize the theoretical weak-field gain, with the mode waist at $\tau_w = 0.5$. The resonator was designed to have 2% mirror transmission, corresponding to quality factor $Q = 50$, and 1% edge losses. The resonator length was 13 times the undulator length, so a mirror wide enough to reflect 99% of the light must have a radius of about 150 times the electron beam radius. That disparity in sizes requires a very large, fine grid in the transverse $x - y$ direction. To allow for a more reasonable grid size, the mirrors were artificially moved closer together, in this case to dimensionless separation $\tau_m = 2$ equal to twice the undulator length. This significantly reduced the laser spot size at the mirror. The mirror's radius of curvature was increased to maintain the same Rayleigh length over the undulator. If the mode shape is the same over the FEL interaction region, reducing the length of the free-space propagation region outside the undulator should not alter the simulation results.

In order to accurately model the transverse profile of the electron beam, it should exist on at least a few $x - y$ grid points. For this simulation, we increased the electron beam radius to $\sigma_e = 0.2$ in order to accommodate a reasonable grid size. The peak current density was decreased to $j = 54$ to keep the same total current, which is proportional to $j\sigma_e^2$. Since the current density j is inversely proportional to the area of the electron beam, the product $j\sigma_e^2$ is actually independent of beam size. In fact, the FEL single-mode gain is proportional to $jF \propto j\sigma_e^2$, and is independent of the electron beam size. If the transverse mode remains undistorted, then the value of σ_e has no effect on the gain. However, when the electron beam is small, transverse mode distortion tends to increase the actual gain above the single-mode gain. The choice of $\sigma_e = 0.2$ is considered small enough to allow some mode distortion if it should occur.

A single mode, one-dimensional simulation in t, including the filling factor F, predicts about 50% single-pass gain for the CEBAF IR FEL. A longitudinal multimode, two-dimensional simulation in (z,t) shows that the short pulse effects alone reduce the gain to about 25%. With a transverse multimode, three-dimensional simulation in (x,y,t), the single-pass gain increases to more than 100% because of mode distortion. A four-dimensional simulation in (x,y,z,t), which includes both mode distortion and short-pulse effects, gives a net single-pass gain of only 18%, roughly the same result given by the two-dimensional simulation. The results of the *4dpnf* simulation over $n = 60$ passes are shown in Figure 36. The output is similar to those from our two-dimensional simulations described in the chapter on longitudinal multimodes. The new intensity/contour plot in the middle-right is the evolution of a cross-section through the optical wavefront $|a(x,n)|$ at $y = z = 0$, shown at the end of each pass through the undulator. The final wavefront cross-section after $n = 60$ passes, shown in the upper-right, is nearly Gaussian. In the middle of the wavefront is a dimple that is about the size of the electron beam, shown in the upper-right as superimposed yellow rectangle. The dimple is caused by the interference of light emitted at $\tau \approx 0.6$ with light emitted later at $\tau \approx 0.9$. At $\tau \approx 0.6$, where electron bunching begins, the new light generated by the narrow electron beam of radius $\sigma_e \approx 0.2$ has a Rayleigh length $z_0 \approx \sigma_e^2 \approx 0.04$, and rapidly diffracts outward. The phase shift of the generated light over the last section of the undulator, $\Delta\tau \approx 0.3$, can be more than $\Delta\phi \approx -\pi$ causing destructive interference. As a result, a higher-order mode structure develops over many passes. The final mode is a combination of the fundamental Gaussian mode and a higher-order mode, causing a dimple on the scale of the electron beam. This dimple disappears when the electron beam size is increased beyond $\sigma_e \approx 0.3$, because the phase shift is insufficient for destructive interference at the end of the undulator.

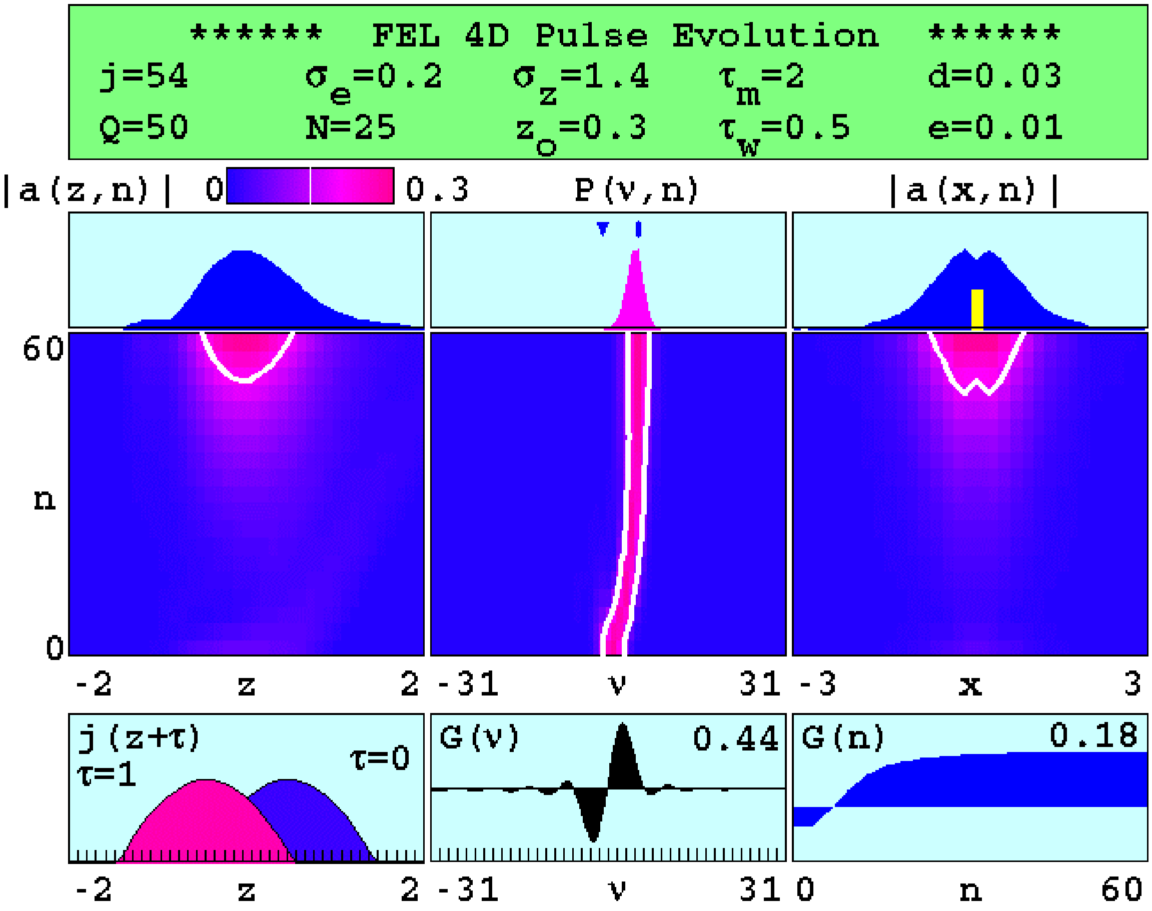

Figure 36. Four-dimensional simulation results for the CEBAF IR FEL, showing steady-state gain $G(n)$ in weak optical fields, and the development of a dimple in the optical wavefront, $|a(x,n)|$. (From [55].)

The theoretical single-mode gain spectrum for these parameters, $G(\nu)$, is shown in the lower middle of Figure 36 for reference. Above the gain spectrum is the optical power spectrum evolution, $P(\nu,n)$, showing the initial power centered at resonance,

$\nu = 0$. After $n \approx 15$ passes, the laser frequency shifts to the value for maximum gain, corresponding to phase velocity $\nu \approx 2.6$. The final power spectrum in the upper-center is narrow, but is Fourier-transform limited by the short optical pulse. In the gain evolution $G(n)$ shown in the lower right, loss initially dominates gain, but as the laser frequency shifts to the value for maximum gain, the single-pass gain grows to about 18%. Considering the mirror loss and the effect of the dimple, this is in rough agreement with the weak-field gain of 25% found in short-pulse simulations without transverse effects.

Figure 37 shows the results of a *4dpnf* simulation of the same FEL, allowed to run for $n = 400$ passes to reach steady-state saturation, where the gain each pass now equals the loss. The desynchronism value $d = 0.005$ has been optimized for maximum power in strong fields, but all other parameters are the same as in Figure 36. The optical power spectrum evolution $P(\nu, n)$ in the center of Figure 37 shows a shift to phase velocity $\nu \approx 2\pi$ for optimum gain in strong fields, as we saw earlier in the FEL gain surfaces. The final optical mode shape $\left|a(x,n)\right|$ has no dimple, because the strong fields reduce the phase shift that is needed for interference.

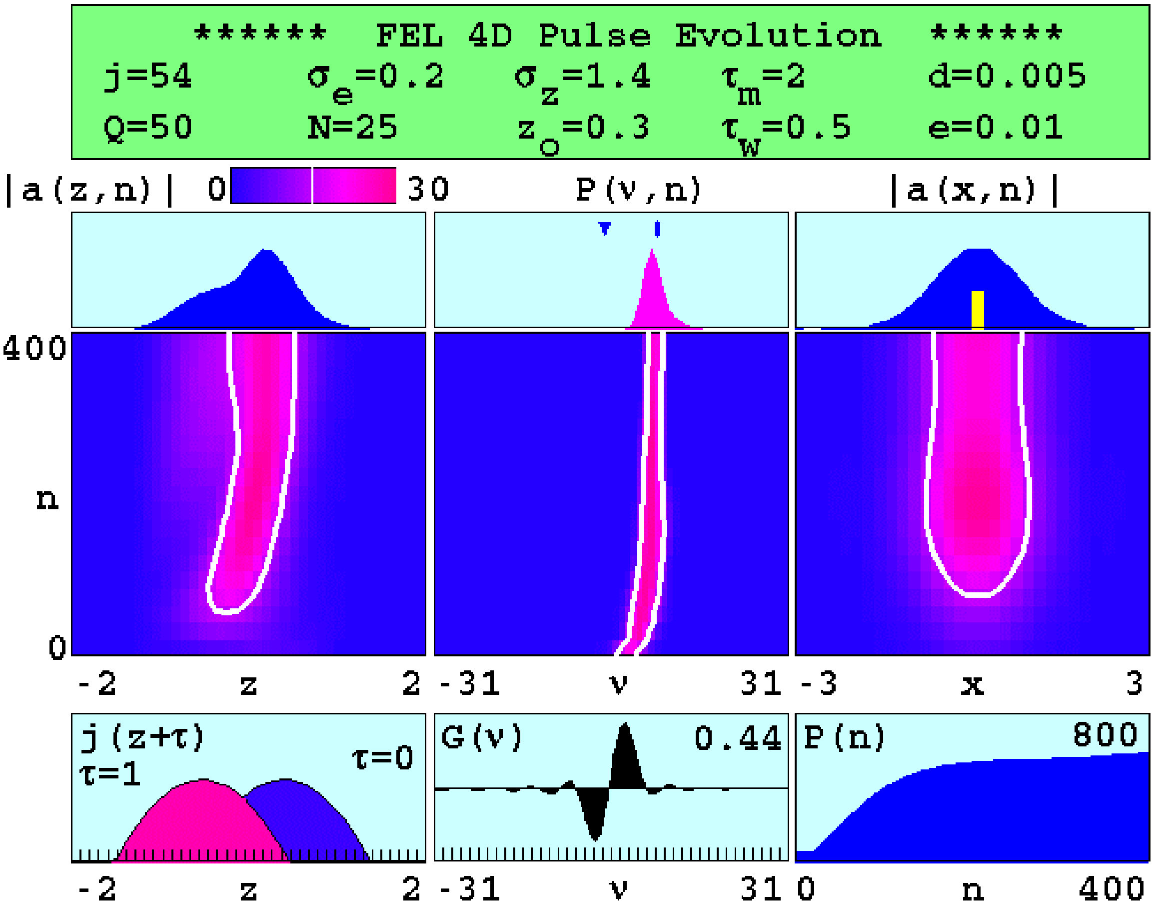

Figure 37. Four-dimensional simulation results for the CEBAF IR FEL, showing steady-state optical power $P(n)$ and the development of a smooth Gaussian wavefront $|a(x,n)|$. (From [55].)

B. LONG PULSES

For modeling long-pulse FELs, we have developed a multi-pass, four-dimensional simulation called *4dwrn*, which includes the betatron motion of the electrons and does not assume a narrow electron beam. A complex-valued three-dimensional array, $a(x,y,z)$, is used to model the optical beam inside a window of width a few slippage distances or less. A three-dimensional array represents the electron beam current density $j(x,y,z)$, which is assumed to have a parabolic profile in the x and y directions. One-dimensional arrays are used to store the microscopic phase and phase velocity of each sample electron, and two-dimensional arrays represent their x and y positions as they execute betatron oscillations. As before, the pendulum equation (52) is used to follow the microscopic motion of the electrons in phase space, and the parabolic wave equation (53) describes the evolution of the light.

1. Boeing 1 kW FEL Oscillator

In 1996, we used *4dwrn* to study the Boeing 1 kW FEL oscillator, discussed earlier in the chapter on longitudinal modes. This author played a key role in planning this research, developing and running the simulations, and interpreting their output, and was the lead author of a paper we published on the results of this work [56]. Figure 38 shows the output from a *4dwrn* simulation of the Boeing FEL oscillator over $n = 50$ passes. The dimensionless current density is $j = 1800$, with an electron beam radius $\sigma_e = 0.5$. The electrons have a Gaussian energy spread given by $\sigma_G = 11$ and an angular spread $\sigma_\theta = 1.4$. The electrons have a betatron frequency $\omega_\beta = 8.4$, or slightly more than one betatron oscillation along the $N = 220$ period undulator. The dimensionless Rayleigh length is $z_0 = 0.5$, with ≈20% mirror outcoupling $(Q = 5)$ and 1% edge losses $(e = 0.01)$.

The power evolution $P(n)$ in the lower right of Figure 38 shows that large optical fields develop rapidly inside the high-gain FEL $(j \gg 1)$, creating deep potential wells in phase space. The bunched electrons undergo synchrotron oscillations, and the trapped-particle instability leads to sideband formation. The sidebands are amplified each pass, modulating the field envelope $|a(z,n)|$ shown on the left, and producing a broad, chaotic optical power spectrum, shown in the center plot, $P(\nu,n)$. The final spectral width is $\Delta\lambda/\lambda \approx \Delta\nu/2\pi N \approx 3.5\%$. The simulation predicts a steady-state output power of $P \approx 8\times10^4$ in our dimensionless units, which corresponds to about 250 W, after accounting for the overall system duty factor.

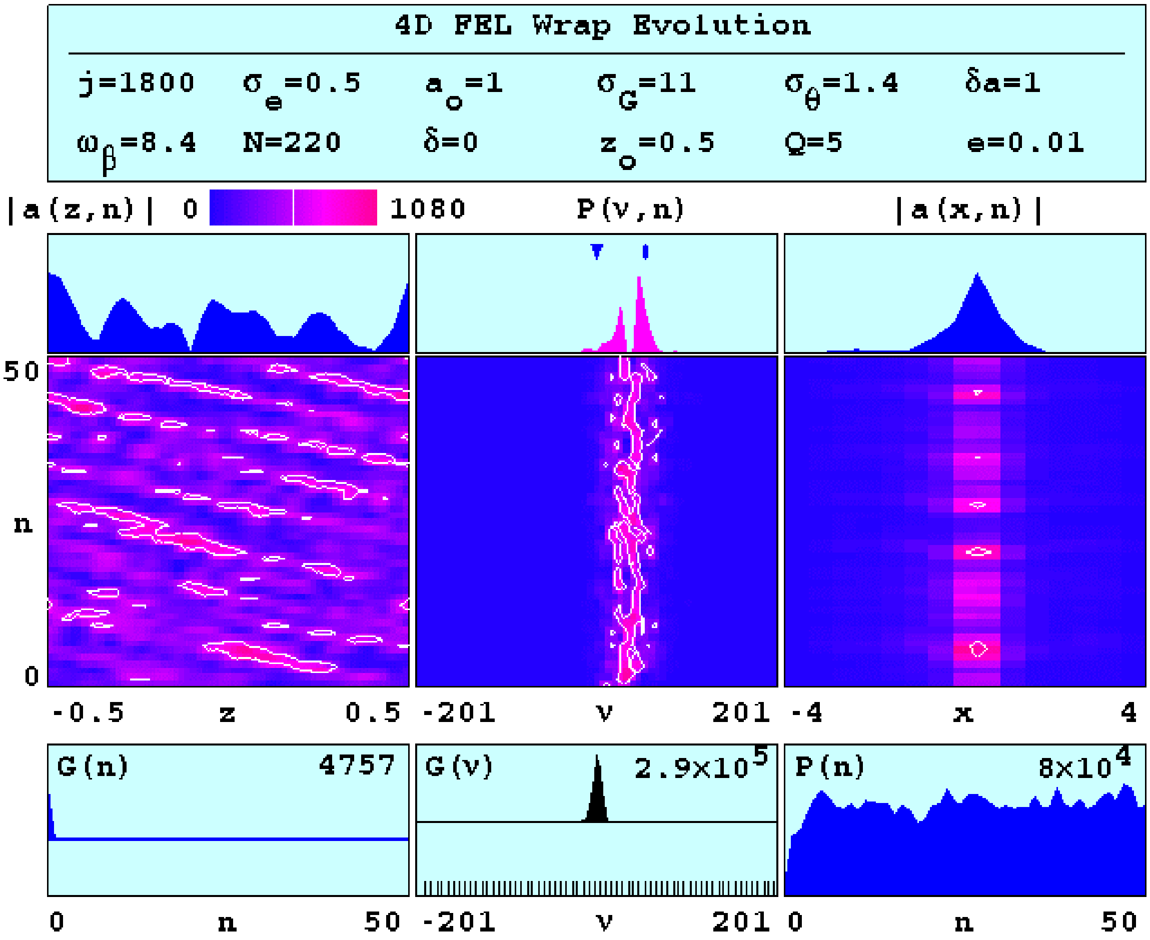

Figure 38. Four-dimensional simulation results for the Boeing 1 kW FEL oscillator, showing the development of a broad, chaotic optical power spectrum $P(\nu, n)$. (From [56].)

One way to prevent the trapped-particle instability is to taper the undulator. This should cause about half of the electrons to become untrapped, which would reduce the synchrotron oscillations. Figure 39 shows another *4dwrn* simulation of the Boeing FEL oscillator, with a 10% undulator taper, corresponding to phase acceleration $\delta = 88\pi$. The theoretical weak-field gain spectrum $G(\nu)$ in the lower center has numerous spikes because of the large undulator taper.

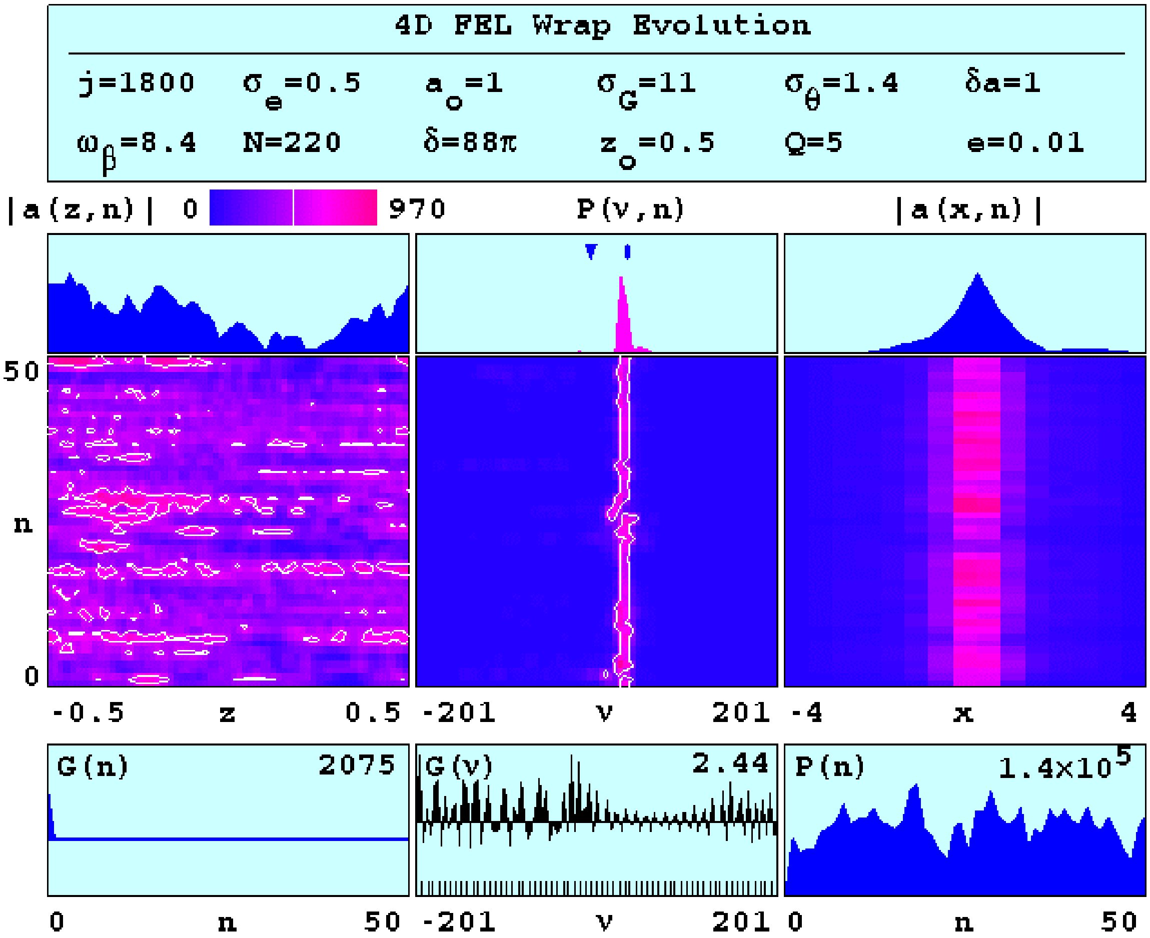

Figure 39. Four-dimensional simulation results for the Boeing 1 kW FEL oscillator with a tapered undulator, $\delta = 88\pi$, showing the suppression of sidebands and the development of a narrow optical power spectrum $P(\nu, n)$. (From [56].)

In Figure 39, we see that the sideband growth is reduced significantly, and the spectral width is now only $\Delta\lambda/\lambda \approx 1\%$. The average output power is increased to 430 W, but the power evolution $P(n)$ shows significant oscillations. This may be due to sporadic attempts at sideband formation and interference of sideband frequencies. Increasing the outcoupling or the system duty factor would be necessary to achieve 1 kW average power.

C. CURRENT NPS RESEARCH: MEGAWATT FEL

At the Naval Postgraduate School, we are working on the design of a compact, high average power FEL for ship defense in collaboration with Jefferson Labs and Advanced Energy Systems [57]. The laser must produce at least 1 MW of average power at a wavelength near 1 μm for propagation through the marine atmosphere and destruction of incoming missiles. With 25% outcoupling, the intra-cavity power would be 4 MW. The entire system is intended to fit inside a box this is approximately $12\text{m}\times 4\text{m}\times 4\text{m}$, so the resonator can only be 12 m long. For a typical Rayleigh length of $Z_0 = 5$ m, the laser spot size on the mirrors would be only a few mm diameter. This spot size would give a power density on the mirrors of about 30 MW/cm^2, which would destroy the mirrors. We have proposed an optical resonator with a very short Rayleigh length of $Z_0 = 1.8$ cm to increase the mirror spot size and reduce the intensity to 210 kW/cm^2. Cooled sapphire mirrors may be able to withstand this intensity without damage.

The design calls for a short $N = 20$ period, $L = 60\,\text{cm}$ length undulator, to enhance the extraction efficiency and avoid beam scraping at the ends of the undulator. For these parameters, the dimensionless Rayleigh length is $z_0 = Z_0/L = 0.03$, compared to a typical FEL with a Rayleigh length of $z_0 = 0.3$. The rms undulator parameter for this design is $K = 2$.

The optical mode radius at its waist in the middle of the proposed resonator is only $w_0 = 0.08$ mm. With such a short Rayleigh length, the beam will expand rapidly, to a spot size of 2.5 cm at the mirrors, approximately 300 times greater than at the waist. This size disparity implies that a grid of at least 4096×4096 elements in the transverse (x, y) plane is required to represent the optical beam throughout the resonator. The grid dimensions are determined by the requirement that it must cover the entire optical wavefront at the mirrors, yet still represent the much smaller wavefront at the waist with $\gtrsim 16$ grid elements. Note that the FFTs used in our propagation algorithm require that the grid dimensions be integral powers of 2.

The superconducting accelerator will provide an electron beam with an energy of 140 MeV and an average current of 0.6 A. The dimensionless current density is $j = 200$, so this is a high-gain FEL. The electron beam will be recirculated to enhance overall system efficiency and reduce shielding requirements for the beam dump. An electron beam radius of $r_e = 0.08$ mm would optimize the overlap with the optical mode in the center of the undulator. This corresponds to a normalized electron beam radius of $\sigma_{x,y} = 0.2$, so there could be significant optical mode distortion.

The electron pulse length is $l_e = 0.3$ mm, or a normalized length of $\sigma_z = 15$ slippage distances, so pulse slippage effects should be minor. However, longitudinal modes should be included to study coherence evolution, and to allow the simulation to self-consistently determine the laser operating frequency. To accurately model the longitudinal pulse for a reasonable number of time steps through the undulator, at least 1024 sites are required in the *z* direction. With the requirement for 4096×4096 elements in the (x, y) plane at each of the longitudinal sites, assuming 8 bytes for each double-precision floating-point number, a 256 GB array is needed to represent the amplitude and phase of the optical field at every point inside the optical cavity. This is much greater than the capacity of currently available personal computers and desktop workstations.

To avoid this memory limitation, we could artificially move the mirrors in closer, as we have done in some of three-dimensional simulations described earlier. Another possibility is to use a re-gridding technique. At the end of the undulator, the mode radius is only $w_L = 1.3$ mm, about 16 times the waist radius. So inside the undulator we could use a grid of only 256×256 elements in the (x, y) plane, requiring only 1 GB. Outside the undulator, when the optical beam expands rapidly and no longer interacts with the narrow electron beam, we could map the optical wavefront onto a coarser grid, the same size (256×256) but with each element representing a larger area. We would use this coarse grid to propagate the wavefront out to the mirror and back, and then map it back onto the fine grid when it re-enters the undulator. One issue we are studying is how to map the wavefront from one grid to another without introducing numerical artifacts. We believe re-gridding won’t affect the fundamental mode, but might cause distortion of higher-order modes.

THIS PAGE INTENTIONALLY LEFT BLANK

VII. CONCLUSION

The results presented in this dissertation cover 10 years of FEL research at the Naval Postgraduate School. This work has added to the understanding of important effects in FELs, such as the trapped-particle instability, pulse lethargy, coherence evolution, limit-cycle behavior, gain degradation due to electron beam quality, optical mode distortion, and optical guiding. It has helped to explain new physical effects such as electron beam energy modulation. It has guided the development of new FEL concepts such as multi-stage optical klystrons, inverse-tapered and step-tapered undulators, and short Rayleigh length resonators. It has played an important role in the design of many existing and proposed FEL experiments, including the Boeing 1 kW oscillator and APLE amplifier, the Stanford FIREFLY and SCA FELs, the SELENE FEL klystron, the SLAC X-ray FEL, the CEBAF IR FEL, and the TJNAF FELs.

Our most recent work has concentrated on the development of high average-power FELs for naval applications. We have worked closely with colleagues at TJNAF as they upgrade their present FEL from 2 kW to 10 kW, and eventually to 100 kW average power. We have visited their laboratory numerous times, attended workshops and upgrade review panels, and produced several joint publications and conference presentations. An important research goal has been to enhance their FEL extraction efficiency while minimizing the induced energy spread of the electrons, to enable beam recirculation. To reach this goal, they are considering new undulator designs such as inverse-tapered and step-tapered undulators. The research results presented in Chapter IV of this dissertation have been useful in evaluating these new undulator designs. Our simulations showed that a small negative linear or step-taper produces the best efficiency, but only a slight improvement over no taper, in contrast to previously published results.

A high average-power FEL may require a short Rayleigh length resonator to avoid mirror damage. Classical FEL theory says that the Rayleigh length should be about one third of the undulator length to optimize the overlap between the electron beam and the optical mode. However, the research results presented in Chapter V of this dissertation show that it may be possible to operate an FEL at a much shorter Rayleigh length, one tenth of the undulator length or less, without a significant reduction in gain. In fact, our simulation results shown in Figure 31 predict that the steady-state power actually increases as the Rayleigh length is reduced. We believe this effect is due to optical mode distortion, as seen for example in Figure 33.

At the Naval Postgraduate School, we are currently designing a compact, megawatt average-power FEL for ship defense, in collaboration with TJNAF and Advanced Energy Systems. To satisfy the size requirements without damaging the mirrors, the optical cavity may need to have a very short Rayleigh length. In that case, our present 3D and 4D simulations will need to use very large transverse grids, overwhelming the memory capacity of desktop computers. To avoid this memory limitation, we are developing a re-gridding technique, discussed in Chapter VI.

The original research by the author presented in this dissertation has played an important role in the development of FELs over the past 10 years. Using numerical simulations, this work has helped to bridge the gap between FEL theory and experiments, to understand important physical effects in FELs, and to aid in the design of new FELs.

LIST OF REFERENCES

1. W.B. Colson, *Laser Handbook*, Vol. 6, Chap. 5, Eds. W.B. Colson, C. Pellegrini and A. Renieri, North Holland, Amsterdam (1990).
2. J.M.J. Madey, *J. Appl. Phys.* **42**, 1906 (1971).
3. B.E. Newman et al., *IEEE J. Quant. Elect.* **QE-21**, 867 (1985).
4. T.J. Orzechowski, B.R. Anderson, W.M. Fawley, D. Prosnitz, E.T. Scharlemann, S. M Yarema, A.M. Sessler, D.B. Hopkins, A.C. Paul and J.S. Wuertle, *Phys. Rev. Lett.* **57**, 2172 (1986).
5. L.R. Elias, W.M. Fairbank, J.M.J. Madey, H.A. Schwettman and T.I. Smith, *Phys. Rev. Lett.* **36**, 717 (1976).
6. W.B. Colson, *Short Wavelength Free Electron Lasers in 2000*, http://www.physics.nps.nav.mil/table1.pdf (2001).
7. S. Benson, et al., *Nucl. Inst. and Meth.* **A429**, 27 (1999).
8. G.R. Neil, et al., *Nucl. Inst. and Meth.* **A445**, 192 (2000).
9. H.-D. Nuhn, *Nucl. Inst. and Meth.* **A445**, 149 (2000).
10. E.T. Scharlemann, *J. Appl. Phys.* **58**, 2154 (1985).
11. W.B. Colson, *Phys. Lett.* **64A**, 190 (1977).
12. J. Blau and W.B. Colson, *Nucl. Inst. and Meth.* **A304**, 436 (1991).
13. J.D. Jackson, *Classical Electrodynamics*, Second Edition, John Wiley and Sons, New York, NY (1975).
14. P. Elleaume, *Laser Handbook*, Vol. 6, Chap. 4, Eds. W.B. Colson, C. Pellegrini and A. Renieri, North Holland, Amsterdam (1990).
15. W.B. Colson and P. Elleaume, *Appl. Phys.* **B29**, 101 (1982).
16. W.B. Colson and J.L. Richardson, *Phys. Rev. Lett.* **50**, 1050 (1983).
17. E.T. Scharlemann, A.M. Sessler, and J.S. Wurtele, *Phys. Rev. Lett.* **54**, 1925 (1985).
18. W.B. Colson, J.C. Gallardo, and P.M. Bosco, *Phys. Rev.* **A34**, 4837 (1986).
19. W.B. Colson and R.D. McGinnis, *Nucl. Inst. and Meth.* **A445**, 49 (2000).
20. W.B. Colson, *Phys. Quant. Elec.* **8**, 457 (1982).
21. W.B. Colson, *Free Electron Laser Generators of Coherent Radiation*, Eds. C.A. Brau, S.F. Jacobs and M.O. Scully, SPIE **453**, 290 (1983).
22. J.N. Eckstein, J.M.J. Madey, K. Robinson, T.I. Smith, S. Benson, D. Deacon, R. Taber and A. Gaupp, *Phys. Quant. Elec.* **8**, 49 (1982).

23. W.B. Colson and J. Blau, *Nucl. Inst. and Meth.* **A259**, 198 (1987).

24. W.B. Colson and I. Boscolo, *Phys. Rev. A* **31**, 2353 (1985).

25. D.D. Quick, J. Blau, R.K. Wong and W.B. Colson, *Nucl. Inst. and Meth.* **A 341**, ABS 92 (1994).

26. E. Kelsey, J. Blau, D.D. Quick, R.K. Wong and W.B. Colson, *Nucl. Inst. and Meth.* **A 358**, ABS 61 (1995).

27. A. Christodoulou, D. Lampiris, W.B. Colson, P.P. Crooker, J. Blau, R.D. McGinnis, S.V. Benson, J.F. Gubeli and G.R. Neil, *Nucl. Inst. and Meth.* **A475**, 182 (2001).

28. C. Pellegrini et al., *Nucl. Inst. and Meth.* **A331**, 223 (1993).

29. K.-J. Kim and M. Xie, *Nucl. Inst. and Meth.* **A331**, 359 (1993).

30. J.B. Hall, J. Blau, R.K. Wong and W.B. Colson, *Nucl. Inst. and Meth.* **A341**, ABS 76 (1994).

31. L. Ramos, J. Blau and W.B. Colson, *Nucl. Inst. and Meth.* **A375**, ABS 54 (1996).

32. D.C. Quimby, C.G. Parazzoli and D.J. Pistoresi, *Nucl. Inst. and Meth.* **A318**, 628 (1992).

33. J. Blau, D.J. Frost and W.B. Colson, *Nucl. Inst. and Meth.* **A 331**, 645 (1993).

34. D.C. Quimby, C.G. Parazzoli, J.B. Romero, B.P. McVey and P.A. Byrd, *Nucl. Inst. and Meth.* **A318**, 680 (1992).

35. D.A. Jaroszynski et al., *Nucl. Inst. and Meth.* **A 331**, 52 (1993).

36. T.I. Smith et al., *Nucl. Inst. and Meth.* **A 358** (1995).

37. D.W. Small, R.K. Wong, J. Blau and W.B. Colson, *Nucl. Inst. and Meth.* **A 358**, ABS 44 (1995).

38. P.W. van Amersfoort et al., *Nucl. Inst. and Meth.* **A 318**, 42 (1992).

39. J. Blau, R.K. Wong and W.B. Colson, *Nucl. Inst. and Meth.* **A 358**, 441 (1995).

40. R.L. Swent, K.W. Berryman, H.A. Schwettman and T.I. Smith, *Nucl. Inst. and Meth.* **A304**, 272 (1991).

41. W.R. Pinkley, W. Wilkenson, J. Blau, R.K. Wong and W.B. Colson, *Nucl. Inst. and Meth.* **A341**, ABS 70 (1994).

42. S. Benson, J. Gubeli and G.R. Neil, *Nucl. Inst. and Meth.* **AXXX**, xxx (2002).

43. G.R. Neil et al., *Nucl. Inst. and Meth.* **AXXX**, xxx (2002).

44. J. Blau, V. Bouras, W.B. Colson, K. Polykandriotis, A. Kalfoutzos, S.V. Benson and G.R. Neil, *Nucl. Inst. and Meth.* **AXXX**, xxx (2002).

45. D.A. Jaroszynski, R. Prazeres, F. Glotin and J.M. Ortega, *Nucl. Inst. and Meth.* **A 358**, 224 (1995).

46. D.A. Jaroszynski, R. Prazeres, F. Glotin, J.M. Ortega, D. Oepts, A.F.G. van der Meer, G. Knippels and P.W. van Amersfoort, *Nucl. Inst. and Meth.* **A 358**, 228 (1995).
47. D.A. Jaroszynski, R. Prazeres, F. Glotin, O. Marcouille, J.M. Ortega, D. Oepts, A.F.G. van der Meer, G. Knippels and P.W. van Amersfoort, *Nucl. Inst. and Meth.* **A 375**, 647 (1996).
48. R.D. McGinnis, J. Blau, W.B. Colson, D. Massey, P.P. Crooker, A. Christodoulou and D. Lampiris, *Nucl. Inst. and Meth.* **A475**, 178 (2001).
49. H.E. Bennett et al., *Nucl. Inst. and Meth.* **A341**, 124 (1994).
50. N.G. Gavrilov et al., *Nucl. Inst. and Meth.* **A304**, 228 (1991).
51. J. Blau, R.K Wong, D.D. Quick, W.B. Colson, *Nucl. Inst. and Meth.* **A341**, ABS 94 (1994).
52. N.G. Gavrilov et al., *Nucl. Inst. and Meth.* **A304**, 63 (1991).
53. J. Blau, T. Campbell, W.B. Colson, I. Ng, W. Ossenfort, S.V. Benson, G.R. Neil and M.D. Shinn, *Nucl. Inst. and Meth.* **AXXX**, xxx (2002).G.R. Neil et al., *Nucl. Inst. and Meth.* **A318**, 212 (1992).
54. G.R. Neil et al., *Nucl. Inst. and Meth.* **A318**, 212 (1992).
55. J. Blau and W.B. Colson, *Nucl. Inst. and Meth.* **A318**, 717 (1992).
56. J. Blau, R.K. Wong and W.B. Colson, *Nucl. Inst. and Meth.* **A375**, 358 (1996).
57. W.B. Colson, A. Todd and G.R. Neil, *Nucl. Inst. and Meth.* **AXXX**, xxx (2002).

THIS PAGE INTENTIONALLY LEFT BLANK

INITIAL DISTRIBUTION LIST

1. Defense Technical Information Center
   Ft. Belvoir, Virginia

2. Dudley Knox Library
   Naval Postgraduate School
   Monterey, California

3. Prof. William B. Colson
   Naval Postgraduate School
   Monterey, California

4. Mr. Joseph Blau
   Naval Postgraduate School
   Monterey, California

5. Prof. Robert L. Armstead
   Naval Postgraduate School
   Monterey, California

6. Prof. James H. Luscombe
   Naval Postgraduate School
   Monterey, California

7. Prof. Andres Larazza
   Naval Postgraduate School
   Monterey, California

8. Prof. Ron Pieper
   Naval Postgraduate School
   Monterey, California

9. Prof. Peter Crooker
   Naval Postgraduate School
   Monterey, California

10. Chairman, Department of Physics
    Naval Postgraduate School
    Monterey, California

11. CDR Roger McGinnis, USN
    Naval Sea Systems Command
    Washington D.C.

12. Dr. Thomas W. Meyer
DARPA/ATO
Arlington, Virginia

13. Dr. George Neil
TJNAF
Newport News, Virginia

14. Dr. Steven Benson
TJNAF
Newport News, Virginia

15. Dr. Fred Dylla
TJNAF
Newport News, Virginia

16. Dr. Alan Todd
Advanced Energy Systems
Princeton, New Jersey

17. Prof. Todd I. Smith
Stanford University
Stanford, California